

CRANFIELD UNIVERSITY

NAN YU

THERMAL ANALYSIS OF ENERGY BEAM USING DE-LAVAL
NOZZLE IN PLASMA FIGURING PROCESS

School of Aerospace, Transport and Manufacturing
Precision Engineering

PhD Thesis
Academic Year: 2013 - 2016

Supervisor: Dr Renaud Jourdain and Dr Mustapha Gourma
Industrial supervisor: Professor Paul Shore
October 2016

CRANFIELD UNIVERSITY

School of Aerospace, Transport and Manufacturing
Precision Engineering

PhD Thesis

Academic Year 2013 - 2016

NAN YU

THERMAL ANALYSIS OF ENERGY BEAM USING DE-LAVAL
NOZZLE IN PLASMA FIGURING PROCESS

Supervisor: Dr Renaud Jourdain and Dr Mustapha Gourma
Industrial supervisor: Professor Paul Shore
October 2016

This thesis is submitted in partial fulfilment of the requirements for
the degree of Doctor of Philosophy

© Cranfield University 2016. All rights reserved. No part of this
publication may be reproduced without the written permission of the
copyright owner.

ABSTRACT

In 2012, plasma figuring was proven to be an alternative solution for the fabrication of large scale ultra-precise optical surfaces. Indeed, plasma figuring was successfully demonstrated on a metre class glass surface. The process was exceptionally rapid but residual errors were observed. This thesis addresses this issue by proposing an enhanced tool that provides a highly collimated plasma jet.

The enhanced tool is characterized by a targeted material removal footprint in the range 1 to 5 mm FWHM. The energy beam is provided by an Inductively Coupled Plasma (ICP) torch equipped with a De-Laval nozzle. This thesis focuses on characterization and optimisation of the bespoke plasma torch and its plasma jet. Two research investigations were carried out using both numerical and experimental approaches.

A novel CFD model was created to analyse and understand the behaviour of high temperature gas in the De-Laval nozzle. The numerical approach, that was based on appropriate profiles of temperature and velocity applied to the nozzle inlet, led to a significant reduction of computational resources. This model enabled to investigate the aerodynamic phenomena observed from the nozzle inlet up to the processed surface. Design rules and the effect of changing nozzle parameters were identified. Sensitivity analysis highlighted that the throat diameter is the most critical parameter.

A challenging power dissipation analysis of the plasma torch was carried out. Temperature and flow rate in key components of the torch were measured. Experimental results enabled to calculate the power dissipation values for RF power up to 800 W and for the entire series of designed nozzles. This work enabled to scientifically understand the power dissipation mechanism in the bespoke ICP torches. In addition, by comparing the intensity of the power dissipation values, one nozzle was clearly identified as being more capable to provide a highly efficient plasma jet.

Keywords:

Plasma figuring, plasma jet, ICP torch, De-Laval nozzle, power dissipation

ACKNOWLEDGEMENTS

Firstly, I would like to thank my supervisors: Dr Renaud Jourdain, Dr Mustapha Gourma and Prof Paul Shore, for their excellent supervision and great encouragement. Dr Jourdain provided me a comprehensive guidance on the lab work, brilliant advice whenever I need help, as well as support for my life in England. Dr Gourma co-supervised me on the subject of the CFD simulations and the calculations of heat transfer. He also gave me a number of invaluable advices for my presentations and defence. Prof Shore supervised me principally in the first two years and advised me from the industrial side in the last year. It has been a great honour to be his student. I appreciate all their contributions with strictest standard and greatest effort.

I would like to thank the review panel members, Dr Paul Comley, Dr Humberto Perotto-Baldivieso, Prof Peter Ball, and Prof Ashutosh Tiwari, for reviewing my report and providing precious suggestions and comments. Special thanks go to two experts in plasma facilities, Prof J Nicholls, Mr J Puchacz, Prof T Arnold, Prof K Yamamura, and Prof S Dong, for their wisdom, knowledge and constructive suggestions.

The project was funded by EPSRC Centre for Innovative Manufacturing in Ultra Precision (CIM-UP). Thanks to the grant EP/I033491/1 to make my research possible. I gratefully acknowledge McKeown Foundation, EUSPEN, and Heidenhain Scholarship for their supports on my academic activities.

Many thanks to the colleagues in plasma group, CIM-UP, and Cranfield. They made my research life much joyful and enjoyable. Among them, special thanks to Adam, Neo, Vincent, and Zihang, who give immediate supports to my project. Great courtesy to Jonathan and Carol for their personal supports.

My previous supervisor, Prof YC Liang, and his team gave me strong support and significant care in the past 5 years. Appreciation also goes to my good friends, Dongsheng, Xueli and Fangda, etc. The benefits will last a lifetime.

Lastly, I would like to thank my family for their supporting continuously and love without any condition. I love you all.

TABLE OF CONTENTS

ABSTRACT	i
ACKNOWLEDGEMENTS.....	iii
TABLE OF CONTENTS	v
LIST OF FIGURES.....	vii
LIST OF TABLES	xii
LIST OF EQUATIONS.....	xiii
LIST OF ABBREVIATIONS	xiv
LIST OF PUBLICATIONS.....	xvii
1 Introduction.....	1
2 Literature review	5
2.1 Large optical fabrication.....	5
2.1.1 Demands.....	5
2.1.2 Materials.....	5
2.1.3 Technical specifications of large optics	7
2.1.4 Optical fabrication processes chain.....	8
2.2 Surface figuring process based on plasma jets	8
2.2.1 Chemical aspects	9
2.2.2 Toolpath algorithms.....	9
2.2.3 Reactive Atom Plasma (RAP)	11
2.2.4 Plasma figuring process	12
2.2.5 Plasma Chemical Vaporization Machining (PCVM)	13
2.2.6 Plasma Jet Machining (PJM).....	17
2.2.7 Other plasma figuring techniques.....	19
2.2.8 Residual mid-spatial frequency errors	20
2.3 Atmospheric pressure plasma	21
2.3.1 Radio frequency plasma torches.....	22
2.3.2 Plasma modes in ICP torches	24
2.3.3 Mechanical design of the ICP torches	25
2.3.4 Plasma jet diagnostics of the ICP torches	27
2.4 Numerical analysis of ICP torches	28
2.5 Power dissipation of the ICP torch	31
2.5.1 Infrared (IR) techniques for temperature measurement	32
2.6 Summary	33
2.6.1 Summary of previous work.....	33
2.6.2 Identification of “Gap of knowledge”	33
3 Methodology.....	35
4 Experimental setup and numerical approach	37
4.1 Experimental setup for the RF network investigation	37
4.1.1 Plasma delivery system (PDS).....	37
4.2 CFD model creation and validation	43

4.2.1 CFD Modelling approach for High Temperature Jet.....	43
4.2.2 Set-up for material removal footprint experiment	50
4.3 Experimental setup for the power dissipation analysis.....	52
4.3.1 Measurement method and instrumentation for the power dissipation analysis	52
4.3.2 Experimental method for the power dissipation analysis.....	57
5 Results	62
5.1 Result of RF network investigation.....	62
5.1.1 Effects of capacitors in the RF network.....	62
5.1.2 Effects of torch coil in the RF network	66
5.1.3 Summary	70
5.2 Result - numerical analysis of De-Laval nozzle designs	72
5.2.1 Aerodynamic behaviour of the De-Laval nozzle	72
5.2.2 De-Laval nozzle evaluation using CFD model.....	78
5.2.3 CFD optimized nozzle versus original nozzle	82
5.2.4 Summary	84
5.3 Result - power dissipation analysis of ICP torch	85
5.3.1 Results of measurement of coolant (flow rate and temperature)	85
5.3.2 Power absorbed by coolants in E mode	90
5.3.3 Uncertainty analysis	91
5.3.4 Power absorbed by coolants in H mode.....	93
5.3.5 Power dissipated by argon gas in H mode	95
5.3.6 Power dissipated by radiation in H mode	96
5.3.7 Summary	98
5.4 Result of power dissipation analysis of enhanced nozzle series.....	101
5.4.1 Design and manufacturing of enhanced nozzles.....	101
5.4.2 Power dissipation comparisons	106
5.4.3 Summary	107
6 Discussion	109
6.1 Numerical approach and its result.....	109
6.2 Power dissipation analysis.....	110
7 Conclusion.....	112
8 Recommendations for future work.....	115
REFERENCES.....	117

LIST OF FIGURES

Figure 2-1 International science programmes: 1) Ground telescopes (EELT) [4]; 2) EUV lithography (ASML) [5]; 3) National Ignition Facilities (NIF) [6].....	5
Figure 2-2 Segments of EELT: The size of EELT's primary mirror [4] (left); The prototype segment fabricated by Cranfield University (right)	7
Figure 2-3 Rapid production chain for large scale mirror segment fabrication [13]	8
Figure 2-4 Schematic of random pitch spiral path (left) and PSD for random pitch spiral polished region (right) [23].....	10
Figure 2-5 Schematic of reversed staggered tool-path algorithm in [22]	11
Figure 2-6 The RAP process on fused silica, using CF_4 in an argon plasma [30]	12
Figure 2-7 Topography of a 420x420 mm ² ULE mirror before (left) and after (right) figuring within 2.5 hours [22]	13
Figure 2-8 Schematic of the shaping method principle using pipe electrode (left) and its dedicated footprint under different intrachamber pressures [38]	15
Figure 2-9 Schematic of the shaping of the workpiece with a curved surface [38](left) and its photo (from Nikon website)	15
Figure 2-10 Cross section of footprint for different of tilt angles of electrode (left) and thicknesses of the workpiece [39].....	16
Figure 2-11 SEM image of the tip of microelectrode (left) and surface topography used for small complex-shaped optics (right) [40].....	16
Figure 2-12 a) Schematic drawing of the PJM process [51]; b) Photo of microwave excited primary plasma jet in contact with a dielectric surface [55]; c) Photo of RF excited primary plasma jet in contact with a conducting surface [55].....	17
Figure 2-13 Setup of a microwave driven PJM facility [59]	18
Figure 2-14 Setup of a microwave driven PJM facility [59]	18
Figure 2-15 Figuring of 400 mm diameter areas: Average directional PSD plot of the residual error map Y-cross-sections for the figure correction over 400 mm diameter areas [22].....	21
Figure 2-16 Schematic diagram of the RF CCP torch with central tubular electrode and two outer ring electrodes [72].....	22
Figure 2-17 Approximate plasma domains [19]	24
Figure 2-18 (a) Schematic diagram of the RF ICP torch; (b) Low power plasma discharge in air [84]	25

Figure 2-19: (a) Induction plasma torches manufactured by Tekna; (b) Cross-section of the Tekna torch equipped with a nozzle [88]	26
Figure 2-20 Bespoke ICP torch equipped with an original De-Laval nozzle	26
Figure 2-21 Heavy particles temperature contours in the supersonic and the subsonic jets [117]	29
Figure 2-22 Ionization non-equilibrium degree [117]	30
Figure 2-23 Velocity axial profiles in supersonic and subsonic plasmas [117] ..	30
Figure 2-24 Details of annular slot for air injection and splitter plate in near-throat region showing Mach number distribution for CO ₂ /air flow combination [118]	31
Figure 2-25 Surface topography showing the MSF features [129]	34
Figure 3-1 Logic diagram of the PhD project	35
Figure 4-1 PDS schematic (left) and CAD model of the torch assembly (right)	37
Figure 4-2 Correlation between capacitance and COMET capacitor knob	39
Figure 4-3 Photo of the ICP torch (right) and the cross-section of its schematic (left)	40
Figure 4-4 Round wire coil with dimensions [131]	41
Figure 4-5 ICP torch regions and part names	41
Figure 4-6 Argon flow rate versus forwarded power	42
Figure 4-7 Coolant temperature variation for a two hour period	43
Figure 4-8 Computational domain in [86]	46
Figure 4-9 Correlation between benchmark model [86] and author's validation models. Top: axial pressure profiles; Bottom: axial temperature profiles...	47
Figure 4-10 Computational domain of the model and its geometry (unit mm) ..	49
Figure 4-11 Schematic of the torch path (left), picture of both substrate and torch (right)	50
Figure 4-12 Cross section of the trench	51
Figure 4-13 Depth of trench footprint versus standoff distance	52
Figure 4-14 Photo of the NI DAQ used in the experiment	53
Figure 4-15 Instrumented plasma torch using RTD sensors	54
Figure 4-16 Cross section schematic for the wrapped RTD sensor (top) and OMEGAFLIM RTD sketch (bottom)	54

Figure 4-17 Photo of the IMPAC Pyrometer IN 510 (top) and the optical sensor head (bottom)	55
Figure 4-18 Setup of the measurement using ThermolMAGER TIM 450 (left) and a field of view from ThermolMAGER (right)	56
Figure 4-19 Photo of the flowmeter used in the experiment (left) and multiplying factor graph (right)	57
Figure 4-20 Temperature controlled plasma torch and mix match RF network	58
Figure 4-21 Schematic the plasma delivery system: RF generator, gas supply, chiller, RTDs, flow meter (FM), torch and coolant channels are shown	59
Figure 4-22 Coolant temperature variation for a two-hour period	59
Figure 4-23 Supply total temperature measurement logs of the coolants using both RTD and TC	60
Figure 4-24 Temperature measurement log of the nozzle using TC	61
Figure 4-25 Temperature measurement logs of the coolants using RTD	61
Figure 5-1 Frequency versus tune capacitance	63
Figure 5-2 Frequency versus load capacitance	64
Figure 5-3 Comparison of influence on frequencies between tune capacitor and load capacitor	64
Figure 5-4 Ignition powers recorded at different tune capacitances	65
Figure 5-5 Load capacitance versus ignition power	66
Figure 5-6 Photo showing the length of coil (left) and its measurement method (right)	66
Figure 5-7 Frequency and ignition power versus the length of coil	67
Figure 5-8 Three-turn powered coil, and two-and-a-quarter-turn free coil (left) and three-turn powered coil, and two- turn free coil (right)	68
Figure 5-9 Frequency for 2¼-free-turn coil and 2-free-turn coil	68
Figure 5-10 Forwarded power versus reflective power for 2¼-free-turn coil and 2-free-turn coil	69
Figure 5-11 Calculated distribution of the Mach number (left), the temperature of HTJ (right) (x-axis is radial distance from the symmetric line, and z-axis is axial distance along the symmetric line)	73
Figure 5-12 Axial profiles of temperature, blue dotted line and velocity, black solid line (top), Static pressure along the symmetric axis of the De-Laval nozzle (bottom)	74

Figure 5-13 Radial profiles of (a) temperature, (b) density, (c) axial velocity, and (d) radial velocity along the “POI”	75
Figure 5-14 Radial profile of the axial velocity along POI (left) and sketch of the HTJ that flows onto the “Exposed area” (right)	76
Figure 5-15 Curves of the footprint (black solid line) and axial velocity of HTJ along the POI (blue dotted line)	77
Figure 5-16 Correlation between footprint 6 sigma values and exposed area diameters.....	77
Figure 5-17 The throat diameter (D_2) versus the radius exposed to free radicals (♦ left), and D_2 versus the maximum velocity in the throat (▲ right)	79
Figure 5-18 The divergent end dimensions (D_3) versus the radius exposed to free radicals (♦ left), and D_3 versus the maximum velocity in the throat (▲ right)	80
Figure 5-19 The depth of the divergent path (h_3) versus the radius exposed to free radicals (♦ left), and h_3 versus the maximum velocity in the throat (▲ right). (Divergent angle changes with h_3).....	81
Figure 5-20 The depth of the divergent path (h_3) versus the radius exposed to free radicals (♦ left), and h_3 versus the maximum velocity in the throat (▲ right). (Divergent angle is kept constant)	82
Figure 5-21 Temperature map of gas mixture: original nozzle (left), enhanced nozzle (right)	83
Figure 5-22 Axial profiles of velocity (left) and temperature (right) along the symmetric axis.....	83
Figure 5-23 Radial profiles of axial velocity (left) and temperature (right) along the impinged surface	84
Figure 5-24 Photo of the reading (left) and the measurement position on the pipe through coil (right)	85
Figure 5-25 Photo of the reading (left) and the measurement position on the pipe through nozzle (right)	86
Figure 5-26 Photo of the reading (left) and the measurement position on the total return pipe (right)	86
Figure 5-27 Temperature measurement logs of the coolants using RTD	87
Figure 5-28 Temperature differences of the coolants through ICP torch (1st to 6th trial).....	88
Figure 5-29 Temperature differences of the coolants through ICP torch (7th trial)	88

Figure 5-30 Temperature differences of the coolants through ICP torch (8th trial)	89
Figure 5-31 Left: schematic of the coolant circuit. RTDs were positioned at four key points of the coolant circuit; Right: temperature difference of coolant channels: coil, nozzle and total	89
Figure 5-32 RF power versus temperature difference	90
Figure 5-33 RF power versus power dissipated for each coolant channel in E mode	91
Figure 5-34 Image of the bespoke ICP torch obtained by spectrum camera	93
Figure 5-35 Image of the original ICP torch nozzle obtained by thermal camera	94
Figure 5-36 Temperature measurement logs of the coolants using RTD (Note: * marks the forward power given in H mode)	94
Figure 5-37 RF power versus temperature difference in E and H mode plasma	95
Figure 5-38 RF power versus power dissipated from the total coolant in both E and H mode	95
Figure 5-39 Radiation regions of the ICP torch	97
Figure 5-40 Cross section of existing nozzle	102
Figure 5-41 Left: ICP torch; Right: the dedicated flange (top view)	102
Figure 5-42 Four parts of the new nozzle	103
Figure 5-43 Assembly of the new nozzle. Left: external view; Middle: perspective drawing; Right: cross section with flange	104
Figure 5-44 Assembly diagrams of the new nozzle and existing flange. Left: section view; Right: top view	104
Figure 5-45 3D drawings of existing and new nozzle	105
Figure 5-46 Predicted power dissipated of enhanced nozzles when RF power is 1200 W	106

LIST OF TABLES

Table 2-1 Properties of optical material options (value is given from low to high temperature)	7
Table 2-2 Plasma jet sources (2.45 GHz microwave) for atmospheric plasma processing of surfaces, developed at IOM [50].....	19
Table 4-1 Parameters recorded during the operation of plasma delivery system	60
Table 5-1 Optimum values for the RF network	70
Table 5-2 Parameters of the nozzle in the characteristic analysis.....	78
Table 5-3 Uncertainty budget of the power dissipation of coolant	92
Table 5-4 Power balance of the ICP system	98
Table 5-5 Parameters of related material	104
Table 5-6 Dimensions of the original and enhanced nozzles	105

LIST OF EQUATIONS

(2-1).....	9
(2-2).....	9
(4-1).....	37
(4-2).....	40
(4-3).....	44
(4-4).....	44
(4-5).....	44
(4-6).....	44
(4-7).....	45
(4-8).....	45
(4-9).....	45
(4-10).....	46
(4-11).....	48
(4-12).....	56
(4-13).....	57
(5-1).....	90
(5-2).....	96
(5-3).....	96
(5-4).....	96
(5-5).....	97

LIST OF ABBREVIATIONS

ADC	Analog-to-Digital Converter
APPP	Atmospheric Pressure Plasma Polishing
BC	Boundary Conditions
CCP	Capacitively Coupled Plasma
CF ₄	Carbon Tetrafluoride
CFD	Computational Fluid Dynamics
CNC	Computer Numerical Control
CTE	Coefficient Thermal Expansion
DAQ	Data Acquisition
EEDF	Electron Energy Distribution Function
EELT	European Extremely Large Telescope
EEM	Elastic Emission Machining
EM	Electromagnetic
ESO	European Southern Observatory
EUV	Extreme Ultra Violet
FDM	Finite Difference Method
FEM	Finite Element Method
FJP	Fluid Jet Polishing
FP	Forward Powers
FSD	Full Scale Deflection
FVM	Finite Volume Method
FWHM	Full Width at Half Maximum
HiPER	High Power laser Energy Research facility
HSF	High Spatial Frequency
HTJ	High Temperature Jet
IBF	Ion Beam Figuring
ICP	Inductively Coupled Plasma
IOM	Leibnitz Institute for Surface Modification

IR	Infrared
LLNL	Lawrence Livermore National Laboratory
LMJ	Laser Megajoule
LSF	Low-Spatial Frequency
LTE	Local Thermodynamic Equilibrium
MFC	Mass Flow Controllers
MHD	Magneto-Hydrodynamics
MRF	Magnetorheological Finishing
MRR	Material Removal Rate
MSF	Mid-Spatial Frequencies
NF ₃	Nitrogen Trifluoride
NI	National Instruments
NIF	National Ignition Facility
OES	Optical Emission Spectrometry
OFAT	one-factor-at-a-time
PAP	Plasma Assisted Polishing
PCVM	Plasma Chemical Vaporization Machining
PDS	Plasma Delivery System
PJM	Plasma Jet Machining
PLC	Programmable Logic Controller
POI	Pathway Of Investigation
PSD	Power Spectral Density
RAP	Reactive Atom Plasma
RF	Radio Frequency
RMS	Root Mean Square
RP	Reflective Powers
RTD	Resistance Temperature Detectors
SF ₆	Sulfur Hexafluoride
SiC	Silicon Carbide
SSD	Sub Surface Damage

TC	Thermocouples
TD	Temperature Difference
TMT	Thirty Meters Telescope
ULE	Ultra Low Expansion
VHF	Very High Frequency
VLT	Very Large Telescope
WP	Work Package

LIST OF PUBLICATIONS

Journal papers:

Yu, N., Jourdain, R., Gourma, M., & Shore, P. (2016), “Analysis of De-Laval nozzle designs employed for plasma figuring of surfaces”, International Journal of Advanced Manufacturing Technology. (DOI: 10.1007/s00170-016-8502-y)

Jourdain, R., Castelli, M., **Yu, N.**, Gourma, M., & Shore, P. (2016), “Estimation of the power absorbed by the surface of optical components processed by an inductively coupled plasma torch”, Applied Thermal Engineering (DOI: 10.1016/j.applthermaleng.2016.08.024)

Conference papers (reviewed):

Yu, N., Jourdain, R., Gourma, M., & Shore, P. (2016), “Enhanced nozzle design of highly collimated plasma jets for surface correction”, In: Proceedings of the 16th International Conference of the European Society for Precision Engineering and Nanotechnology, Session 6, 20 May – 3 June 2016, Nottingham (UK), EUSPEN, Cranfield, art. no. p6.31.

Yu, N., Jourdain, R., Gourma, M., & Shore, P. (2016), “Energy Balance Investigation of an Inductively Coupled Plasma Torch for Plasma Figuring”, In: Proceedings of euspen’s Special Interest Group Meeting: Thermal Issues, Session 1b, 17 – 18 March 2016, Prague (CZ), EUSPEN, art. no. o1.4.

Yu, N., Jourdain, R., Gourma, M., & Shore, P. (2015), “Investigation of power dissipation in a collimated energy beam”, In: Proceedings of 6th International Conference of Asian Society for Precision Engineering and Nanotechnology, Session 10, 15 – 20 August 2015, Harbin (China), ASPEN, art. no. 157.

Yu, N., Jourdain, R., Gourma, M., & Shore, P. (2014), “Analysis of nozzle design used for the creation of advanced energy beam”, In: Proceedings of ASPE 29th annual meeting, Session VIII, 9 – 14 November 2014, Boston (USA), American Society for Precision Engineering, Raleigh, pp 200 – 205.

Conference papers (non-reviewed):

Yu, N., Jourdain, R., Gourma, M., & Shore, P. (2014), “Analysis of nozzle design used for reducing the MSF errors in rapid plasma figuring”, In: Proceedings of the 3rd Annual EPSRC Manufacturing the Future Conference, 23 – 24 September 2014, Glasgow (UK).

Yu, N., & Shore, P. (2014), “Precision engineering and Reactive Atom Plasma (RAP) figuring techniques at Cranfield”, In: Proceedings of 9th UK-China Workshop on Space Science and Technology, 28 – 29 May 2014, Shanghai (China).

1 Introduction

Large scale ultra-precise surfaces are required for several major science programmes. Large optics are used in laser energy fusion plants: National Ignition Facility (NIF), Laser Megajoule (LMJ) and High Power laser Energy Research facility (HiPER). In the area of integrated circuits, large mirrors are required for extreme ultra violet (EUV) lithography for patterning structures at 7 nm node (Samsung) and 5 nm node (TSMC). Another field of interest is astronomical projects. Both the European Extremely Large Telescope (EELT) and the Thirty Meters Telescope (TMT) are designed on the bases of a segmented primary mirror that is tens of meters in diameter.

Conventional surface figuring methods will not meet the form accuracy requirements because of the large demand. Also the fabrication of thousands of metre-size (form accuracy better than 20 nm RMS and surface roughness better than ~1 nm RMS) led to an expected processing duration of ten hours which has not been demonstrated yet.

Both ultra-precision grinding and polishing are mature, while the surface figuring process is not. Currently, existing figuring processes includes Ion Beam Figuring (IBF) and Magnetorheological Finishing (MRF). Although these processes can achieve high form accuracy and excellent surface roughness, they cannot meet the ten hour target. Also it must be mentioned that the high vacuum chamber used for the IBF process affects the cost significantly.

An alternative approach is the used of plasma jet at atmospheric pressure. Plasma based figuring techniques have been proven to be a successful alternative method for the finishing step by many research institutes. Among these plasma figuring techniques, the Reactive Atom Plasma (RAP) was developed in the context of metre scale optical surfaces correction. Research on RAP has been progressed at Cranfield University Precision Engineering Institute since 2003. Many optical materials, such as ULE, fused silica, silicon, BK7 and SiC, are proven to be processed using the RAP. The RAP process combines high surface finishing and high removal rates. The world largest

plasma figuring machine (Helios 1200) was created through collaboration between RAPT Industries and Cranfield University in 2008. This machine is based on a motion controller and an inductively coupled plasma (ICP) torch, where argon (main gas) and SF₆ (reactive species) are ignited using alternated current. In 2012, a rapid surface figuring demonstration was carried out on a 420 mm x 420 mm ULE glass surface by Castelli et al. using Helios 1200. Form accuracy of 31 nm RMS was achieved from originally 373 nm RMS within 3 iterations of 45 mins each. This result proved that the RAP process was an ideal alternative for the figure correction of large optical surfaces. However, mid-spatial frequencies (MSF) were observed and analysed by Jourdain and Castelli. MSF could result in hazing effect, and lead to energy loss. Therefore, minimization and elimination of MSF had to be addressed in the next step of the plasma figuring research.

Highly collimated energy beams characterized by a material removal footprint in the range 1 to 5 mm FWHM and removal rate in the range 1~5 mm³ min⁻¹ were targeted. This project focuses on characterization and optimisation of a bespoke plasma torch and its plasma jet. The following objectives have to be addressed:

1. Creation of a method for tuning the plasma delivery system: Investigation of the RF network of the plasma delivery system and determination of the influencing factors. Find out the optimum parameters in the RF network.
2. Numerical analysis of a De-Laval nozzle of the plasma torch: Investigation of the thermodynamic property of the gas mixture using computational fluid dynamics (CFD) simulations.
3. Power dissipation analysis of the plasma torch: Investigation of the power loss mechanism of a plasma delivery system for the bespoke ICP torch.
4. Experimental tests of enhanced nozzles: Design of a series of De-Laval nozzles based on the results obtained through the CFD analysis. Test the nozzles using the power dissipation analysis.

The structure of this thesis is indicated below:

Chapter 2 contains a comprehensive literature survey that was made to introduce the scientific and commercial background of plasma figuring technique, a clear statement of previous works and current challenges. The gap of knowledge was identified after reviewing all the related literatures.

Chapter 3 contains the methodologies of the project. It includes four work packages (WP) of investigation to achieve the aforementioned four objectives. Chapter 3 explains how the investigation in each WP works and the logical relationship of each other.

Chapter 4 contains the description of the model creation, experimental setup and the instrumentation and equipment used throughout this PhD project.

Chapter 5 presents the results of the four work packages.

Section 5.1 contains the work carried out to investigate the RF network response. An optimum tuning of three system parameters is recommended.

Section 5.2 contains the discussion about the results obtained in CFD simulation work. The model is based on the High Temperature Jet (HTJ) specifically for a De-Laval nozzle. It was validated initially with a benchmark model [1] and further validated against with the previous material removal footprints.

Section 5.3 focuses on the power dissipation mechanism of the bespoke ICP torch and its original nozzle. Temperature and flow rate measurements were carried out and these results are used to calculate how much power the torch loses through its two key components: nozzle and coil. This method was used to test the designed nozzles -Section 5.4.

Section 5.4 contains the new nozzles that are designed based on the CFD simulation results and engineering experience. These nozzles are tested using the power dissipation measurement. Finally, an optimisation nozzle was chosen from all those new nozzles with higher torch efficiency.

Chapter 6 contains the discussion about the whole work of this thesis. Problems and advancements are highlighted.

Chapter 7 contains the author's conclusions and highlights the contributions to the knowledge.

Chapter 8 contains the future work suggestions.

2 Literature review

2.1 Large optical fabrication

2.1.1 Demands

Ultra-precise and ultra-smooth surfaces are gaining in importance. Large scale ultra-precise optical surfaces are becoming the main consumable for several international science programmes and research projects. These include laser fusion energy, extreme ultra violet (EUV) lithography and ground and space based telescopes (Figure 2-1). A variety of astronomical projects such as the European Extremely Large Telescope (E-ELT) and the Thirty Meters Telescope (TMT) led to design and fabrication of segmented primary mirrors of tens of meters in diameter [2,3]. Thus, this research focuses on an advanced optical figuring fabrication process for large and ultra-precise surfaces. First we will focus on the high end materials used.



Figure 2-1 International science programmes: 1) Ground telescopes (EELT) [4]; 2) EUV lithography (ASML) [5]; 3) National Ignition Facilities (NIF) [6]

2.1.2 Materials

In the aforementioned world leading projects, glass and glass ceramics are very often selected for the optical components. Taking the telescopes application for examples, they require extremely small thermal coefficient expansion and high stiffness. Corning ULE[®] is well known since it became the material choice for the primary mirror of Hubble space telescope. Another material named Zerodur[®] (Schott company) was supplied for Chandra X-ray Observatory and ESO/ Very Large Telescope (VLT), and Keck telescope. Materials like Fused silica and silicon carbide (SiC) are also used frequently.

ULE[®] is a titania-silicate glass characterised by an extremely low coefficient thermal expansion (CTE). CTE is lower than $3.3 \times 10^{-8} \text{ K}^{-1}$ for temperature range of 5 to 35 °C [7]. It is made using a flame soot deposition process that currently yields monolithic boules. This material is used for the fabrication of lightweight optics. Indeed, 80% weight reduction was achieved by the lightweight fusion bonded structures, while 95% from ultra-lightweight frit bonded structures. The 1.5 m class ULE mirrors with areal densities less than 10 kg m^{-2} , was made for an application requires light-weighting and corresponding high stiffness-to-weight ratio.

Zerodur[®] is a glass ceramic material (inorganic, non-porous lithium aluminium silicon oxide) that is widely used for ground-based telescopes [8], [9]. Although it has similar material properties with ULE, Zerodur is very different because it is a glass ceramic [10]. Zerodur is more cost effective for large mirror blanks (~8 m corner to corner) [9]. The areal density of 45 kg m^{-2} is common.

Silicon carbide (SiC) is a ceramic. It is a popular candidate for optical mirrors because of the excellent thermo-mechanical properties, with better thermal stability and stiffness than ULE or Zerodur. Its mechanical properties make it very difficult to machine. Diamond is used to grind or polish SiC. Its machining is accompanied with serious tool wear. Also, on the surface of a lightweighted SiC substrate, a scanning print-through is the main issue.

Fused silica is a non-crystalline glass of silicon dioxide with excellent optical qualities. This is a very low thermal expansion material with CTE of $5.5 \times 10^{-7} \text{ K}^{-1}$ in the range of 25 -100 °C (data from Schott Lithosil [11]), and also extremely thermal shock resistant, enabling its use in precision mirror substrates [12]. With much better ultraviolet transmission than other glasses, fused silica is a great choice for ultraviolet spectrum lenses.

The basis of approach for choosing an optical material is to assess homogeneity, absence of bubbles, chemical resistance, CTE, specific stiffness, workability. Generally, the ideal material has a large specific stiffness and a small CTE. From the Table 2-1, no material could meet the aforesaid

requirements. Thus, comprehensive estimation is carried out to make a decision for each specific mirrors design.

Table 2-1 Properties of optical material options (value is given from low to high temperature)

Material	Density (g cm ⁻³)	Elasticity modulus (GPa)	Poisson ratio	CTE (10 ⁻⁶ K ⁻¹)	Thermal conductivity (W mK ⁻¹)	Thermal diffusivity (10 ⁻⁶ m ² s ⁻¹)
ULE	2.21	67.6	0.17	0.033	1.31	0.77
Zerodur	2.53	91	0.24	0.02-0.1	1.64	0.72
SiC	2.89-3.21	391-466	0.25	2.4	150-57	65-13
SiO ₂	2.2	72.1	0.17	0.55	1.31	0.75

2.1.3 Technical specifications of large optics

In order to realize these new instruments mentioned in section 2.1.1, the figuring process should meet the following requirements:

- 1) High form accuracy (better than $\lambda/60$ RMS);
- 2) Low surface roughness (less than 1nm RMS);
- 3) Rapid surface figure correction at nanometre accuracy (better than 10 h m⁻²).

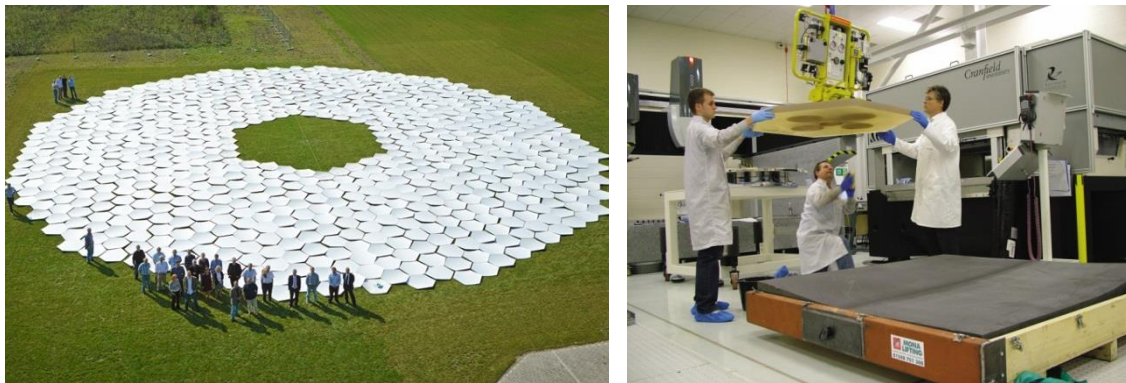


Figure 2-2 Segments of EELT: The size of EELT's primary mirror [4] (left); The prototype segment fabricated by Cranfield University (right)

2.1.4 Optical fabrication processes chain

Fabrication steps of large mirrors include grinding, polishing, surface figure correction. Cranfield University Precision Engineering Institute has proposed a process chain of three subsequent machining steps (Figure 2-3). The target is to reach a 20 hours cycle time for each step of surface generation[13].

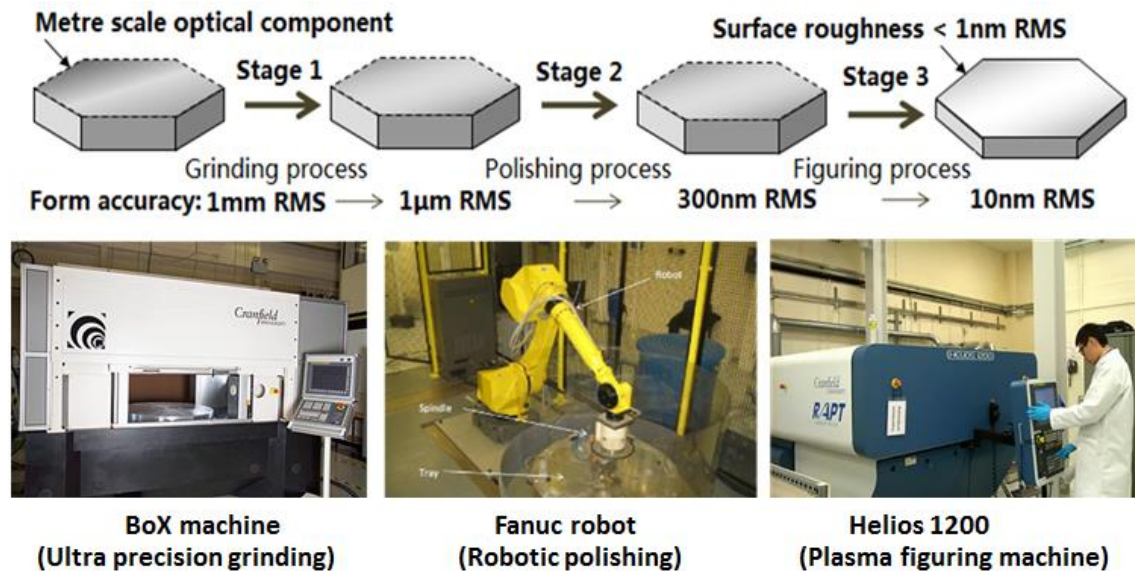


Figure 2-3 Rapid production chain for large scale mirror segment fabrication [13]

2.2 Surface figuring process based on plasma jets

Surface figuring is the final process to correct surface form errors. This takes place after the chemical-mechanical polishing processes. Figuring techniques are normally performed as the final step to remove the long spatial frequencies (form errors) and surface damages. Castelli has reviewed the Reactive Atom Plasma (RAP) figuring and other competing techniques used in optical fabrication, including Magnetorheological Finishing (MRF) [14], Ion Beam Figuring (IBF) [15], Fluid Jet Polishing (FJP) [16], Elastic Emission Machining (EEM) [17].

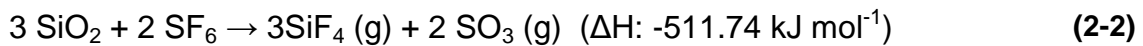
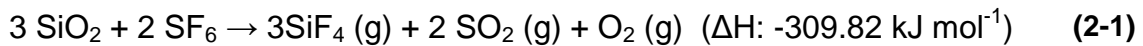
Chen [18] defined plasma as a 'quasi-neutral gas of charged and neutral particles which exhibits collective behaviour'. These moving particles may form concentrations of positive and negative charges that form local electric fields. The electrical current that is due to the movement of charges induces magnetic

fields at the same time [19]. Highly energized electrons collide with each other and consequently transfer thermal energy to surrounding atoms and ions. These three processes take place at the same time [20].

Section 2.2 introduces existing plasma figuring processes carried out at atmospheric pressure. These figuring methods have been developed for ultra-precision surface figure correction.

2.2.1 Chemical aspects

The optical materials mentioned in 2.1.2 are all silicon based materials. Fluorine or chlorine radicals are used to process those surfaces. The preferred reactive gases are Nitrogen trifluoride (NF₃), Carbon tetrafluoride (CF₄), and Sulfur hexafluoride (SF₆). O₂ is introduced sometimes together with those reactive gases to reduce the polymeric contaminations (CO_xF_y or SO_xF_y) by producing CO₂ or SO₂. In the project of this thesis, SF₆ was used and the chemical equation is given in (2-1) or (2-2) [21]:



From an energetic viewpoint, (2-2) is preferred over (2-1). Both of these two reactions are exothermic, but the energy released by (2-2) reaction is higher than (2-1). (2-2) produces more stable SO₃ molecule.

2.2.2 Toolpath algorithms

Castelli summarised different types of tool paths that can be used in deterministic finishing [22]. Apart from the most common raster-scanning and spiral tool-paths, randomised tool-paths investigation is emphasised by researchers to reduce the MSFs on a polished surface. A random pitch spiral path (Figure 2-4, left) was used in the MRF processing on a nucleated glass flat mirror with 100mm in diameter. No strong periodic feature in the Power Spectral Density (PSD) curve can be found in the result (Figure 2-4, right).

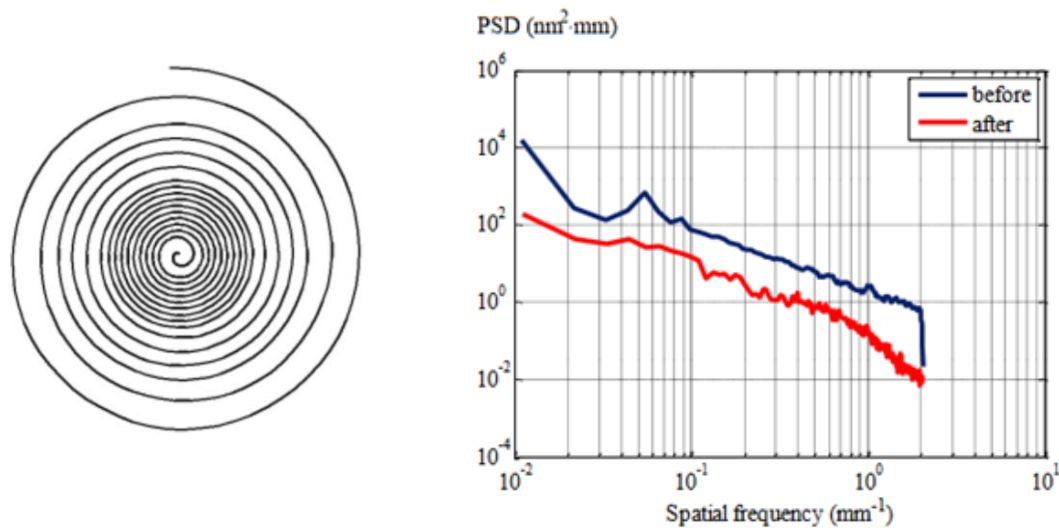


Figure 2-4 Schematic of random pitch spiral path (left) and PSD for random pitch spiral polished region (right) [23]

However, plasma figuring is strongly affected by heat variation comparing to IBF, MRF, and other sub-aperture polishing. The basis temperature of the whole substrate increases successively, leading to an increased material removal rate. Leibniz Institute for Surface Modification (IOM) applied a heat transfer simulation in the velocity map but kept the same raster scanning algorithm [24]. But this method is considered not applicable for large surface processing, as the simulation of large workpiece takes much longer time.

Castelli presented a reversed staggered rastering tool-path [22]. Figure 2-5 illustrated the first two loops of the tool path. The torch travels the raster-scanning path with a larger staggering step, and reverses the path until the whole surface is covered. This algorithm strategy could improve the homogeneity of thermal distribution of the substrate, and reduce the temperature gradient effects. ~30 nm PV form over 70mm length can be achieved using this tool-path.

have been proven to be machineable by RAP process [26],[27],[28],[29] from both RAPT Industries and Cranfield.

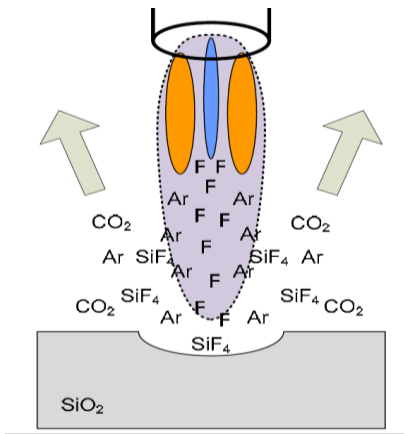


Figure 2-6 The RAP process on fused silica, using CF_4 in an argon plasma [30]

2.2.4 Plasma figuring process

Plasma figuring is a dedicated chemical fabrication process used to correct at nanometre level optical surfaces. A high-speed jet of plasma is blown onto the substrate surface. The reactive species react with the atoms of the surface. Volatile compounds are generated and flowed away [20]. Plasma figuring is a non-contact, sub-aperture, and deterministic process. It enables the rapid creation of a figure corrected and damage-free surfaces.

In 2003, the Precision Engineering Institute of Cranfield University purchased the first plasma figuring machine for fundamental research of the plasma figuring characterizations. The largest and most advanced plasma figuring machine is named Helios 1200 [29],[31]. This machine was built in 2008, through collaboration between RAPT industries and Cranfield University.

All of the research discussed in this thesis is based on work done within Helios 1200. This machine has a capability of 1.2 metres for processing scale. The substrate is held face downward so that the removed material or contaminations are prevented from re-deposition. In the 3 linear axes orthogonal machine, the substrate is held in a Y axis carriage (twin motor ball-screw drive), while the plasma torch scans in X axis (linear motor) with a raster-scanning route. The vertical Z axis controls the standoff distance between plasma torch and the

substrate. The machine transfers the time dwell map to the workpiece by adjusting the travelling speed along short distances when rastering [31].

The Fanuc 30i CNC motion system is adopted, together with a dedicated software package and a programmable logic controller (PLC), to ensure machine safety. The CNC system provides micrometre resolution of motion, and the software package manages the plasma delivery system, CNC system, as well as the safety features.

A fast figure correction process on 420 mm x 420 mm ULE was demonstrated in 2012 by Castelli [22,32]. Results are illustrated in Figure 2-7. 31 nm RMS form accuracy was achieved within 2.5 hours the original RMS figure error was 373 nm.

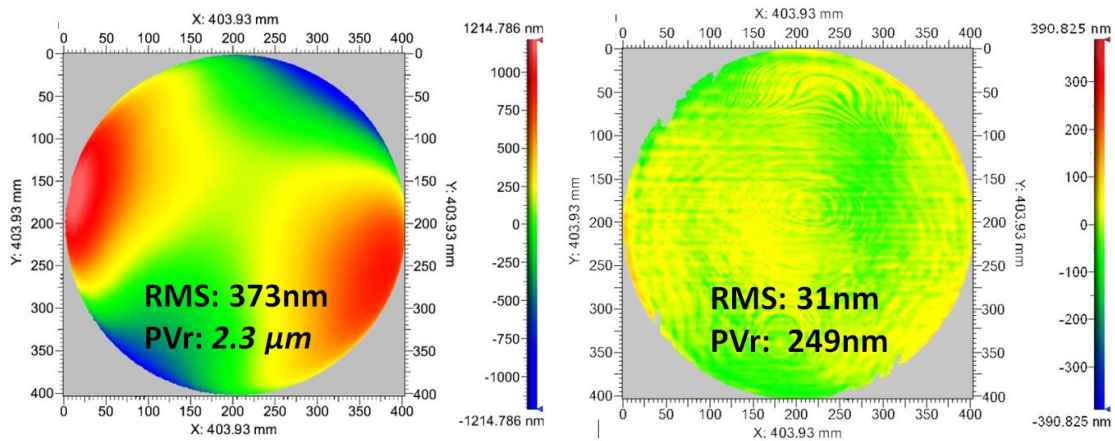


Figure 2-7 Topography of a 420x420 mm² ULE mirror before (left) and after (right) figuring within 2.5 hours [22]

In order to improve the surface figuring capability, additional research has started on a laser assistant plasma torch [33], optimal ICP torch nozzle design [34][35] and microwave generated plasma torch [36].

2.2.5 Plasma Chemical Vaporization Machining (PCVM)

Plasma Chemical Vaporization Machining is a patented process developed by Mori at Osaka University. His group published the basic concept and applications in 1993 [37], in which surface roughness of 0.5 nm RMS on Si single crystal and quartz glass was reported. Similar with PJM and RAP, PCVM

is a chemical machining method using neutral radicals generated by atmospheric pressure plasma. The plasma delivery system in PCVM is a type of CCP source. Plasma is ignited through the use of a central electrode driven by RF current at about 150 MHz. Halogen atoms with electronegativity are yielded in this very high frequency (VHF) plasma [37],[38],[39],[40],[41],[42],[43]. Comparing with a plasma etching process in LSI manufacturing, PCVM has much higher machining efficiency and is more deterministic [43]. It is because of the relatively higher pressure in the PCVM chamber (PCVM 650 Torr, about 1 atm; PACE 1-10 Torr), which allows a higher concentration of radicals to be yielded in the plasma. In the following 15 years, various shapes of electrode were developed for different applications, such as wire, plane, blade [37], pipe [38–41] and rotary electrode [42,43]. In more recent years, the development of open-air type PCVM operated with 13.56 MHz RF power leads to a more productive hybrid process named plasma assisted polishing (PAP). In the section, the pipe electrode type is the focus as it can be compared with the nozzle in the ICP torch investigation of this thesis.

Takino from Nikon Corporation has carried PCVM with a pipe electrode since 1997 [38]. The shaping method principle is illustrated in Figure 2-8 (left). Plasma is generated at the tip of the pipe electrode, while reaction gas is continuously supplied to the plasma through the pipe. A pipe shape electrode is easily managed for the supply of process gas and suitable for the removal of the target area, which makes a higher level of control. The typical shape of the footprint is provided in Figure 2-8 (right). Unlike the classical Gaussian shape footprint from PJM and RAP, this is a hollow form.

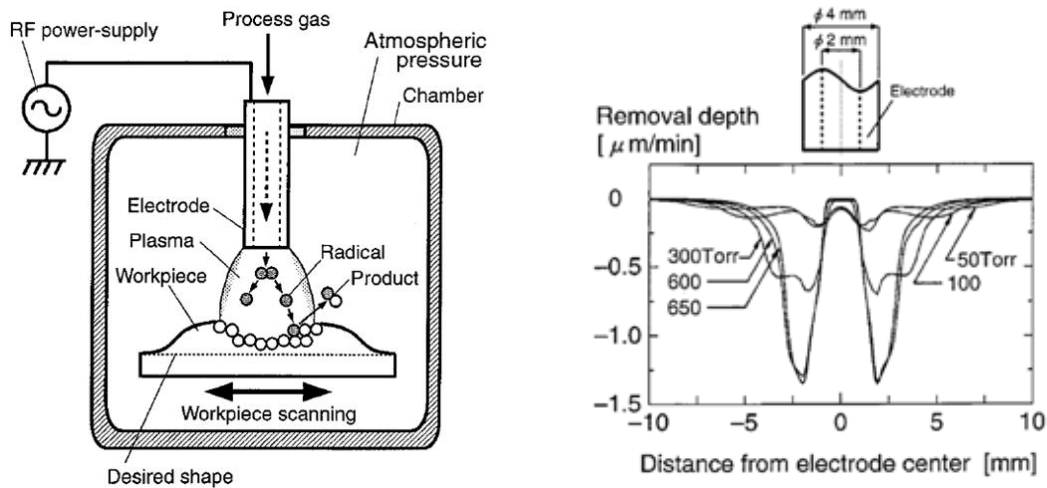


Figure 2-8 Schematic of the shaping method principle using pipe electrode (left) and its dedicated footprint under different intrachamber pressures [38]

The workpiece is loaded on a worktable, which is driven by a four axes platform (X,Y,Z linear axes and R rotary axis). For curved surface correction, another axis is introduced to enable the pipe to be tilted with an angle θ (Figure 2-9). The centre axis of the electrode is operated orthogonal to the surface. It has been proven that the tilt angle of the electrode and the thickness of the workpiece (distance between the electrode tip and worktable) do not affect the removal rate very much [39], as shown in Figure 2-10.

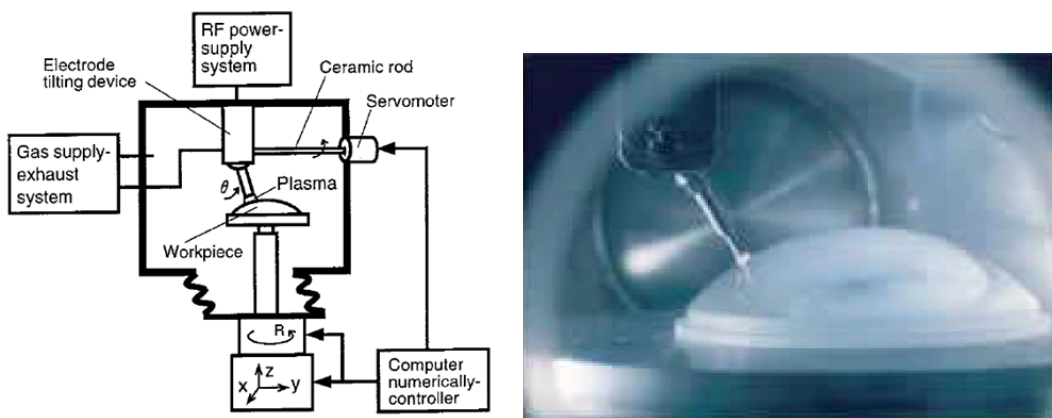


Figure 2-9 Schematic of the shaping of the workpiece with a curved surface [38](left) and its photo (from Nikon website)

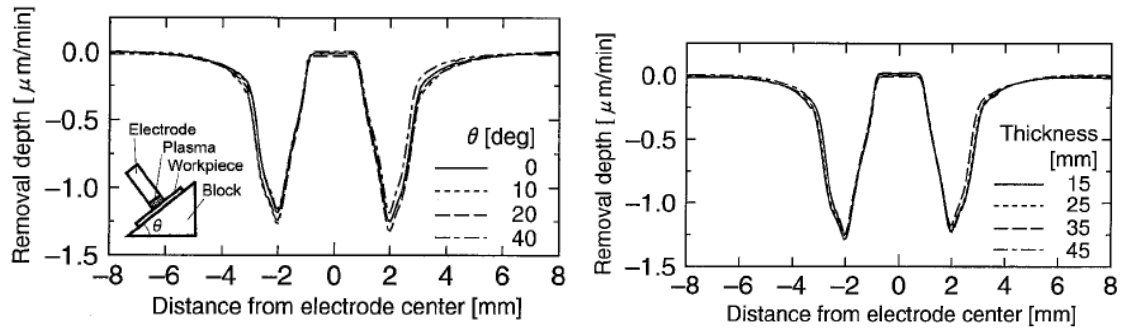


Figure 2-10 Cross section of footprint for different of tilt angles of electrode (left) and thicknesses of the workpiece [39]

The standoff distance is around 400 μm and footprint is about 6mm FWHM. Normally the footprint size is dependent on the size of pipe and the processing conditions. FWHM of the spot varies from 0.85mm to 10mm ([38–40,42,44]). Using a 12mm pipe, figure correction of an aspheric fused silica surface (160mm in diameter) was achieved to 130nm PV (form) and 0.37nm RMS (roughness) [39]. Also, the development of a sub-millimetre sized pipe was used for small complex shapes (Figure 2-11). In the latter applications using a pipe electrode, the process gas was drawn into the pipe from the chamber instead of blow out [40,44]. They proved that drawing in of the process gas realizes a smaller size of a footprint than the blowing out method. Anyway, the pipe electrode could particularly correct the errors in small areas, as the plasma is generated in the vicinity of the tip. Therefore, a smaller-diameter electrode is more effective and more deterministic but is usually utilized for the fine correction on small lenses.

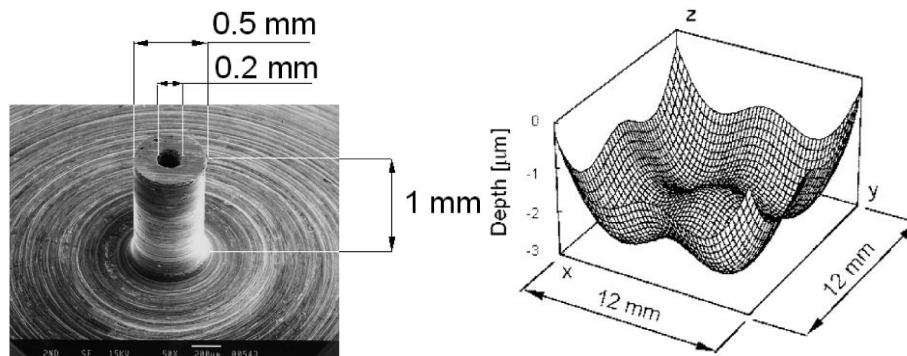


Figure 2-11 SEM image of the tip of microelectrode (left) and surface topography used for small complex-shaped optics (right) [40]

2.2.6 Plasma Jet Machining (PJM)

Plasma Jet Machining (PJM) is under development for the surface figuring and correction by IOM for about two decades. Collaborating with Carl Zeiss, Schindler's group leads the plasma processing investigation of a variety of optical materials in a rough vacuum environment in the mid-1990s (Ion beam etching [45], reactive ion beam etching [46], radical jet etching [47], plasma jet chemical etching [48,49]). PJM avoiding costly vacuum chamber has been reported since 2001 by Arnold and Boehm [15,24,50–57]. PJM is based on the chemical reaction of a non-thermal plasma jet driven either with microwave or RF power [50]. A schematic drawing of PJM is shown in Figure 2-12a. A mixture of reactive gas, e.g. CF_4 and SF_6 , and oxygen is used as other sub-aperture plasma figure methods. In the following 15 years, a variety materials (Silicon based: Si, SiO_2 , SiC , ULE; Metals like tungsten) have been tested. FWHM from 0.2 to 12 mm of the near-Gaussian shape footprint is reported in association with MRR range of $5 \times 10^{-5} - 50 \text{ mm}^3 \text{ min}^{-1}$ [50]. Usually, microwaves at 2.45 GHz are used (Figure 2-12b), but removing the short circuit used for microwave tuning also radio frequency at 13.56 MHz (Figure 2-12c) can be applied to the same configuration.

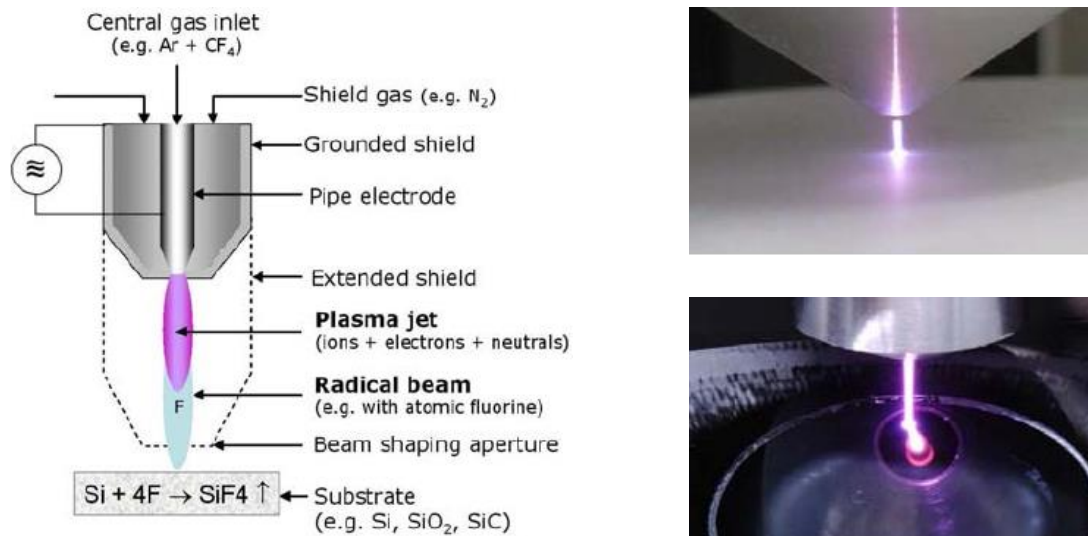


Figure 2-12 a) Schematic drawing of the PJM process [51]; b) Photo of microwave excited primary plasma jet in contact with a dielectric surface [55]; c) Photo of RF excited primary plasma jet in contact with a conducting surface [55]

Microwave driven plasma jet source covers a wide power range from 10W to 600W at 2.45 GHz. Arnold et al [51,55] present this type of torch where the plasma is generated by the injection of microwave energy. The setup (as shown in Figure 2-13) is the same as the one described in [24,58], where a coaxial waveguide system is employed. The difference here is that the gas supply is injected through an inner conductor that leads to a nozzle. The gas supply is a mixture of inert and reactive gases; typically helium is used as the inert gas in this example, however, argon is also a common carrier gas. The total gas flow rate is around 2.5 L min^{-1} , while reactive species was injected into the inert gas flow at a rate of 0.01 L min^{-1} (see Figure 2-13). This forms a stable and rotationally symmetric plasma jet discharge at atmospheric pressure. The setup in Figure 2-13 is also used for Mass Spectrometry. The size of the nozzle is around 8 mm in diameter as shown in Figure 2-14.

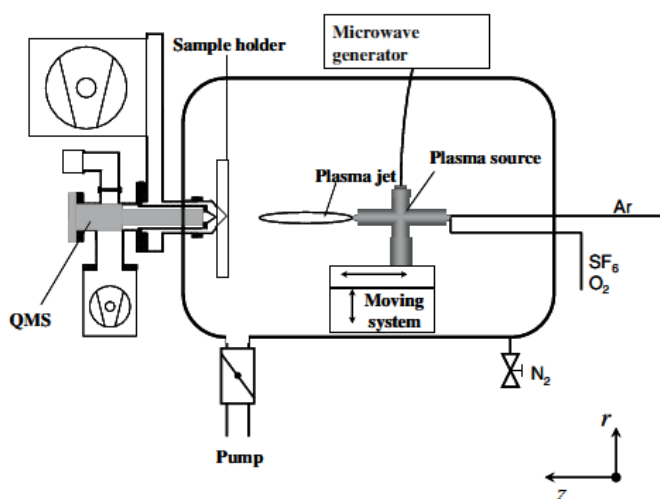


Figure 2-13 Setup of a microwave driven PJM facility [59]

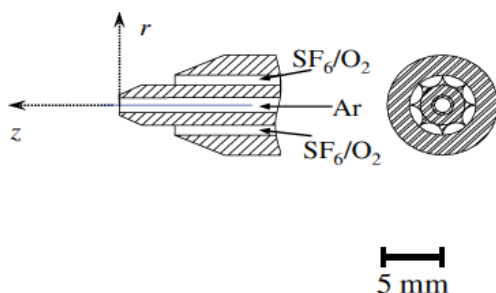
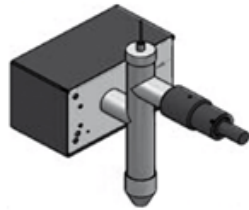




Figure 2-14 Setup of a microwave driven PJM facility [59]

Arnold reviewed PJM themselves in [50] with different types of microwave driven sources. The rough range of material removal rate and FWHM are listed in Table 2-2 depending on different sizes of plasma torches.

Table 2-2 Plasma jet sources (2.45 GHz microwave) for atmospheric plasma processing of surfaces, developed at IOM [50]

Source type	High power	Compact	Miniature
			
Weight (kg)	15	2	0.1
Max. power (W)	600	150	0.1
FWHM (mm)	2-12	0.2-2	0.2-1
MRR ($\text{mm}^3 \text{min}^{-1}$)	30	1	0.1

Paetzelt et al [56] demonstrated plasma-assisted chemical etching of crystalline silicon with a Radio Frequency generated plasma at atmospheric pressure. Helium gas was employed as the carrier gas and fluorine based reactive species was introduced to a helium plasma discharge. The standoff distance is 3.3 to 5.3 mm. The tool function of the plasma jet -FWHM- was measured to be in the range of 0.52mm to 1.8mm and presented Material Removal Rates of up to $0.068 \text{ mm}^3 \text{min}^{-1}$. The form accuracy of this 10mmx10mm substrate was achieved by PJM to 90nm PV from 1000nm PV within 17 minutes. This type of excitation is quite similar to the PCVM in terms of precessing parameters and results.

2.2.7 Other plasma figuring techniques

Harbin Institute of Technology of China has been conducting research onan APPP torch design since 2007 [60]. This research, so far, has concentrated on characterising the thermal, spectroscopic and material removal properties of the

plasma tool [61,62]. A surface roughness of 0.631 nm Ra was reported by Zhang et al, and the material removal rate on single crystal silicon wafers was reported to be $32 \text{ mm}^3 \text{ min}^{-1}$ [60]. The first and probably the only result of Zerodur figuring was reported in 2010 using the capacity coupled plasma jet [63]. The surface roughness of over 100 nm Ra proves again that the Zerodur with multiple phases and multiple composites is not suitable for plasma processing. Recently, surface investigations on fused silica using an ICP torch was carried out by Jin [64] and Xin [65].

The National University of Defence Technology emphasizes on improving the machining efficiency of SiC and presents their plasma etching method assisted by means of enhanced ion [66] and enhanced arc [67]. Experiment was carried out on a 100 mm diameter SiC surface. The shape error was corrected to 19nm RMS from initial 58nm RMS within 8 minutes. A maximum MRR of $0.35 \text{ mm}^3 \text{ min}^{-1}$ is obtained, which is about 10 times that of pure ICP etching.

2.2.8 Residual mid-spatial frequency errors

Surface errors are typically divided into three parts by spatial frequency: Low-Spatial Frequency (LSF), Mid-Spatial Frequency (MSF) and High Spatial Frequency (HSF) [68].

MSF errors can be corrected by both smoothing and figuring. The smoothing approach uses the smoothing effect from large stiff tools like a stressed lap. But as mentioned previously, contact machining will generate SSD and degrade the form accuracy. The other way is figuring approach, using smaller tools to correct the relevant frequencies. That means higher tool positioning accuracy is required to avoid roughness. However, this method may produce MSF errors again.

MSF observed on the residual error maps was analysed by means of Power Spectral Density (PSD) computation in Castelli's PhD project [22]. The average directional PSD is computed as the weighted average of single cross-sections PSD and is useful for evidencing peaks that match regular patterns in the surface figure error.

Figure 2-15 illustrates the PSD results of the optical surface processed in Cranfield. As marked in this figure, the curve peaks at the toolpath steps (6 mm and 9 mm), as well as twice their values. This phenomenon was considered due to the deep material removal in the second iteration, performed with a 9 mm staggering step.

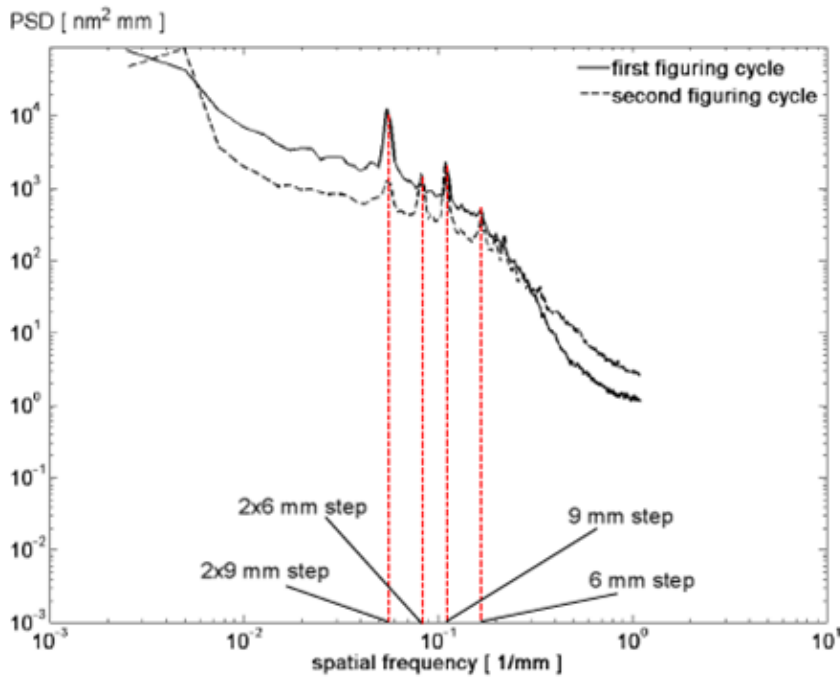


Figure 2-15 Figuring of 400 mm diameter areas: Average directional PSD plot of the residual error map Y-cross-sections for the figure correction over 400 mm diameter areas [22]

2.3 Atmospheric pressure plasma

Atmospheric pressure plasma is characterised by an extremely short mean free path (e.g. an Argon molecule travels a distance of 64 nm between two collisions [69]). The plasma at atmospheric pressure is dominated by particle collisions. Also, local thermodynamic equilibrium (LTE) is considered to be achieved, including kinetic and chemical equilibrium. In the context of plasma figuring, an atmospheric plasma enables the reduction of processing cost.

2.3.1 Radio frequency plasma torches

For the wide range of industry and laboratory applications, there are a large number of means to generate plasma. These include: dielectric barrier discharge, radio frequency (RF) signal, microwave signal, corona discharge, and so on [70]. This section focuses on atmospheric pressure plasma sources. RF signal are typically applied to capacitively coupled plasma (CCP) discharges (2.3.1.1) or inductively coupled plasma (ICP) discharges (2.3.1.2).

2.3.1.1 Capacitively Coupled Plasma (CCP)

CCP is largely used for industrial applications because it is robust. A typical CCP plasma system consists of an RF signal generator and a reactor that includes two electrodes. Figure 2-16 illustrates a schematic diagram of the RF CCP torch. One of the electrodes is connected to the RF power supply, while the other one is connected to the earth. The electrodes in the RF discharge are covered by sheaths, and the electrodes together with their sheaths forming a capacitor. The plasmas was generated using a free running type RF generator (275W, 27.12 MHz). The electron density is in the range of 10^9 - 10^{10} cm^{-3} [71].

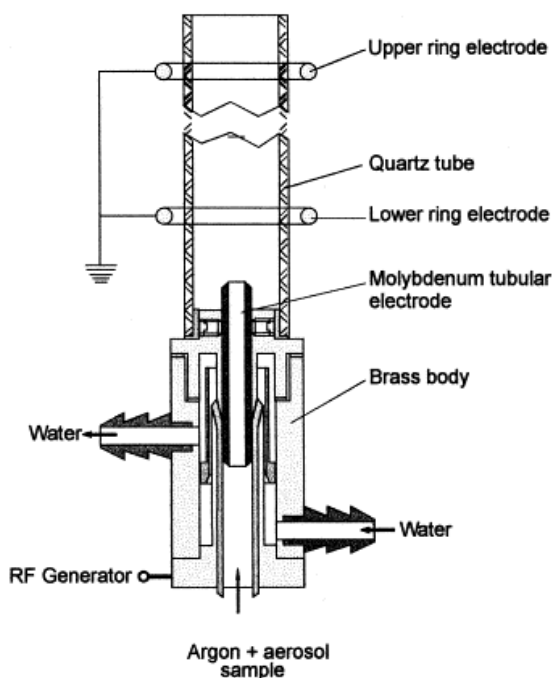


Figure 2-16 Schematic diagram of the RF CCP torch with central tubular electrode and two outer ring electrodes [72]

2.3.1.2 Inductively Couple Plasma (ICP)

Compared with CCP plasma, ICP is known as electrodeless plasma. Consequently the ICP discharge is free of contamination. In 1961, Thomas Reed invented the first induction plasma torch [73,74]. Atmospheric ICP torch designs have changed little since Reed's invention.

During the past 50 years, ICPs have been proven an extraordinary tool for material scientists [75,76] and surface engineers [77]. Researchers have investigated relentlessly the design and the use of inductively coupled plasma (ICP) torches for scientific and industrial purposes.

The electric currents produced by electromagnetic induction supplies the energy. When a time-varying electric current is passed through the coil, it creates a time-varying magnetic field around it, which in turn induces azimuthal electric currents in the rarefied gas, leading to the formation of plasma. Argon is one example of a commonly used rarefied gas [78].

The range of temperature is between 6,000 K and 10,000 K, which is comparable to the surface of the sun. The discharge of the ICP torch could generate a high-density of electrons (10^{15} cm^{-3}). Therefore, the ICP torches are widely used for applications that need a dense plasma, e.g. mass spectroscopy, sub-micron or nano-powders production, and spray coating or etching.

Figure 2-17 shows the log-log plot of density versus temperature. Some of the more important plasma domains are illustrated Hollahan and Bell [79], and in this image, one can find the "glow discharge" .

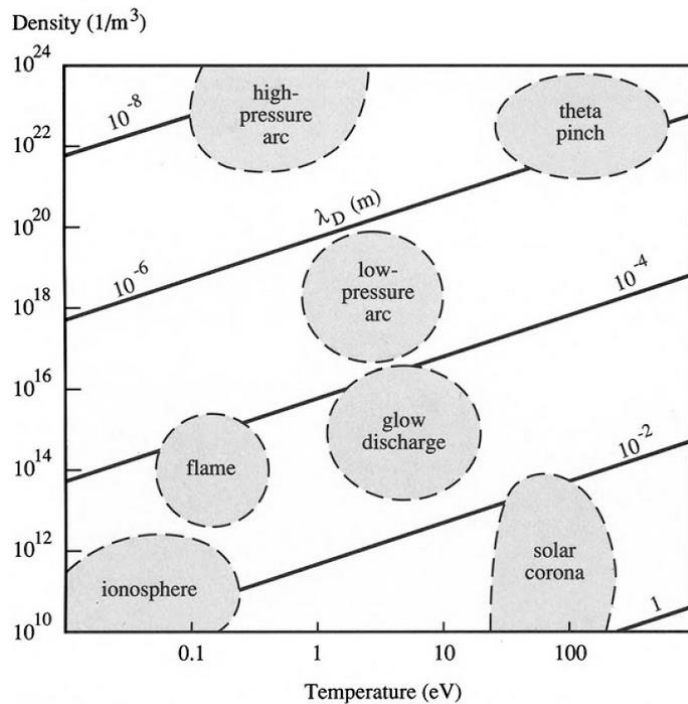


Figure 2-17 Approximate plasma domains [19]

At atmospheric pressure, the ignition is often achieved with the aid of a TESLA igniter. This device creates high-frequency and high voltage electric sparks that induce local arc-break inside the torch and stimulates a cascade through ionization of the plasma gas. The result is a stable plasma.

2.3.2 Plasma modes in ICP torches

The two plasma types are dominated either electric or magnetic fields. They are named E-mode (capacitively coupled or electrostatic discharge) and H-mode (inductively coupled or electromagnetic discharge) [80]. The E-mode plasma is characterized by a weak electron density [81].

For regular ICP torch, the E-mode plasma is originated by a voltage drop across the exciter coil. The H-mode plasma is characterized by the induced magnetic field. At atmospheric pressure, Razzak [82,83] reported the plasma images of the transition for Ar ICPs. He claimed that the E-H mode transition has very short transition time.

2.3.3 Mechanical design of the ICP torches

Generally, an ICP torch includes three parts: the coil, the confinement tube, and the gas distributor. Figure 2-18 illustrates the schematic diagram of a regular ICP torch and a photo the plasma discharge in the torch.

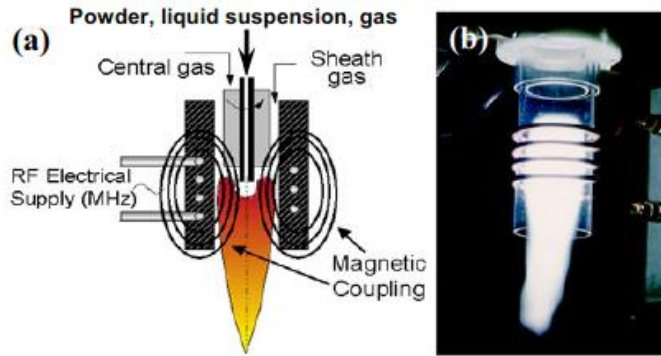


Figure 2-18 (a) Schematic diagram of the RF ICP torch; (b) Low power plasma discharge in air [84]

The induction coil consists of several spiral turns, depending on the RF power source characteristics. Coil parameters including the coil diameter, number of coil turns and radius of each turn.

The confinement tubes are adopted in an ICP torch so that the gas can be confined. The common implementation is a quartz tube being cooled either by compressed air or cooling water. However, this torch design, with poor mechanical and thermal characters, can be only used in low power (less than 30 kW). The high power plasma torches, with intense radiation, are made of the ceramic tube instead of transparent quartz tube [85]. Silicon Nitride (Si_3N_4) is adopted due to its better thermal conductive capability and thermal shock resistance. Industrial plasma torches with a greater size and power will choose metal when they take the power coupling efficiency and risk of chemical reactions into account. Figure 2-19 illustrates a commercial ICP torch manufactured by Tekna. This torch type of torch is used by many researchers [86,87].

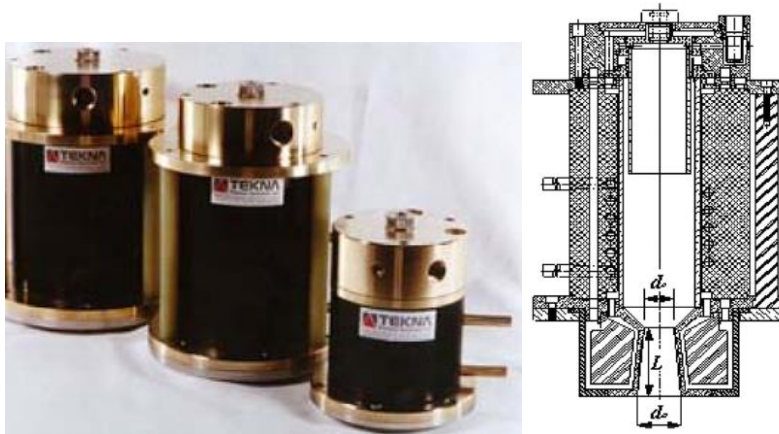


Figure 2-19: (a) Induction plasma torches manufactured by Tekna; (b) Cross-section of the Tekna torch equipped with a nozzle [88]

Figure 2-20 shows the bespoke ICP torch used in this PhD project. This assembly includes a regular ICP torch and a De-Laval nozzle.

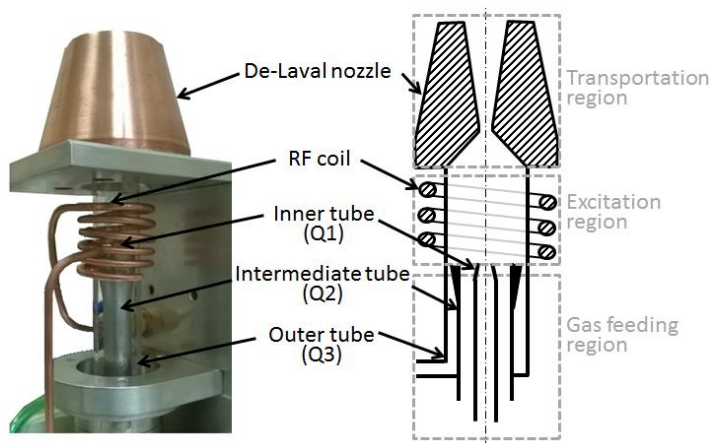


Figure 2-20 Bespoke ICP torch equipped with an original De-Laval nozzle

Figure 2-20 illustrates three gas tubes, which are marked as Q1, Q2, and Q3. The carrier gas is introduced into the torch with an inner tube from Q1. In the reactive plasma, carrier gas includes NH_3 , CH_4 , SF_6 , and oxygen. In the torch made by TEKNA, nano-powder is injected from Q1 [84]. The central gas is introduced into the torch as a swirling gas stream, so as to make sure the gas discharged in the proper axis of the torch. The swirling gas is generated from the intermediate tube Q2. Q3 is the sheath gas, going through the space between the intermediate tube and the quartz outer tube. Sheath gas can also

keep the flow stable for the plasma discharge, but its real function is to protect the confinement tube from the high temperature.

2.3.4 Plasma jet diagnostics of the ICP torches

The diagnostic tool of plasma jet is often used to derive the thermal footprint of the torch. Many of the previous studies on the temperature investigation of an ICP torch were conducted by direct measurement, including probe diagnostics and optical emission spectrometry (OES). Rahmane et al investigated enthalpy probe measurement in both ICP [89] and direct current plasma [90]. The obtained results with an enthalpy probe, which were compared with those from OES, and the plasma was cooled by less than 3%. This performance of the enthalpy probe was proven comparable with the laser scattering method carried out by Fincke [91]. Hopwood pioneered the use of Langmuir probe diagnostics for ICP basic parameters with an assumption of a Maxwellian electron energy distribution function (EEDF) [92]. Singh [93] studied the ICP RF discharges by means of a Langmuir probe comprehensively. More recently, Peterson [94] presented electron density measurements with a hairpin resonator probe. O'Brien applied OES measurement on the ICP torch used in Cranfield, to calculate the temperature distribution of the plasma jet [95].

However, the plasma torch (in this project) does not allow, within its application setup, the use of diagnostic tools mentioned previously. The main reason is that the space between torch nozzle output and the substrate is rather limited. Indeed, the ratio between the standoff distance and the nozzle outer diameter is 0.3. In practice, neither diagnostic probes nor OES methods can be implemented. In-direct measurements were undertaken to investigate heat transfer of the impinging jets. Kant estimated heat flux distributions by measuring the temperature distribution on the surface and applying inverse techniques [96]. Other investigations that quantify the heat transfer characteristics were also conducted [97,98] by Li and Dong.

Jourdain studied the heat transfer of a plasma jet onto optical components using an inductively coupled plasma torch [99]. The total power of 220 W was

absorbed by the substrate when the given RF signal was 1 kW. Then Jourdain claims that the temperatures can be predicted spatially and transiently.

2.4 Numerical analysis of ICP torches

To solve the problems of mathematical analysis, a numerical approximation is used instead of an analytical calculation. Continuous problems are replaced by a discrete problem, and the solution is to approximate the continuous problem. Iterative methods are commonly used to terminate in a finite number of steps after successive approximations. Finally, an accurate solution is found with a convergence test [100].

In order to describe the state of plasma, plasma modelling is carried out to solve the equations of motion. The main types of plasma models used in industry and in engineering applications are based on magneto-hydrodynamics (MHD). An experimental approach requires numerous costly and time consuming trial-and-error iterations. With advances in computational fluid dynamics (CFD) and computer hardware, CFD offers an alternative method for designing and understanding complicated flow control systems [101].

CFD aims to solve the governing equations in fluid mechanics using numerical analysis and a computer. CFD enables the prediction of the hot gas flows. The interactions of confined fluids with surfaces are modelled through boundary conditions. The procedures followed in CFD approaches, rely on specifications of geometry, meshing, appropriate boundary conditions and solving the equations of continuity, momentum and energy with an iterative solver.

CFD process requires the discretization of governing equations. Discretization methods in the numerical analysis include Finite volume method (FVM) [102], Finite element method (FEM) [103], Finite difference method (FDM) [104], Spectral element method, and Boundary element method to cite but few.

CFD software improves the accuracy and speed of complex simulation scenarios. Nowadays, there is a variety of commercial CFD software, such as ANSYS Fluent [105], COMSOL Multiphysics [106], CFD-ACE [107], Phoenix [108], CFX [109], Star-CCM [110], amongst many others. For the work

presented in this project, ANSYS Fluent package was chosen to perform simulations.

Previously, researchers investigated plasma modelling via MHD [111,112]. In this investigation, particular attention was given to the work of Proulx and Boulos who carried out a large amount of plasma CFD simulation research using a De-Laval nozzle [1,113–117]. A comparison between the De-Laval nozzle modelling and the cylindrical nozzle modelling was carried out. The temperature contours of the result are displayed in Figure 2-21. The De-Laval nozzle generates a supersonic plasma jet, consisting of alternating expansion and compression zones. By means of these zones, the static pressure tends to equilibrate with the ambient pressure (Figure 2-22). The axial velocity rises about one hundred times in the supersonic nozzle becoming much higher than in the subsonic jet (Figure 2-23). The supersonic jet performs faster transport of the reactive species from the torch to the substrate, providing smaller residence time and leading to the higher deposition rate. Unlike the situation in the subsonic jet, where the axial velocity begins to drop several centimetres before the substrate, in the supersonic flow, the axial velocity remains high until the near-substrate shock region, where it becomes subsonic.

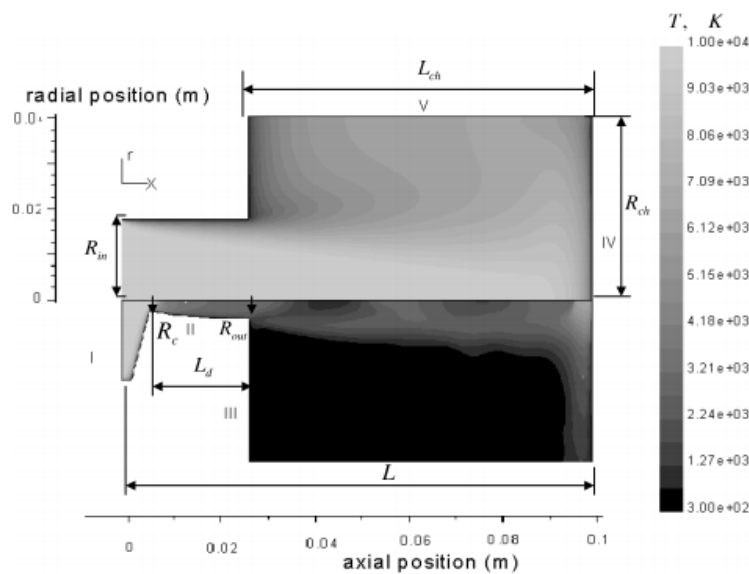


Figure 2-21 Heavy particles temperature contours in the supersonic and the subsonic jets [117]

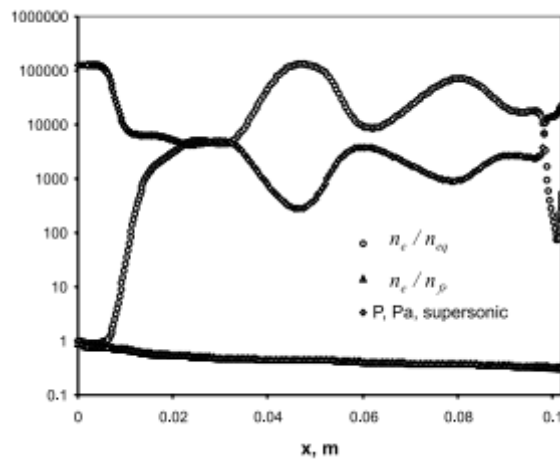


Figure 2-22 Ionization non-equilibrium degree [117]

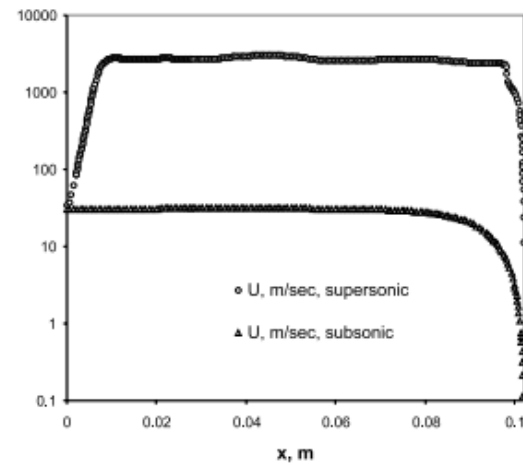


Figure 2-23 Velocity axial profiles in supersonic and subsonic plasmas [117]

Ding Li analysed the simulation of general fluids with the arbitrary equation of state and multiple components and multiple phases are outlined along with corresponding boundary condition methods [118]. The capabilities of the approach are demonstrated by nozzle flow calculations for four fluids with very different properties: air at normal pressures and temperatures where perfect gas assumptions apply, air at ultra-high pressures where real-gas effects dominate the solutions, argon expanded to low pressures where condensation and two-phase flow take place, and a purely incompressible fluid to demonstrate the method in this 'singular' limit.

As a more complex example of perfect gas flow calculations, we consider a modified nozzle with two separate inlet streams. In this calculation, CO₂ is introduced into the main inlet while air is introduced through an annular slot just upstream of the throat on the outside of the nozzle. The area of the slot is 20% of the total area. A splitter plate that extends nearly to the throat is used to guide the CO₂ into the nozzle and to insure parallel flow between the two gases. The details of the geometry are given in Figure 2-24. The goals of this calculation are to test the possibility of using a fluid with a different ratio of specific heats as a means of controlling the design Mach number of the main

flow in the nozzle while simultaneously demonstrating the computation of a mixture of perfect gases.

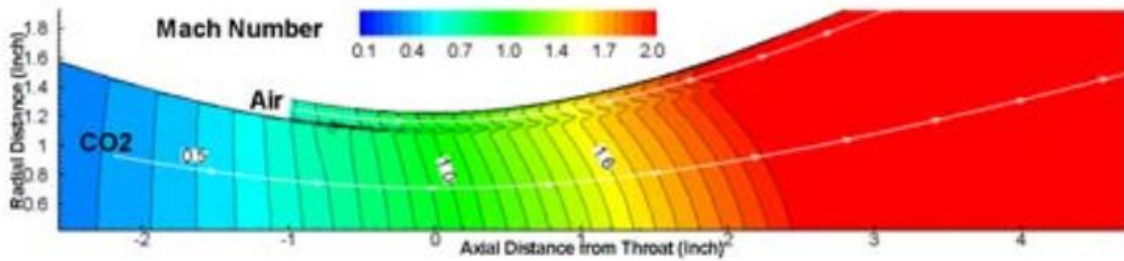


Figure 2-24 Details of annular slot for air injection and splitter plate in near-throat region showing Mach number distribution for CO₂/air flow combination [118]

Previous work has focused on the magneto-hydrodynamics of the plasma within the plasma core. Boulos and Mostaghimi [119,120] built 1-D models with laminar flow to solve the electromagnetic field equations. Nishiyama [121,122] reported that the secondary gas (cold helium) could control the temperature and flow field in Radio Frequency (RF) ICP. Colombo and Bernardi [123,124] have created both 2D and 3D models for investigating the effects of the torch geometries on the plasma flow and temperature distributions. In those aforementioned investigations, the operating power varied from 3 up to 10 kW, while the frequencies in all cases were set to 3MHz. Boulos and Nishiyama have successfully compared their modelling results with experimental data, in regards to radial velocity distribution [125] and axial temperature distribution [122]. Morsli and Proulx [1,126] validated their models by comparing calculated axial temperature profiles and discrete temperature measurements. In this thesis, the modelling method uses High Temperature Jet (HTJ) approach and considers Morsli's numerical plasma modelling as a reference for the validation.

2.5 Power dissipation of the ICP torch

In 1961, Reed stated that 45% of total input power (1.6 kW) was transferred to the plasma jet [73]. In 1969, Miller presented more accurate results about energy losses distribution using a novel analytical model [119]. He determined that 34% of the total input power (2.7 kW) was lost. In 1990, Chen [127] improved a 2D electromagnetic field formulation previously created by Boulos

[81] and predicted the heat flux and the temperature maps of an ICP torch plasma jet. The torch efficiency was 66 % and 33 % for a 1 kW and 3 kW input signal power respectively. This performance reduction was explained through the rapid enlargement of the core of the plasma. This enlargement leads to a rapid increase of the heat loss from radiation through the outer quartz tube.

The RF plasma torches reported in the aforementioned publications are too difficult to make a direct comparison. However, it seems reasonable to claim that roughly 50% of the input power is converted to the core of the plasma. Also, the loss within the torch is driven by radiation heat transfer mechanism. Whatever, the heat transfer to a substrate during surface processing is a different matter that these researchers did not address. Instead they created diagnostic tool and method to characterise the plasma jets for all sort of torches.

2.5.1 Infrared (IR) techniques for temperature measurement

Any matter with a temperature above 0K emits IR radiation according to its temperature. Stefan and Boltzmann illustrated that an unambiguous temperature can be measured from radiation signal [128]. The temperature change of an object is accompanied by a change of radiation intensity.

IR thermometry is a kind of noncontact temperature measurement device that offers 3 major advantages – fast (in the ms range), high temperature (over 1300°C) and no interference (electric conductive). However, the measuring target must be optically visible to the IR thermometry, and only surface temperature can be measured.

Infrared thermometers contain 4 major parts: Lens, spectral filter, detector (sensor) and electronics (amplifier/linearization/signal processing).

The optical path of the infrared thermometer is characterized by the ratio Distance to Spot size. The path is dependent on the lens' specification. The spectral filter selects the wavelength range (1 μm to 20 μm), which is relevant for the temperature measurement. The electronics transfer the thermal radiation intensity into the electrical signals.

The emissivity is a material constant factor, that to show the capability of the object to emit infrared energy. The emissivity (ϵ) ranges from 0 to 100% (blackbody). Normally, an emissivity determination is modified associating with a contact sensor (e.g. RTDs). The displayed measuring value will correspond to the contact measurement. For some specific reflective materials, a special plastic sticker will be used to increase the emissivity.

2.6 Summary

2.6.1 Summary of previous work

To meet the demand of meter-scale ultra-precise optical surfaces, atmospheric pressure plasma processes (RAP, PCVM, PJM, APPP) have been proven for fast surface figuring. In the Loxham optical lab of Cranfield University Precision Engineering Institute, RAP process has been carried out since 2003. Diagnostic and characterization of ICP torch were investigated, and dedicated toolpath algorithms were developed independently. The whole surface figuring on 420 mm x 420 mm ULE was demonstrated in 2012 and the metrology for this size optical surface was also developed. MSF was pointed out to be addressed as the next step of the plasma figuring research in Cranfield.

2.6.2 Identification of “Gap in knowledge”

In 2012, Jourdain et al scrutinised MSF of a 400mm diameter surface processed by the RAP torch. The investigation revealed a strong residual footprint due to the RAP plasma torch [129] (Figure 2-25). This surface structure was assessed and linked to the raster- scanning parameters and ICP torch nozzle design. Figure 2-25 highlights this surface structure showing the main spatial frequency and its harmonics.

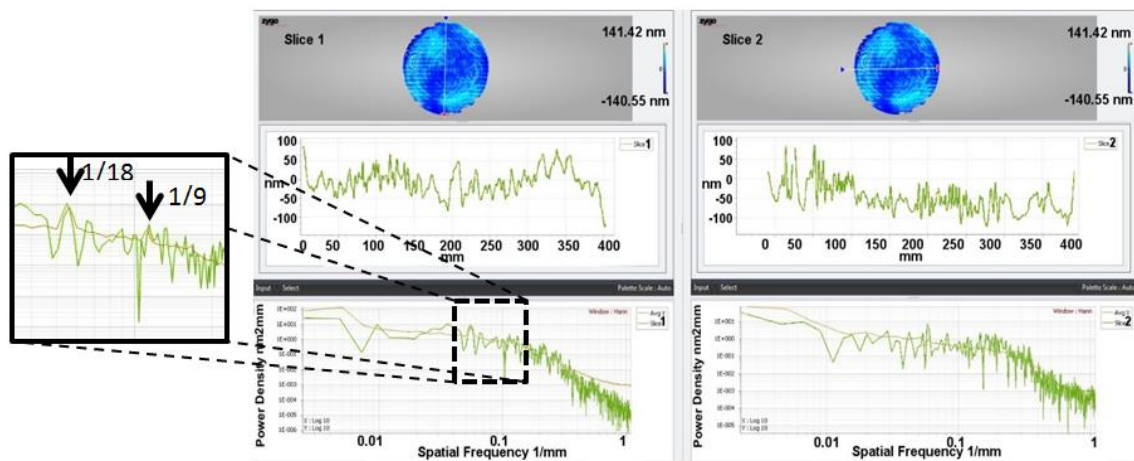


Figure 2-25 Surface topography showing the MSF features [129]

The purpose of the work presented in this thesis is to advance the plasma figuring of optical surfaces through the development of optimised ICP torches and associated nozzles. Highly collimated energy beams characterized by a material removal footprint in the range 1 to 5 mm FWHM and removal rate in the range $1\sim5\text{ mm}^3\text{ min}^{-1}$ are targeted. Thus, an entire understanding of the plasma jet in terms of its aerodynamic and thermodynamic behaviour needs to be addressed. Based on such understanding, a method to design and test the plasma torch nozzle is presented.

3 Methodology

To fill the gap of knowledge identified in 2.6.2, highly collimated and efficient plasma jet is aimed to be created through the development of De-Laval nozzle design. Four objectives were proposed (in Chapter 1) to realise this aim. Four work packages (WP) of investigation were carried out to achieve these objectives. This chapter explains how the investigation in each WP works and the logical relationship of each other. The logic diagram is given in Figure 3-1.

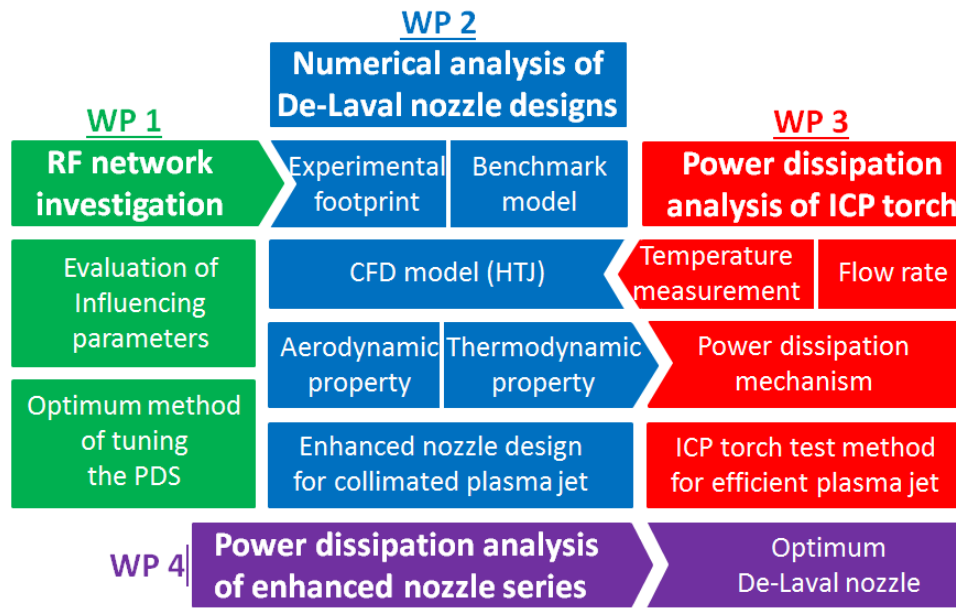


Figure 3-1 Logic diagram of the PhD project

WP 1 aims to achieve an optimum method for tuning the plasma delivery system (PDS). Through evaluating the impact of parameters in the RF network on the PDS, optimum parameters were found. This work enabled the experimental research (in WP 2, 3, 4) to be carried out efficiently.

WP 2 aims to understand the aerodynamic and thermodynamic properties of the De-Laval nozzle. A CFD model was created based on the high temperature jet (HTJ) flow. The input parameters come from the measurements carried out previously or from WP 3. The HTJ model was validated by a Benchmark model and previous experimental results of the material removal footprint. The output results of this HTJ model include the distribution of velocity, temperature, etc. This result was used to analyse the power dissipation mechanism (in WP 3)

later on. Finally, the HTJ model enabled a rapid design of a series of nozzles for highly collimated plasma jets. This series of enhanced nozzles were manufactured and tested in WP 4.

WP 3 aims to investigate the power dissipation mechanism of the bespoke ICP torch. High quality measurement of temperature and flow rate of the coolant was undertaken in a challenging environment. Experimental results enabled to calculate the power dissipation values for RF power up to 800 W and for the entire series of designed nozzles. Through the linear correlation between the power dissipation value and the RF power, the power dissipation of the ICP torch at 1200 W can be predicted. This work enabled an alternative method to test the nozzles rapidly (in WP 4).

WP 4 aims to select an optimum De-Laval nozzle providing a highly efficient plasma jet. By comparing the intensity of the power dissipation values, one nozzle was clearly identified as being more capable to provide highly efficient plasma jet.

4 Experimental setup and numerical approach

4.1 Experimental setup for the RF network investigation

4.1.1 Plasma delivery system (PDS)

In this section, the combined ICP torch, fixed matching RF network and the RF signal generator is named the plasma delivery system (PDS).

4.1.1.1 Fixed matching RF network

Figure 4-1(left) schematic shows the circuit diagram of the PDS. The PDS includes four main electrical components: RF power supply, transmission line, RF network, and plasma discharge region. The impedance is in the form of inductance, capacitance, and resistance as shown in the figure below.

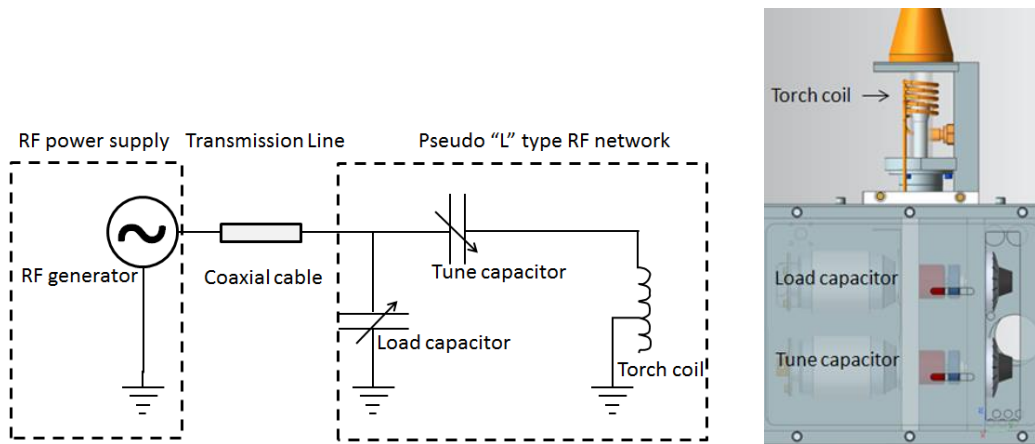


Figure 4-1 PDS schematic (left) and CAD model of the torch assembly (right)

Low impedance, properly selected length transmission is used for good power transfer. The transmission line is composed of coaxial cables, adapters, and connectors. The cable is an N male to N male cable using RG142 coax. The length of transmission line with no adapters is chosen by multiple of $\frac{1}{4}$ wavelength (λ), and λ is calculated as below:

$$\lambda = \frac{v}{f} = \frac{c\alpha}{f} \quad (4-1)$$

where λ is the wavelength of RF wave;

v is the wave speed, that can be calculated by multiplying velocity

- factor times the speed of light;
- f is the frequency of RF power, which is 40.68×10^6 Hz;
- c is the speed of light, which is 3×10^8 m s⁻¹;
- α is the velocity factor of coax, (the speed an RF wave travels along the coax cable relative to the speed in a vacuum), which is 69% (from Pasternack);
- λ is calculated as 5.0885 metres.

In this section, the three influencing factors shown in Figure 4-1(right) will be tested in the following subsections.

4.1.1.2 RF generator

The RF power supply is provided by a COMDEL CV2000/40.68 MHz RF generator. Optional frequency agile tuning technique is applied in this RF generator[130]. This RF generator has a power capability of 2000 W and it is designed for a 50 ohms load. The frequency can be swiped from 38.5 to 42.5MHz. The Reflected Power (RP) is limited to 20% of maximum Forward Power (FP). Hence impedance matching is important for RF power waves, as it is needed to provide maximum power transfer between the RF generator and the load coil. If more than 20% power is reflected back to the generator then the RF generator may be damaged.

4.1.1.3 Capacitors in the RF network

COMET capacitors were used in this PDS. Both tune and load capacitors are the same types – CVBA 250AC, with a capacity range from 5pF to 250pF. The capacitance per turn is 14 pF and the minimum adjustment for this capacitor is 1/100 turn (Figure 4-2). In the RF network of Helios 1200, the tune capacitance is set around 215pF, and the load capacitance is set around 40pF. One should notice that with tuning the same degree of the capacitor knob (1/100 turn), tune capacitance is changed 0.07%, while load capacitance is changed 0.5%. Frequencies were recorded from the display of the RF generator when one variable was set.

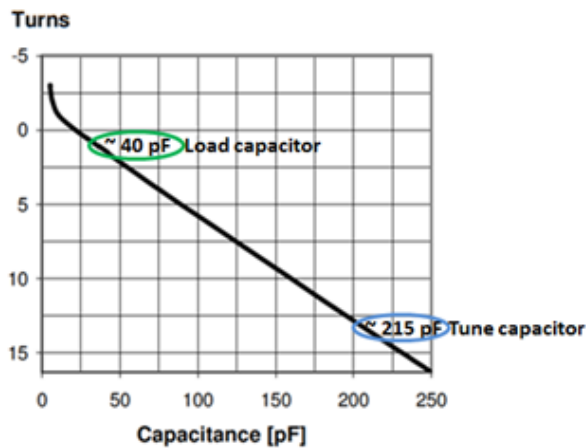


Figure 4-2 Correlation between capacitance and COMET capacitor knob

4.1.1.4 Torch coil in the RF network

Alternating currents from RF generator is supplied to the coil of ICP torch, and produces time-varying electromagnetic fields around the torch plasma. In turn, the azimuthal electric field is induced in the argon gas leading to the plasma generation (Figure 4-3). The RF coil is the last component in the electrical system used to generate an Argon plasma. There are three factors affecting the role of the RF coil in transferring energy:

- Geometry – being part of the RF system, the coil dimensions are important to the tuning of the circuit. Slight changes in dimensions can produce small changes in resistance or inductance and are normally compensated in the tuning circuitry of the system;
- Position – this includes concentricity and alignment. These are very important in producing correctly shaped plasma, which consistently needs to be located in the same position.
- Material – this includes base metal and plating material. The most efficient conductor of RF energy is pure silver followed by annealed copper. There is very little difference in the conductivity of these materials but there is a great deal of difference in cost. Copper is used as the base material of all commercially available coils but different manufactures use different plating materials. Silver has the best conductance and gold the best corrosion resistance.

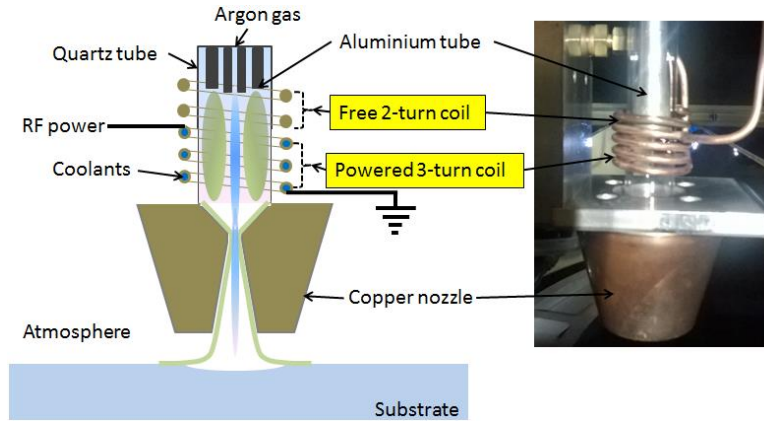


Figure 4-3 Photo of the ICP torch (right) and the cross-section of its schematic (left)

The torch coil adopted in Helios 1200 is a helical shape in cylindrical geometry (Figure 4-3, right). This coil is made of copper and composed of two parts: free 2-turn coil and powered 3-turn coil (Figure 4-3, right). The free turns are solid copper, while the powered 3 turns are hollow for coolant purpose.

Comparing with most common fully loop coil, this design is considered to ease the ignition of the plasma (higher electron density). Any change of the coil could result in the significant change of plasma impedance. The inductance of a round wire coil is determined by dimensions in Figure 4-4, according to Henrys:

$$L_{coil} = \mu \pi D^2 N^2 / 4l \quad (4-2)$$

where L_{coil} is the inductance of the coil;
 μ is the constant of proportionality;
 D is mean diameter of the air core coil;
 N is number of turns;
 l is the length of the coil.
 λ is calculated as 5.0885 metres.

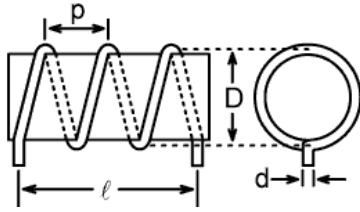


Figure 4-4 Round wire coil with dimensions [131]

The coil's variables in this section include the length of the coil and the number of free turns.

4.1.1.5 ICP torch

The ICP torch under investigation can be divided into three regions: gas feeding, excitation, and transportation (Figure 4-5). The gas feeding region ideally provides a consistent supply of gas through three coaxial tubes whatever the operating conditions. The gas supply value and type are provided in section 2.5. Radio frequency (RF) power is transferred to the helical coil by applying an alternated current. Gas ionisation is created in the excitation region where the plasma core temperature is about 10,000 K [132]. A De-Laval nozzle is equipped with the ICP torch for securing plasma transportation. This nozzle enables the amendment of plasma jet characteristics in terms of velocity, temperature, and footprint dimension. This engineering artefact is highly convenient as it is used to tailor the jet footprint without occurring engineering modifications of the ICP torch.

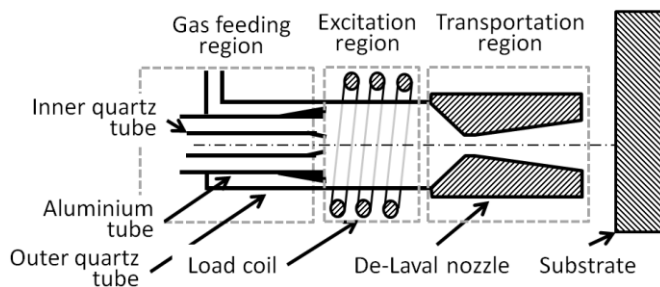


Figure 4-5 ICP torch regions and part names

4.1.1.6 Gas supply

Argon gas was provided to the plasma torch using analog mass flow controllers (MFC) from Brooks. In fact, three MFC were used as there were three coaxial

tubes to feed. These MFCs were utilized to control and monitor the gas flow supplied when the RF forwarded power was ramped up from 250 W up to 800 W. In the experiments, the total nominal gas flow of argon was set to 20.2 L.min⁻¹. However, this nominal value was not reached by the MFC as shown Figure 4-6. These results were obtained through a series of six experiments for which forwarded power was ramped up through 100 W steps. Logged values showed an increase of 0.45 L.min⁻¹ for 800 W forwarded power. The mean deviation from the nominal gas flow is within 2.22%.

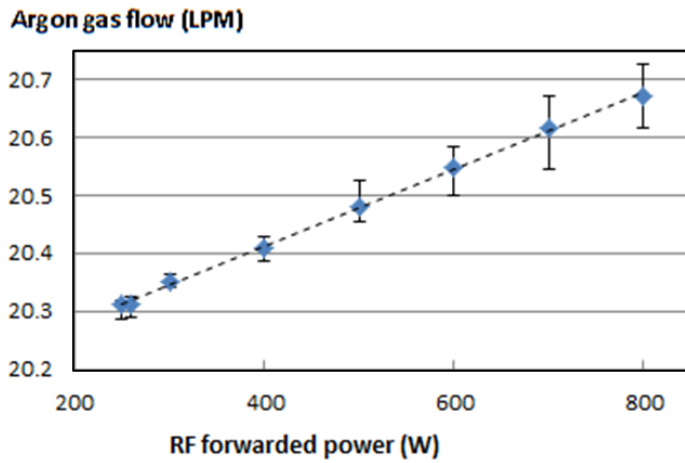


Figure 4-6 Argon flow rate versus forwarded power

4.1.1.7 Coolant supply

Coolant was provided to the plasma torch using an industrial water chiller (TAEevo Tech 051). The distance between the chiller and the machine was 10 m. The total amount of the coolant (tank and pipe) is 115 L. Figure 4-7 shows the thermal cycle logged during two hours duration. The amplitude of the variation is 3.5 °C and the period of the chiller cycle is 30 minutes.

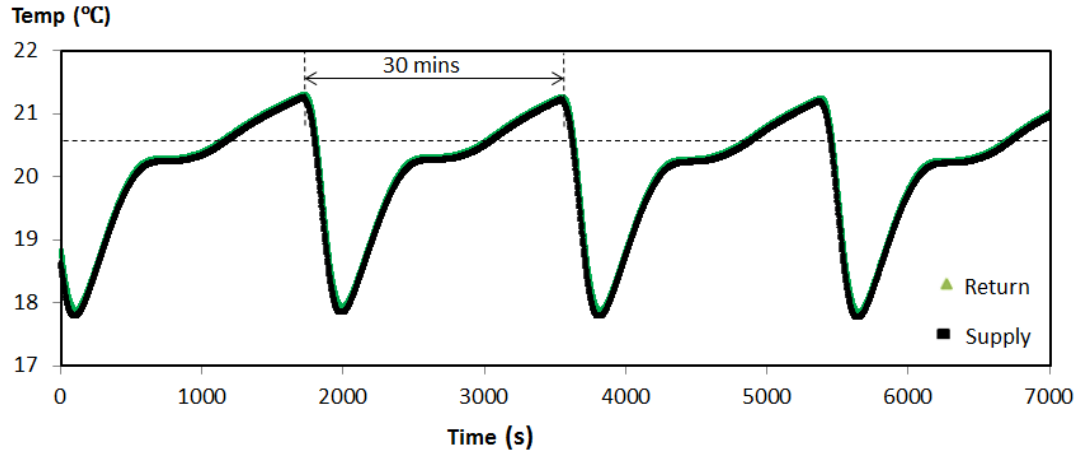


Figure 4-7 Coolant temperature variation for a two hour period

4.2 CFD model creation and validation

4.2.1 CFD Modelling approach for High Temperature Jet

Numerical simulations are carried out in this section to investigate and understand the dynamics of the High Temperature Jet (HTJ) flow. The assumptions and simplifications are as follow.

4.2.1.1 Modelling hypothesis

The main modelling assumptions adopted are:

- The HTJ flow is axisymmetric, steady, and turbulent;
- The effect of EM fields is negligible;
- Viscous dissipation is taken into account;
- The Local Thermal Equilibrium (LTE) is achieved;
- The HTJ is thermally expansible and mechanically incompressible.

4.2.1.2 Governing equations

We have considered a steady state regime with a 2D axisymmetric model based on an HTJ that is governed by the Navier-Stokes equations, conservation of momentum, mass and energy transport. The nomenclatures are provided with those governing equations.

Continuity equation

The mass balance in the axis-symmetric frame (r, z) is expressed by

$$\frac{\partial(\rho v_z)}{\partial z} + \frac{1}{r} \frac{\partial(\rho r v_r)}{\partial r} = 0 \quad (4-3)$$

where ρ is the gas density;

v_z is the gas velocity in axial directions;

v_r is the gas velocity in radial directions.

Momentum equation

The axis-symmetric momentum balance in cylindrical coordinates is given by

$$\rho \left[\frac{\partial v_z}{\partial z} v_z + \frac{\partial v_z}{\partial r} v_r \right] = -\frac{\partial p}{\partial z} + \frac{\partial}{\partial z} \left[\mu \left(2 \frac{\partial v_z}{\partial z} \right) \right] + \frac{1}{r} \frac{\partial}{\partial r} \left[\mu r \left(\frac{\partial v_r}{\partial z} + \frac{\partial v_z}{\partial r} \right) \right] \quad (4-4)$$

$$\begin{aligned} \rho \left[\frac{\partial v_r}{\partial r} v_r + \frac{\partial v_r}{\partial z} v_z \right] & \quad (4-5) \\ & = -\frac{\partial p}{\partial r} + \frac{\partial}{\partial r} \left[\mu \left(2 \frac{\partial v_r}{\partial r} \right) \right] + \frac{\partial}{\partial z} \left[\mu \left(\frac{\partial v_r}{\partial z} + \frac{\partial v_z}{\partial r} \right) \right] + \frac{2\mu}{r} \left(\frac{\partial v_r}{\partial r} - \frac{v_r}{r} \right) \end{aligned}$$

where p is the the pressure in the nozzle;

μ is the viscosity of gas.

Enthalphy equation

The axis-symmetry enthalpy equation in cylindrical coordinates is

$$\rho \left[\frac{\partial h}{\partial r} v_r + \frac{\partial h}{\partial z} v_z \right] = \frac{\partial}{\partial z} \left(\frac{\lambda}{c_p} \frac{\partial h}{\partial z} \right) + \frac{1}{r} \frac{\partial}{\partial r} \left(r \frac{\lambda}{c_p} \frac{\partial h}{\partial r} \right) + U_P - U_R + U_C \quad (4-6)$$

where c_p is the specific heat at a constant pressure;

λ is the thermal conductivity;

U_P is the local plasma energy dissipation rate (Joule heating rate);

U_R is the volumetric radiation heat losses (Radiation losses per unit volume);

U_C is the heat of chemical reaction;

h is static enthalpy.

For ideal incompressible gas, the static enthalpy $h = \sum_j Y_j h_j$, where Y_j is the local mass fraction of species j , and h_j is the enthalpy of species j . In the case of the present work, using the hypothesis mentioned above, U_P and U_C is counted as 0.

4.2.1.3 Turbulence characteristics

The characteristic of plasma flow is estimated on the basis of the Reynolds number and additional information from the literature. $Re = \frac{\rho v D_H}{\mu}$, where ρ is the density of the fluid [133], v is the mean velocity of the fluid, D_H is the hydraulic diameter of the nozzle, μ is the dynamic viscosity of the fluid [134]. These parameters were considered at the inlet of the nozzle. Due to the wide range of parameter values, the Re numbers range from 3800 to 10350. This Re result suggests that the flow is in a transition state with both turbulent and laminar transports [135]. On the other hand, Morsli [86] reported that the turbulence is present in the cooler regions (below 5000 Kelvin) of ICP torch jets. Also it is detailed that the laminar flow is promoted due to the lower densities and higher viscosities at the centre of the plasma stream (above 5000 Kelvin).

In the case of the present work, the temperature of the HTJ is below 5000 Kelvin [22]. Then the HTJ jets' turbulent behaviour is described using the standard k - ε scheme [136]. This turbulence model is used because it is accepted practice and it offers a balance between accuracy and speed of convergence. Also for computing Reynolds stresses two additional transport equations were solved. Kinetic turbulent energy k and its dissipation rate ε equations are shown in (4-7) and (4-8).

$$\frac{\partial(\rho k u_i)}{\partial x_i} = \frac{\partial}{\partial x_j} \left[\left(\mu + \frac{\mu_t}{\sigma_k} \right) \frac{\partial k}{\partial x_j} \right] + G_k - \rho \varepsilon \quad (4-7)$$

$$\frac{\partial(\rho \varepsilon u_i)}{\partial x_i} = \frac{\partial}{\partial x_j} \left[\left(\mu + \frac{\mu_t}{\sigma_\varepsilon} \right) \frac{\partial \varepsilon}{\partial x_j} \right] + C_{1\varepsilon} \frac{\varepsilon}{k} G_k - C_{2\varepsilon} \rho \frac{\varepsilon^2}{k} \quad (4-8)$$

The quantities of $C_{1\varepsilon}$, $C_{2\varepsilon}$, σ_k , and σ_ε are empirical constants [137]. The turbulent viscosity μ_t involves a constant $c_\mu=0.09$ and is derived from k and ε , as shown in (4-9):

$$\mu_t = c_\mu \rho \frac{k^2}{\varepsilon} \quad (4-9)$$

The source term of turbulence G_k is function of turbulent viscosity and stresses, as shown in (4-10):

$$G_k = \mu_t \left(\frac{\partial u_i}{\partial x_j} + \frac{\partial u_j}{\partial x_i} \right) \frac{\partial u_j}{\partial u_i} - \frac{2}{3} k \frac{\partial u_i}{\partial x_i} \quad (4-10)$$

4.2.1.4 Initial validation of modelling approach

The plasma model published by Morsli and Proulx [86] is considered as a benchmark. The geometries of the torch, nozzle and chamber of this model are shown in Figure 4-8. The other boundary conditions (BC) were applied identically. However, the approach of HTJ deals with a computational domain that is different from the domain used in Morsli's model. The domain used in HTJ approach does not include the ICP torch domain.

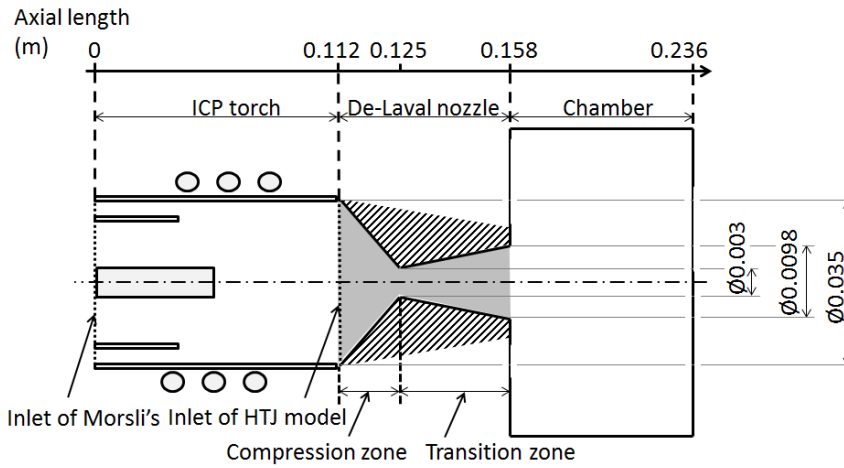


Figure 4-8 Computational domain in [86]

BC related with the geometry of this model and include nozzle inlet diameter: 0.035m, nozzle throat diameter: 0.003m, the length of the convergent path: 0.012m. BCs related to temperatures are nozzle wall: 700K, chamber wall: 300K. In addition, this simulation used the three main results of Morsli's work. Results are the axial distributions of inlet pressure, inlet temperature and gas flow rate. These input axial parameters located at the entrance of the nozzle are inlet pressure: 27,000Pa, inlet temperature: 6000K, gas flow rate: $3.58 \times 10^{-3} \text{ kg.s}^{-1}$.

In their research, Morsli highlighted that the distributions of pressure and temperature exhibit important variations along the central line of the torch. Depending on the position along the central line, these variations are either smooth or abrupt. Two zones of interest are identified. These are named “Compression zone” and “Transition zone” and are illustrated in Figure 4-8 and mentioned again in Figure 4-9.

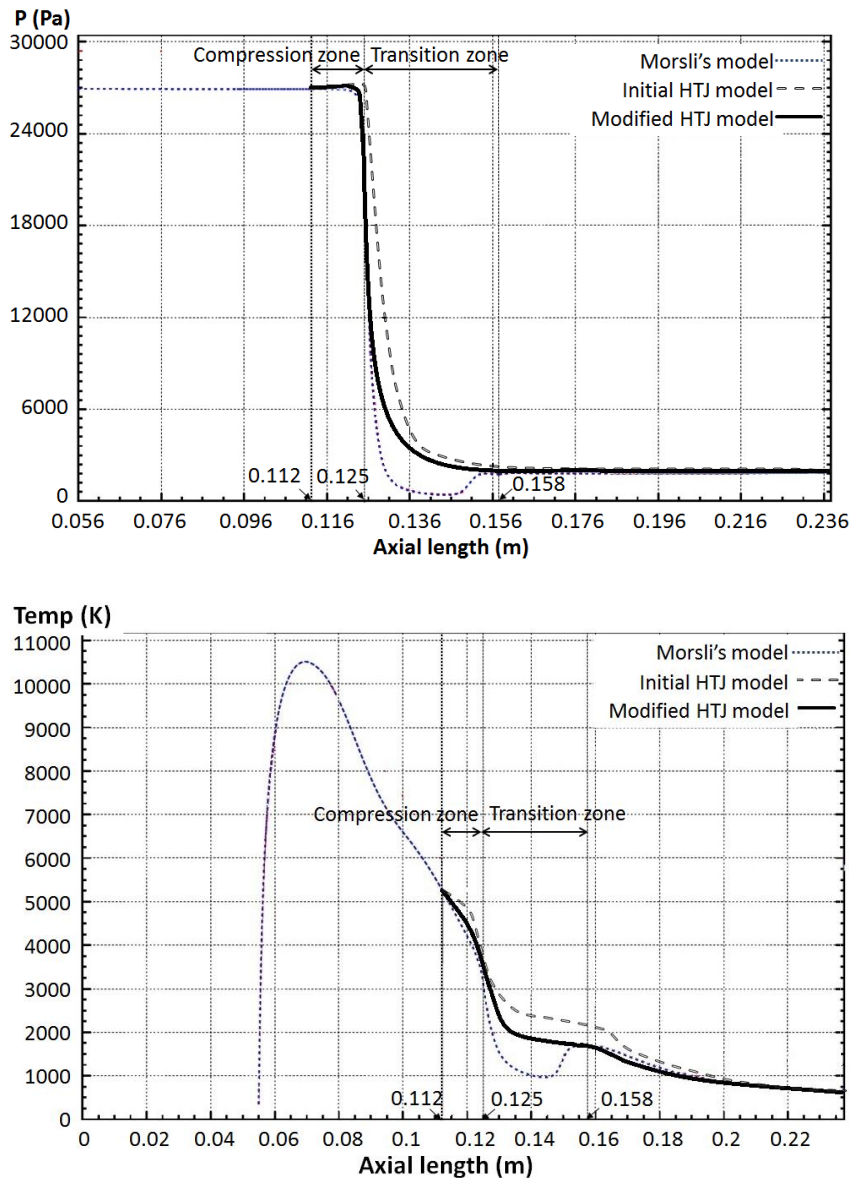


Figure 4-9 Correlation between benchmark model [86] and author's validation models. Top: axial pressure profiles; Bottom: axial temperature profiles

In this work, two models were implemented. The results obtained with the two models are displayed in Figure 4-9 along with Morsli's results. The characteristic and the relative error values are provided hereafter.

The first model referenced as 'initial model' is characterised by a uniform inlet profiles of temperature and velocity. The second model referenced as 'modified model' uses parabolic profiles for temperature and velocity. The use of parabolic profiles allows to obtain better results as shown in Figure 4-9.

In order to measure the discrepancy of the results obtained to the benchmark's, the approach adopted to calculate the relative error δ is as follow; let $\psi_{\text{ben}}(i)$ be any field (pressure, temperature, etc.) obtained from the benchmark model, and $\psi_{\text{act}}(i)$ be its counter-part field estimated with the actual model, these are measured at positions i , then

$$\delta = \frac{\sum_i |\psi_{\text{ben}}(i) - \psi_{\text{act}}(i)|}{\sum_i \psi_{\text{ben}}(i)} \quad (4-11)$$

In the initial model discrepancy on the axial pressure and temperature is estimated to be $\delta = 15$. In comparison, the error in the modified model is reduced to $\delta = 5$.

Regarding these two zones of interest, a detailed comparison is presented hereafter. Compression zone is where flow acceleration occurs. In this zone - Axial length: 0.112m to 0.125m in Figure 4-9 -, pressures slightly built up and temperatures drop further. The modified model shows a clear correlation with Morsli's results. On the other hand, the Transition zone results - Axial length: 0.125m to 0.158m in Figure 4-9 - highlight some discrepancy with Morsli's model. This discrepancy is attributed to the dependency of the pressure and the chemical composition of plasma in Morsli's model. Unlike in Morsli's model, the equation of state in this modified model is not dependent of the constituents. Indeed this model contained only one constituent.

The pressure and temperature profiles are in good agreement with Morsli's model. Based on the aforementioned comparison, the modified model was

considered sufficiently valid to investigate the study case presented in the next section.

4.2.1.5 Boundary conditions and numerical procedure

The computational domain is shown in Figure 4-10. The composition of the HTJ is a mixture of argon and 0.4% SF_6 . This gas mixture (Ar , Ar^+ , SF_6 , F^- , e^-) is fed into the nozzle through the upper aperture and it flows downward in an axisymmetric manner. From this aperture, the input parameters include: flow velocity profile, temperature profile, and pressure. The input temperature of the upper aperture ranges from 1000 to 6500 Kelvin as supported by the measurement of O'Brien [95]. The gas mixture flow rate is 22 l min^{-1} . The corresponding gas mixture velocity in the nozzle inlet is 25.77 m s^{-1} . This value was estimated from the Rankin-Hugoniot relation. For the sake of simplicity, the temperature of the Fused Silica substrate is set to 400 Kelvin uniformly. And wall temperature of the nozzle is 350 Kelvin. The static pressure in the processing chamber is set 101325 Pa (outlet side). Also, the gas temperature of the chamber is 300 Kelvin.

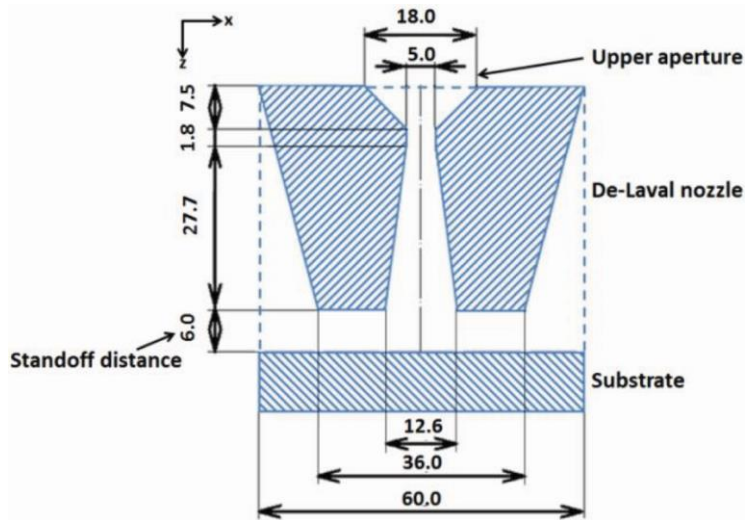


Figure 4-10 Computational domain of the model and its geometry (unit mm)

A coupled implicit solver for the Navier-Stokes equations was used to deal with the strong coupling of momentum and energy equations. The convergence criterion was set to 10^{-5} . The mesh sensitivity was performed to reduce

discretisation errors. The dimensions of the De-Laval nozzle and the standoff distance between the nozzle and the substrate are displayed in Figure 4-10.

4.2.2 Set-up for material removal footprint experiment

In order to assess the correlation of the model output with the actual plasma removal process, a set of footprint material removal experiments were carried out previously by Jourdain and Castelli. Footprints were characterised by two parameters. The first parameter is 6-sigma (mm) value which related to the width of material removal footprint (as shown in Figure 4-12). The second parameter is the depth (nm) of the footprint. The experimental results are compared to the numerical results in 5.2.1.3.

4.2.2.1 Experimental set-up

The ICP torch was moved in a plane parallel to the surface 200mm x 200mm of a substrate. The substrate was made of Fused Silica. Brass masks were used (Figure 4-11, left) for reference purposes to ensure these two regions were etched free. Picture of both substrate and ICP torch is shown in Figure 4-11 (right).

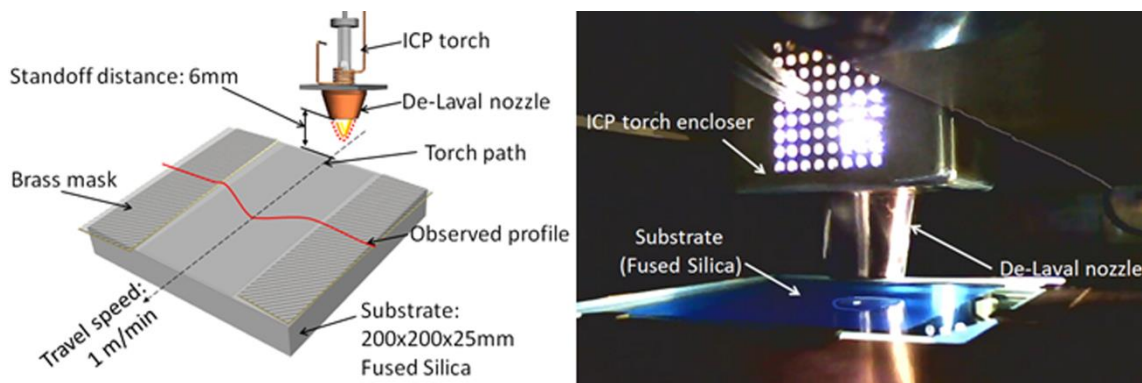


Figure 4-11 Schematic of the torch path (left), picture of both substrate and torch (right)

Key experimental conditions include: RF signal frequency 40MHz, plasma forwarded power 1.2 KW, the travel speed of the torch 1 m min^{-1} , and reactive gas $\text{-SF}_6\text{-}$ concentration 0.4% in argon. A series of single trenches were etched on substrate surfaces. The surface topography -100mm diameter area- was measured using a Twyman-Green interferometer - FISBA Optik $\mu\text{-Phase}$ - [22].

Subsequently, a series of trenches were carried out with different standoff distances. The experimental results are detailed hereafter.

4.2.2.2 Footprint of the ICP torch

For standoff distance equal to 6mm, the profile of the etched footprint (Figure 4-12) was assessed to be near Gaussian, and the 6 sigma value was determined to be 31 mm. The maximum depth of the trench was 120nm. When the standoff distances were changed, different footprint depths were observed. The influence of the standoff distance on the maximum depth can be seen in Figure 4-13. The beam footprint characterization was published in [31]. In this work, the footprint data will be utilized to validate the CFD simulation results.

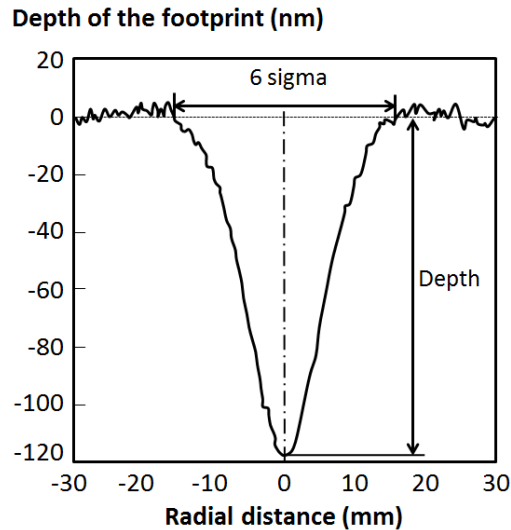


Figure 4-12 Cross section of the trench

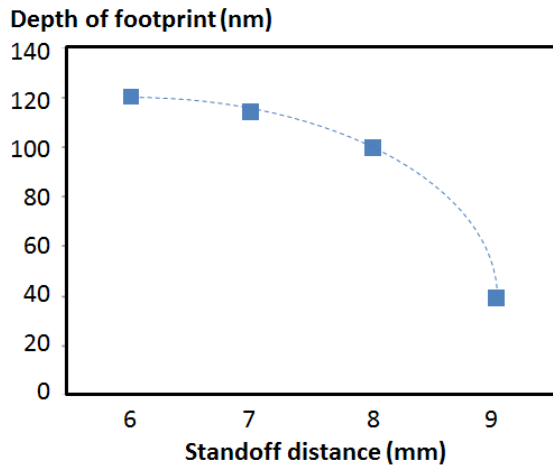


Figure 4-13 Depth of trench footprint versus standoff distance

4.3 Experimental setup for the power dissipation analysis

4.3.1 Measurement method and instrumentation for the power dissipation analysis

4.3.1.1 National Instruments DAQ

Data acquisition (DAQ) is a process to measure an electrical or physical phenomenon, e.g. voltage, current, pressure, temperature, etc. In this project, a DAQ measurement hardware provided by National Instruments (NI) is used to measure temperature. This DAQ (see Figure 4-14) works together with temperature sensors and a computer with programmable software (SignalExpress).

DAQ hardware is an interface between a computer and temperature sensors outside. It digitizes the input analog signals with a signal conditioning circuitry, and an analog-to-digital converter (ADC). Signal conditioning circuitry transfers a signal into a form, which can be input into the ADC. Then an ADC converts the analog signals into digital, and these signals are transferred to a digital equipment over a computer bus. In this project, NI 9270 C Series RTD analog input module features four universal channels and 24 bits of resolution for 100Ω RTD measurements.

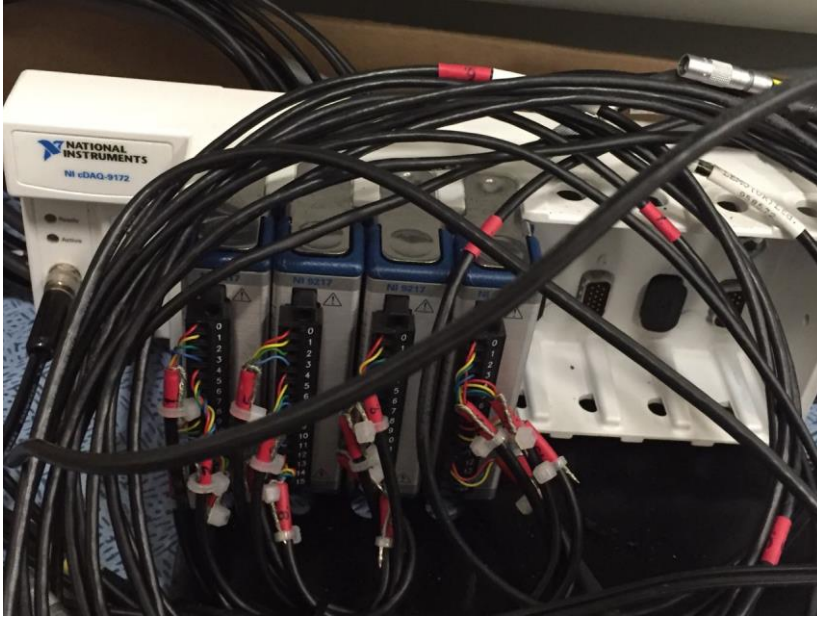


Figure 4-14 Photo of the NI DAQ used in the experiment

4.3.1.2 Resistance Temperature Detectors (RTD)

The RTD principle is based on the change of electrical resistance as a function of temperature. OMEGAFILM PT100 –platinum- RTDs were used for these experiments. These thin film RTDs are proven much higher transient stability (better than 1mK per year). The temperature range is from -70°C to 500°C with a sensitivity of $0.39\% \text{ K}^{-1}$. National Instrument Data acquisition (DAQ) device was used to process the measurement with NI Signal Express. All RTDs were calibrated in 0 and 100°C water. The nonlinearity correction parameter found was 0.385% per 100°C. The measurement uncertainty of these RTDs was down to 0.001 °C (0.1% at 0°C).

The RTDs were located at key points to measure the coolants' temperature of both inlet -supply total-, and outlet -return total, coil and nozzle- (Figure 4-15, left). Bespoke instrumentation was carried out using a straight fitting mounted on the end of the coil (Figure 4-15, right).

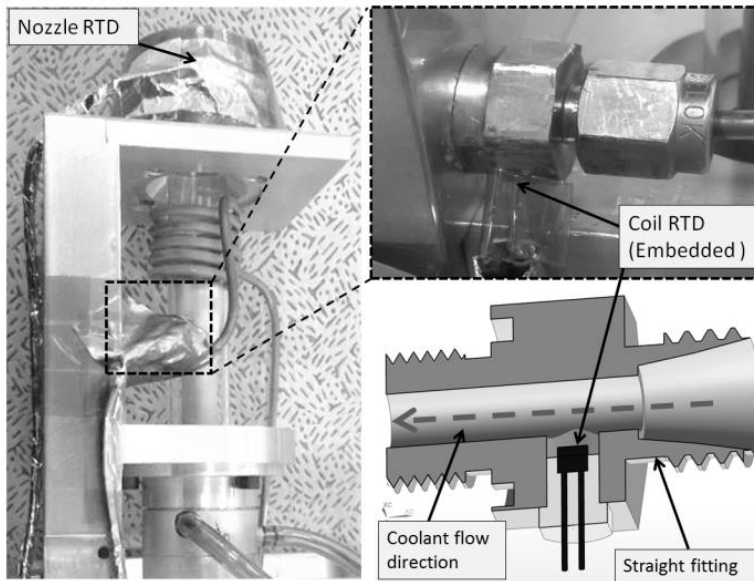


Figure 4-15 Instrumented plasma torch using RTD sensors

All the RTD sensor heads were wrapped with aluminium foil and aluminium tape, the standard wrapping method as shown in Figure 4-16 is used through the whole experiment in this project.

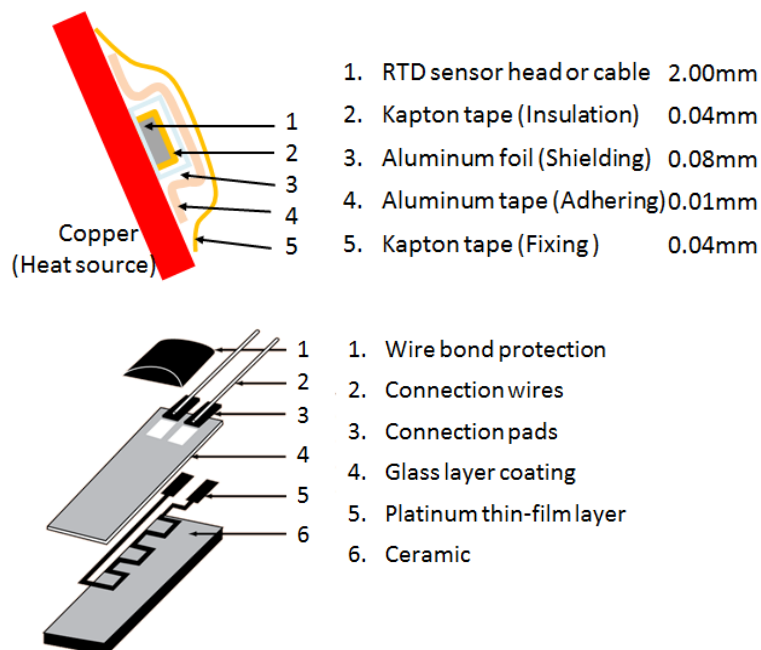


Figure 4-16 Cross section schematic for the wrapped RTD sensor (top) and OMEGAFLIM RTD sketch (bottom)

4.3.1.3 Thermocouples (TC)

TC is a voltage based temperature sensor. The measurement principle is based on Seebeck effect (1822) [138]. In this experiment, K type TC was chosen. Typical temperature range of this type of TC is from -270°C to 1370°C with a sensitivity of $\sim 40 \mu\text{V K}^{-1}$. A Pico TC-08 Data Logger was used for logging the temperature measurements. The measurement uncertainty of these TC was down to 0.1°C . The same standard wrapping method as RTD is also used to wrap TC sensors.

4.3.1.4 Infrared thermometry

Infrared (IR) thermometry is a noncontact temperature measurement device that offers 3 major advantages – fast (in the ms range), high temperature (over 1300°C) and no interference (electric conductive). In this project, two kinds of IR thermometry are used to measure the temperature of copper nozzles. They are IMPAC Pyrometers and ThermoIMAGER camera.

An IMPAC Pyrometer IN 510 (Figure 4-17, top) powered by 24 V DC is adopted. This pyrometer is equipped with sensor head and sensor cable (shielded) for a maximum temperature of 85°C . The optical sensor head provides a field of view 10:1, as illustrated in Figure 4-17 (bottom).

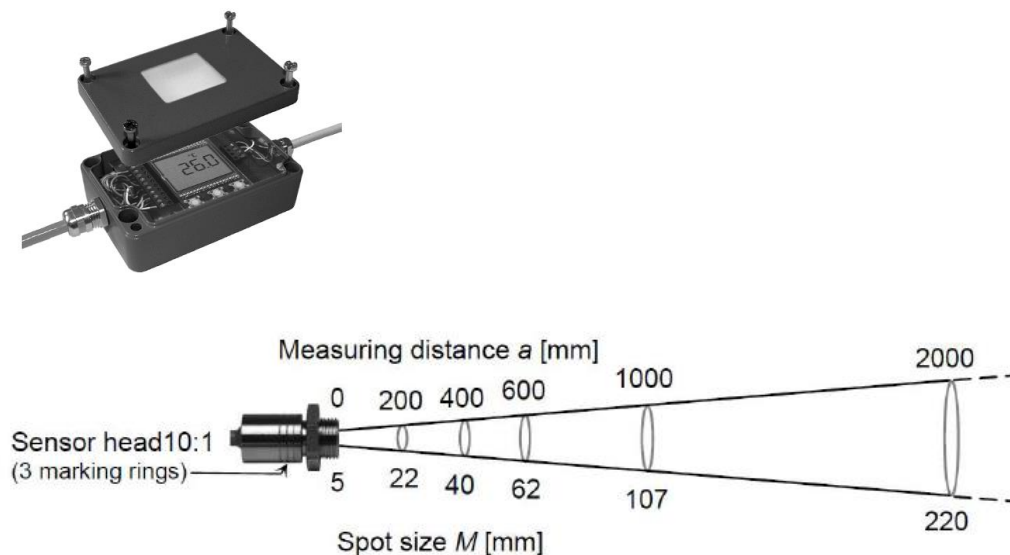


Figure 4-17 Photo of the IMPAC Pyrometer IN 510 (top) and the optical sensor head (bottom)

ThermolMAGER TIM 450 (Figure 4-18) from Micro-Epsilon is used to provide a coarse measurement of the copper nozzle. The camera has a high resolution of 382x299 pixels and high thermal sensitivity with 40mK. It is equipped with 13° lens, and has a measuring range of -20°C to 900°C.

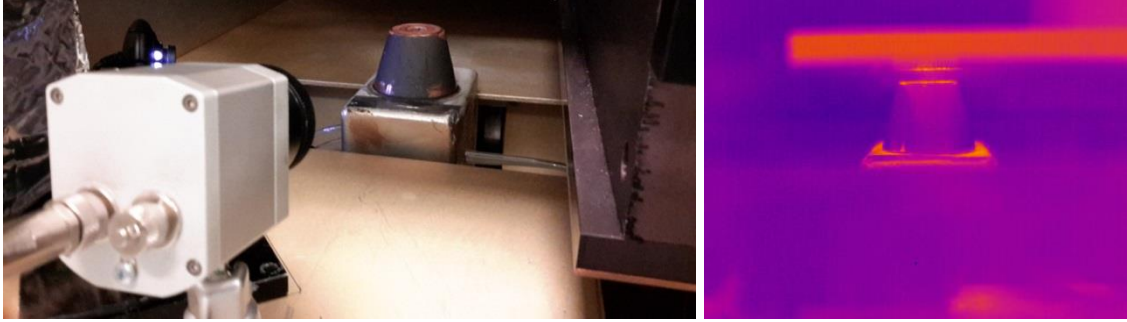


Figure 4-18 Setup of the measurement using ThermolMAGER TIM 450 (left) and a field of view from ThermolMAGER (right)

4.3.1.5 Flow meter

A Platon NGX series glass variable area flowmeter (**Figure 4-19**, left) was used for measuring the flow rate of coolants. The fluid lifts the float to an equilibrium position in a standard scaled glass tube. This tapered tube is chosen as A6 size ($50 - 800 \text{ cm}^3 \text{ m}^{-1}$) in accordance with the limitation of the flow switch. The accuracy of this flow meter is $\pm 1.25\%$ FSD ($\pm 0.625 \text{ cm}^3 \text{ m}^{-1}$). This tube is defined by standard scale for pure water at 20°C, but can be custom scaled for required fluids with a maximum viscosity of 12 cP.

The viscosity of mixed coolant is estimated following Gambill (1959) by

$$\mu_{coolant}^{1/3} = x_a \mu_a^{1/3} + x_b \mu_b^{1/3} \quad (4-12)$$

where x_a is the mass fraction of water (= 50%);

x_b is the mass fraction of ethylene glycol (= 50%);

μ_a is the viscosity of water at 20°C (=1.00 cP (mPa·s));

μ_b is the viscosity of ethylene glycol at 25°C (=16.10 cP (mPa·s)).

So $\mu_{coolant} = 5.475 \text{ cP}$.

The viscosity value of this coolant was below 12cP, the flow tube FSD was estimated using the graph below (**Figure 4-19**, right), according to the density of

the coolant. The density of the coolant at 20°C is 1055.7035 kg m⁻³ (1.0576 SG). So the actual flow rate was the value read from the flowmeter kit multiplying by 0.95.

Figure 4-19 (left) illustrates the flowmeter used in this experiment. This measurement was carried out when Helios 1200 was switched off for safety reason. However, that experimental condition has not affected the measurements.

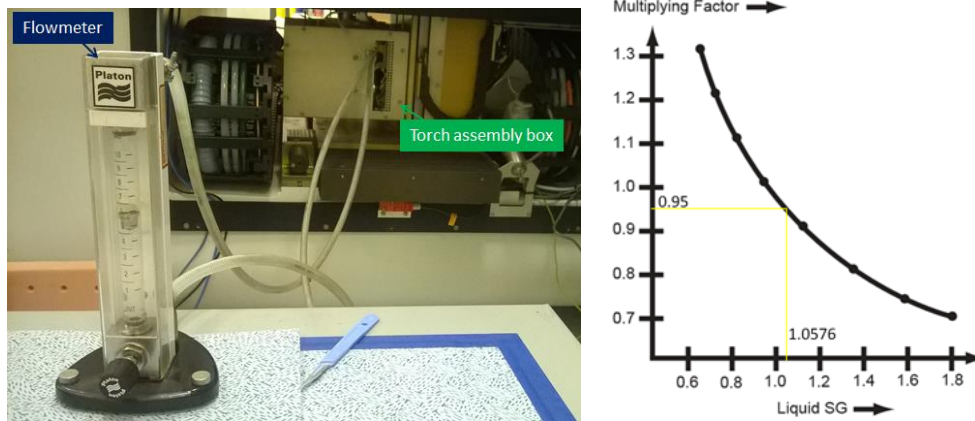


Figure 4-19 Photo of the flowmeter used in the experiment (left) and multiplying factor graph (right)

4.3.2 Experimental method for the power dissipation analysis

4.3.2.1 Power balance

It is aimed to estimate the power dissipated within the plasma torch. This aim was achieved by analysing the power absorbed by coolant running through both torch coil and De-Laval nozzle. Indeed, the RF power was provided to the torch coil to create and maintain the plasma jet. The RF power is consumed by coolant, argon gas, and radiation. The global rate of energy balance is:

$$\Delta P_{RF} = \Delta P_{coolant} + \Delta P_{argon} + \Delta P_{radiation} \quad (4-13)$$

where $\Delta P_{coolant}$ is the power dissipated by the coolants;

ΔP_{argon} is both the power dissipated by the energy beam and absorbed by the ionisation mechanism;

$\Delta P_{radiation}$ is the power dissipated by the core of the plasma but not

counted in the coolant.

This power balance was investigated through both experimental work and analytical calculations. The experimental results presented in the 5.3.1 focus on the temperature change of the coolant channels –coil and nozzle-. The terminology used in the results section is Temperature Difference (TD).

4.3.2.2 Temperature measurement of coolant

Coolant is used to protect the coil and nozzle from melting when the plasma is ignited. The recommended temperature of the coolant is about 20 °C. Coolant flows into two main torch components: coil -excitation region- and nozzle -transportation region-. The torch assembly picture is shown in Figure 4-20. Two tributaries go through the copper nozzle, the aluminium flange and aluminium torch support, and the copper coil. PTFE hoses are adopted for delivering the coolant to the torch assembly.

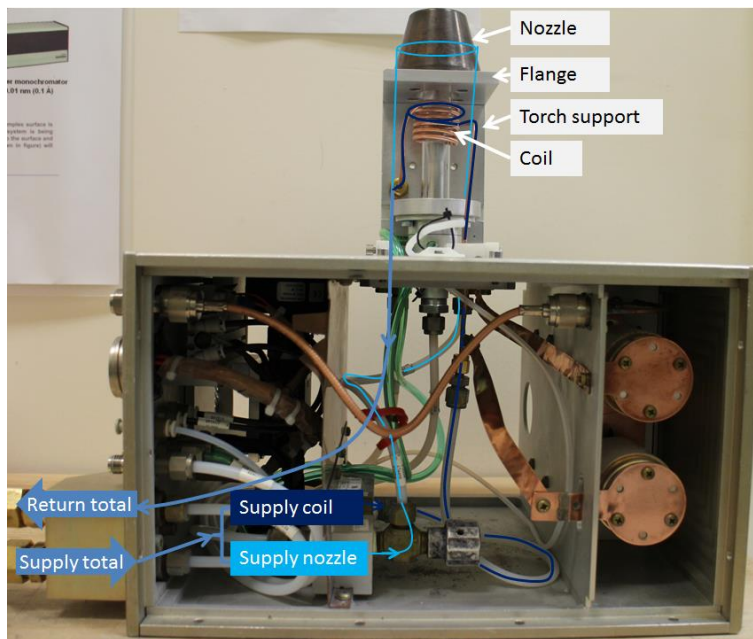


Figure 4-20 Temperature controlled plasma torch and mix match RF network

Figure 4-21 illustrates the schematic of the coolant distribution and the instrumentation of the torch. Positions of flow metres and temperature sensors are provided. Chiller, RF generator, coil, nozzle and gas supply are mentioned.

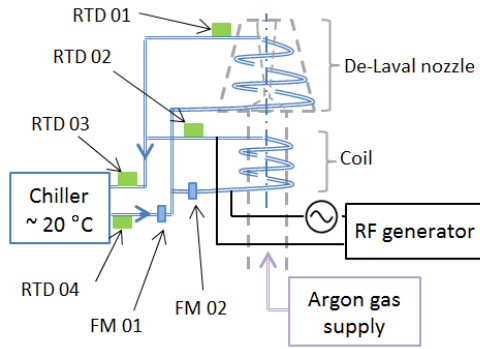


Figure 4-21 Schematic the plasma delivery system: RF generator, gas supply, chiller, RTDs, flow meter (FM), torch and coolant channels are shown

Coolant was provided to the plasma torch using a 19.4 KW cooling capacitance chiller (TAEvo Tech 051). The distance between the chiller and the machine was 10 m. The total amount the coolant (tank and pipe) was 115 L. Figure 4-22 shows the thermal cycle logged during two hours duration. The amplitude of the variation is 3.5 °C and the period of the chiller cycle is 30 minutes.

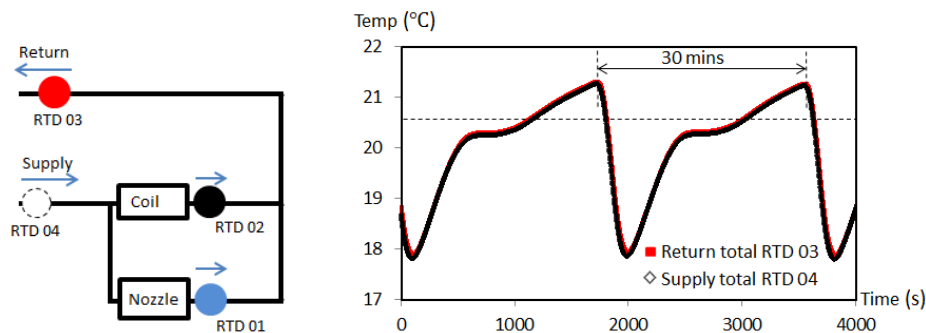


Figure 4-22 Coolant temperature variation for a two-hour period

4.3.2.3 Influence of the sensors onto the PDS

The PDS was strongly affected by the instrumentation (sensors, electrical leads, and connectors). Torch behaviour changes could be observed whenever these sensors were idle or used for logging temperature values. Although the frequencies recorded at different Forward Powers (FP) were barely changed (0.1 MHz), Reflective Powers (RP) increase was observed. The RP value has increased from 0 up to 10 W when RF power was set to 600 W. And the RP was increased from 0 up to 20 W when RF power was set to 700 W. Also, the plasma became systematically unstable when the RF power was set to 800 W

leading to RP rush up to 200 W. Before this instrumentation, the RP used to be less than 10 W for RF power set to 800 W. Consequently, the temperature measurements presented in this experimental work were carried out by setting the RF power below 700 W.

4.3.2.4 Assessment of sensors’ measuring capability

Two sensors -one TC and one RTD- were used to measure “Supply total” coolant temperature. Results are plotted in Figure 4-23. Purple and black plots are TC and RTD responses respectively. RF power was incrementally increased during the 7 minutes this test lasted. It can be seen that TC response was influenced by the RF signal. Red circles are used to point out the time where RF signal was switched on, plasma was ignited, and RF power was increased (recorded in Table 4-1). This signal break is due to the RF frequency re-tuning.

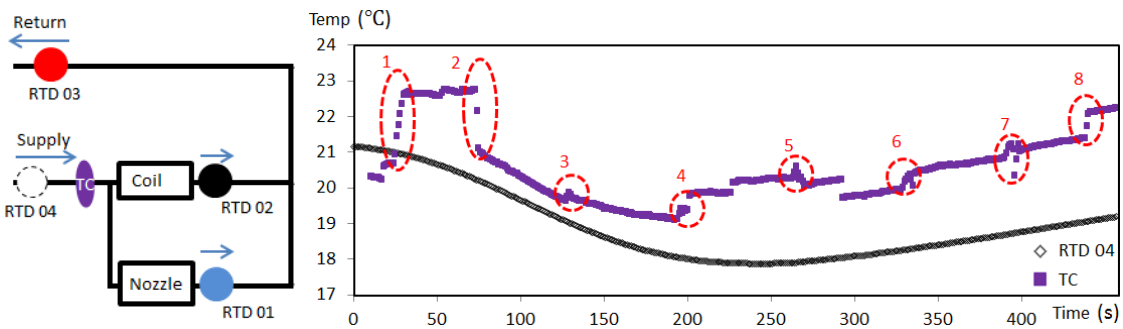


Figure 4-23 Supply total temperature measurement logs of the coolants using both RTD and TC

Table 4-1 Parameters recorded during the operation of plasma delivery system

Numbers shown in Figure 4-23	1	2	3 - 7	8
Action description	Switch on	Plasma ignited	Increase RF power	Switch off
RF power (W)	50-200	230	300 - 700	Back to 0
Frequency (MHz)	41.057	40.845	40.820 - 40.698	-

The Same phenomenon was logged by the TC attached to the surface of the nozzle (Figure 4-24, yellow plot). Poor TC responses are attributed to the lack of high quality EM shielded.

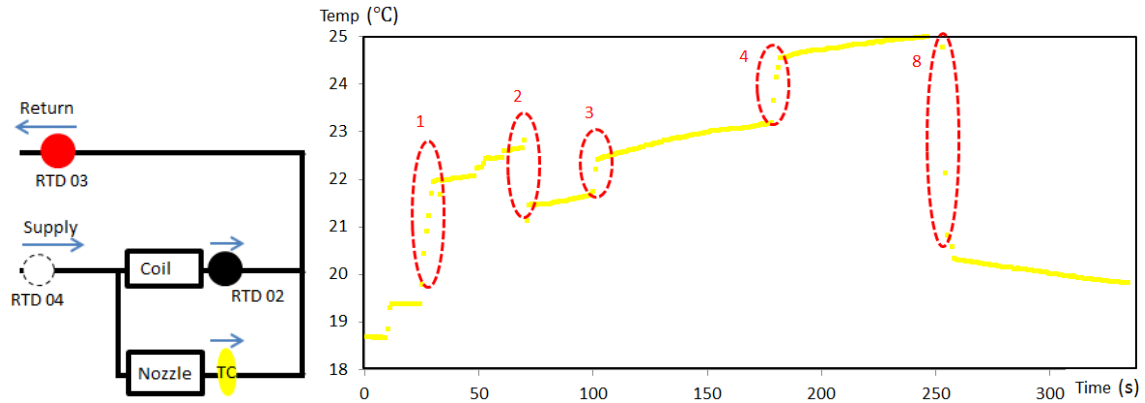


Figure 4-24 Temperature measurement log of the nozzle using TC

4.3.2.5 Thermal response of the coolant through regular operation

Better quality temperature measurements were carried out using RTDs. Logs are displayed in Figure 4-25. This measurement method and instrumentation configuration was assessed robust enough to be used for energy dissipation investigations and calculations.

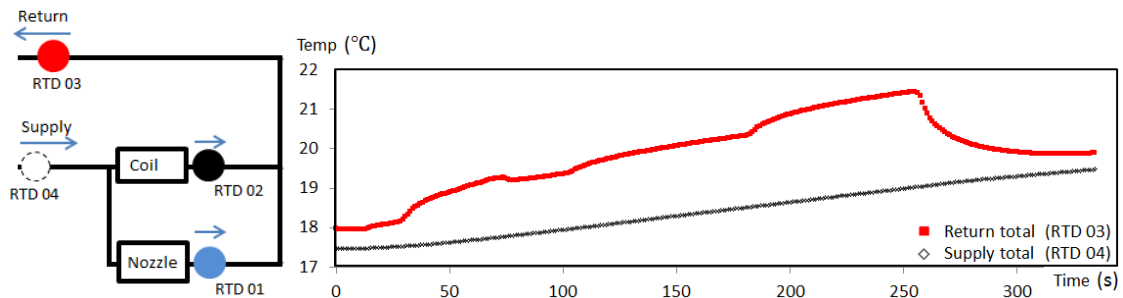


Figure 4-25 Temperature measurement logs of the coolants using RTD

5 Results

5.1 Result of RF network investigation

This work aimed at investigating the RF network of the Plasma Delivery System (PDS). The result of this investigation enabled to determine the most influencing parameters and to recommend a method for tuning the PDS.

The PDS parameters are load capacitance, tune capacitance, and the induction coil (geometry, oxidation, and pitch distance). Due to parameter effects and interactions, a one-factor-at-a-time (OFAT) method was chosen for this investigation.

5.1.1 Effects of capacitors in the RF network

5.1.1.1 Effects of Tune capacitance changes

The tune capacitor value was varied from ~197.96 pF -14.14 turns- to ~199.5 pF -14.25 turns- (increase 0.77%), when the load capacitor was set to ~27.86 pF -1.99 turns-. For each value, the plasma was ignited using a minimum amount of power ~250 W and the RF power was increased up to 800 W. Frequencies were recorded at both 200 W (before ignition) and 800 W. Figure 5-1 displays the logged data. Experiments were carried out within three days, and the frequencies appeared to be repeatable (Max deviation better than 0.1MHz). The logged frequency increased as the tune capacitance value was increased. Also, a pseudo linear correlation was highlighted.

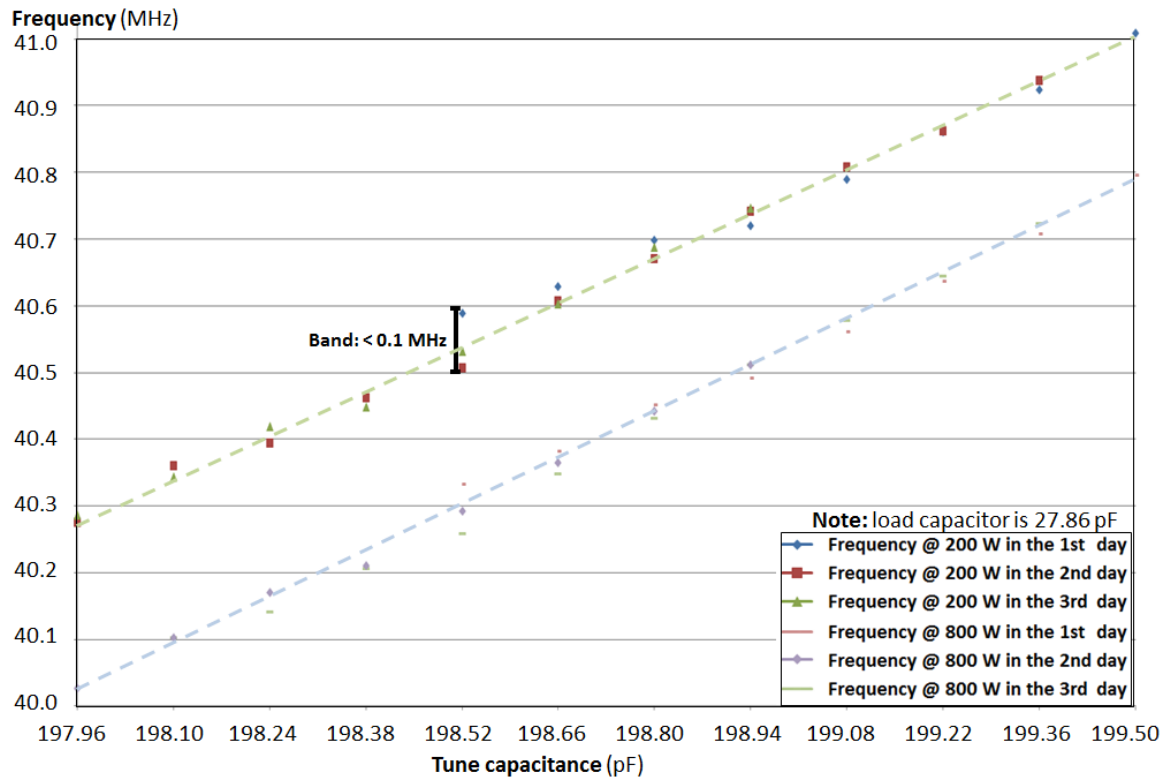


Figure 5-1 Frequency versus tune capacitance

5.1.1.2 Effects of Load capacitance changes

The load capacitor was changed from 27.86 pF (1.99 turns) to 28.42 pF (2.03 turns) (increase 2%) while the tune capacitance value was set to 198.94 pF (14.21 turns). The tune capacitance value was chosen because the observed ignition power value was low and consistent. The frequency values are plotted in Figure 5-2. Then it can be seen that the optimum frequency determined by the RF generator did not change much. This observation contrasted with results shown in the previous section -tune capacitance response (Figure 5-2).

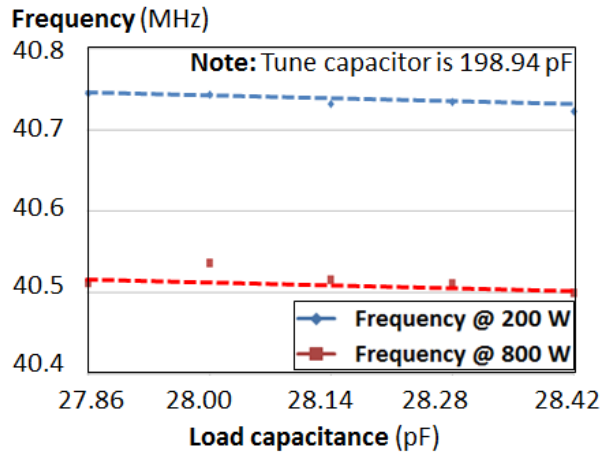


Figure 5-2 Frequency versus load capacitance

The investigation (see Figure 5-3) highlighted that the tune capacitance value change had stronger effect than load capacitor value. Indeed, the frequency changed by 0.05% when the load capacitance value was increased by 2 %. While frequency changed by 2% when the tune capacitance value was increased by 0.77%.

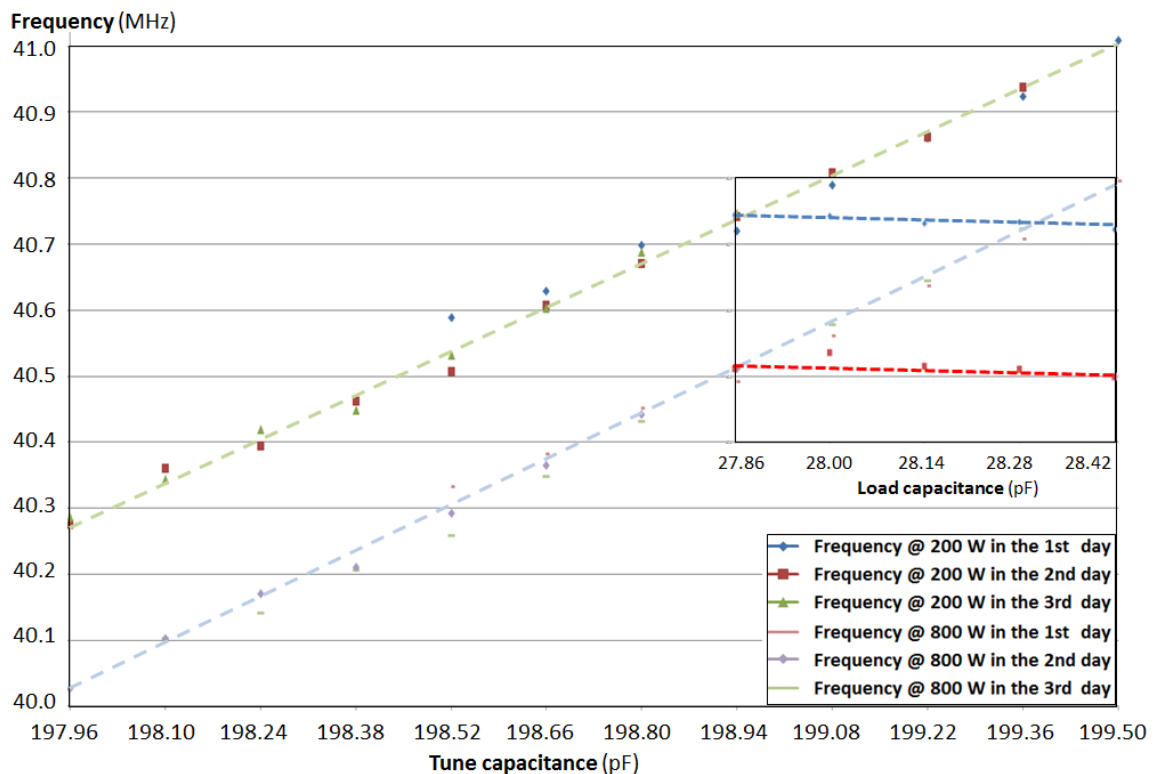


Figure 5-3 Comparison of influence on frequencies between tune capacitor and load capacitor

5.1.1.3 Effects of capacitance setting on the torch ignition

This section enables to compare the effects of tune and load capacitance values on the torch ignition. Three experiments were carried out systematically for each capacitance settings. The minimal amount of power required to strike the plasma was recorded. The line graphs displayed below show mean, min, and max logged values.

The tune capacitance value was changed from 197.96pF (14.14 turns) to 199.5 pF (14.25 turns). The ignition powers are displayed Figure 5-4. Weighted average ignition power values were calculated and displayed (see purple curve). The minimal -averaged- ignition power was determined to 300 W. Optimum tune capacitance value was 198.94 pF. Also ignition power values were more consistent (standard deviation: 6.63 pF) compared to other results.

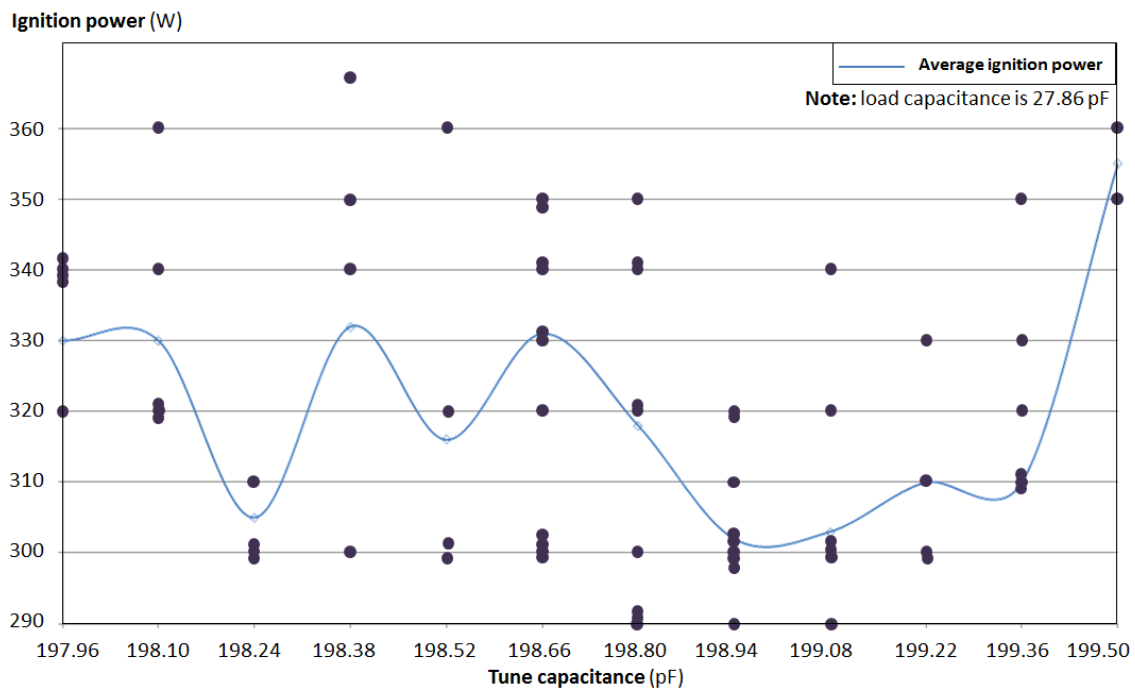


Figure 5-4 Ignition powers recorded at different tune capacitances

After setting the tune capacitor to its optimum value i.e. 198.94 pF, the Load capacitor was changed from 27.86 pF (1.99 turns) up to 28.42 pF (2.03 turns). The ignition power values are plotted in Figure 5-5. The lowest averaged ignition power value was achieved when the load capacitance value was set to

28.00 pF (2.00 turns). Also it was observed that the standard deviation value (5.75 W) was improved.

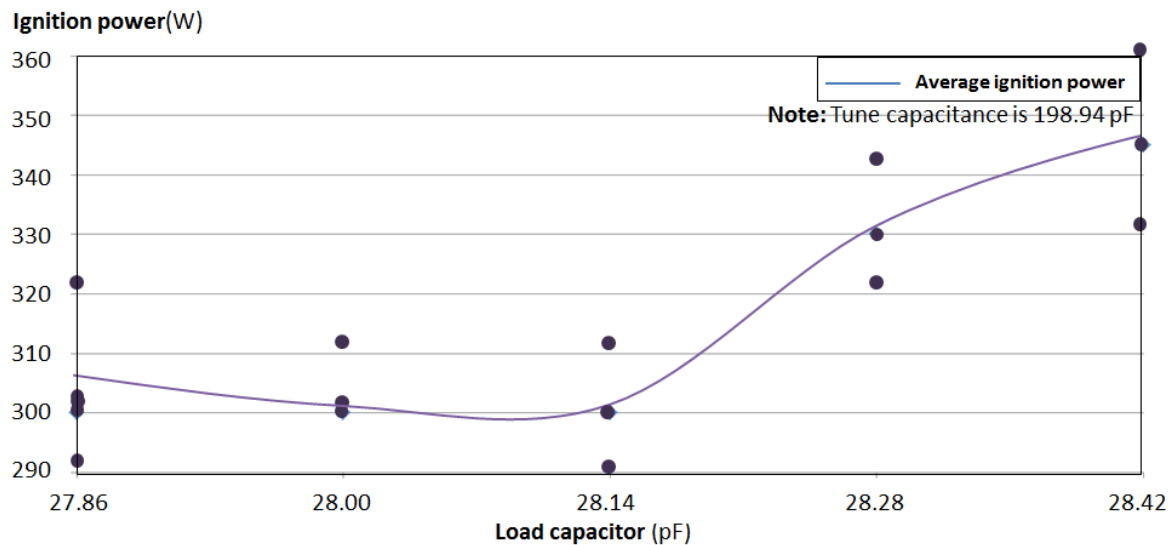


Figure 5-5 Load capacitance versus ignition power

5.1.2 Effects of torch coil in the RF network

5.1.2.1 Effects of the length of coil

The length of the copper torch coil (shown in Figure 5-6, left) can be changed by squeezing or stretching the induction coil (refrigerated grade copper pipe). Figure 5-6 (right) illustrates how the length of the coil was changed and measured using slip gauges.

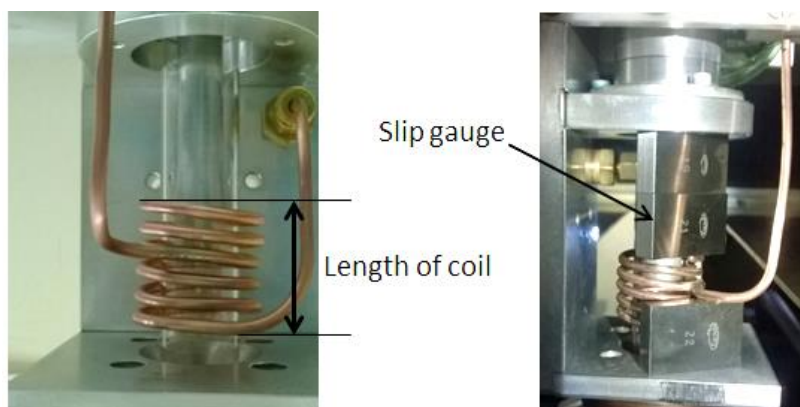


Figure 5-6 Photo showing the length of coil (left) and its measurement method (right)

The length of the coil was changed from 23.5 mm up to 25.5 mm. It was noticed that ignition took place easily for coil length set to 23.5 mm. However, it was noticed that no ignition could take place for the coil length set shorter than 23.5 mm. As shown in Figure 5-7, the frequency value increases as the length of the coil was stretched. Also the ignition power value needed to be increased. The length was changed up to 8.5 %, and the response of frequency was increased 1.24%. The reflective power values were less than 10 W.

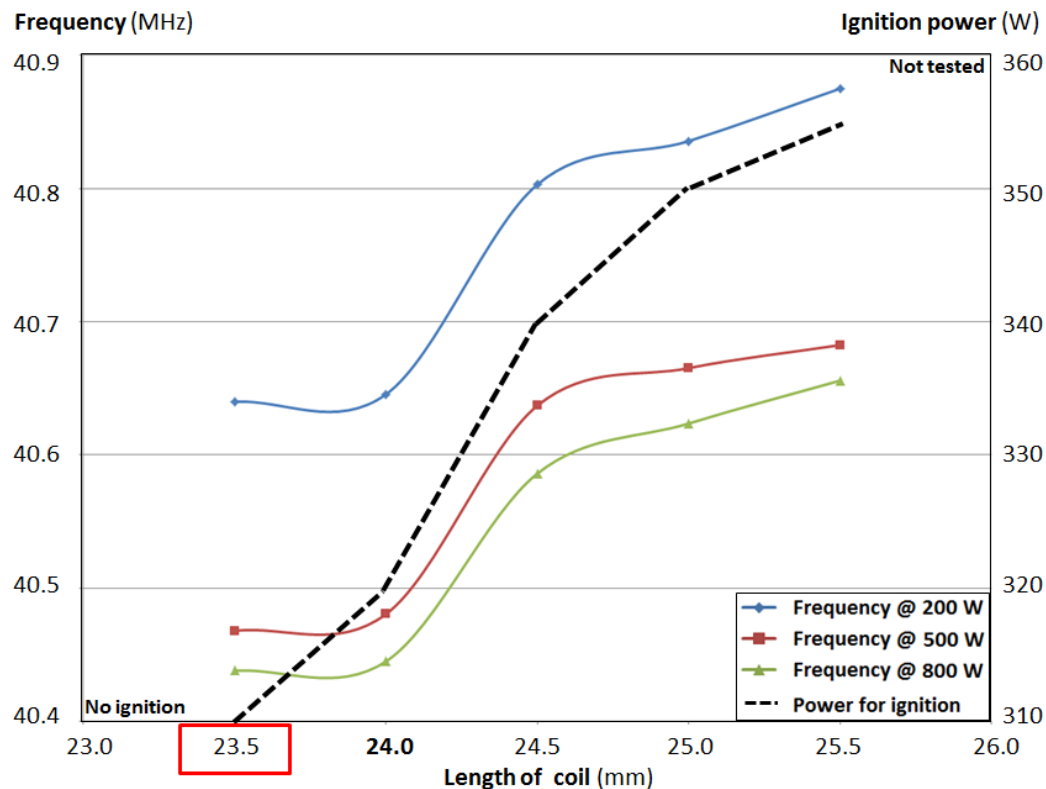


Figure 5-7 Frequency and ignition power versus the length of coil

5.1.2.2 Effects of number of free turns on the coil

The effect of coil geometry was investigated. The original torch was equipped with two different coils. The first tested coil was made of two sections: a three-turn powered coil and a two- turn free coil. The second tested coil had three-turn powered coil, and two-and-a-quarter-turn free coil (Figure 5-8). The values of the load and tune capacitance were 28.0 pF and 199.8 pF.

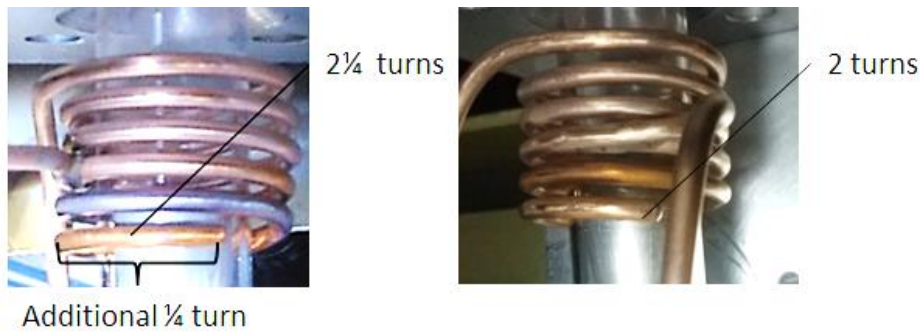


Figure 5-8 Three-turn powered coil, and two-and-a-quarter-turn free coil (left) and three-turn powered coil, and two- turn free coil (right)

For RF power in the range 500 W up to 800 W, results highlighted that frequencies shifted downward by about 50 KHz (Figure 5-9).

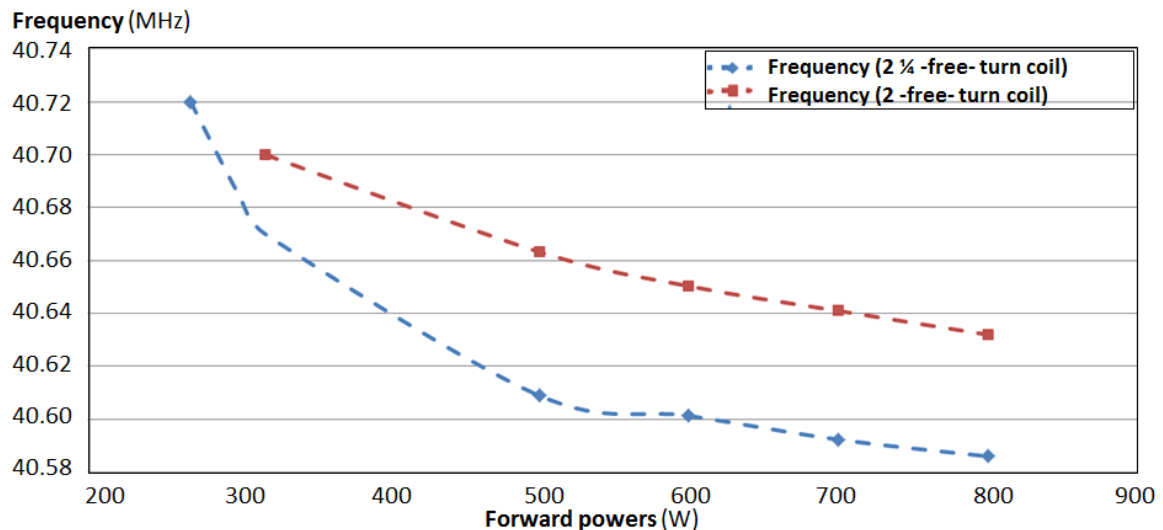


Figure 5-9 Frequency for 2¹/₄-free-turn coil and 2-free-turn coil

The change of reflected power (RP) values was significant (Figure 5-10). The RP value was better than 10 W when using 2-free-turn coil, but these values increased beyond 24 W (3% of RF power).

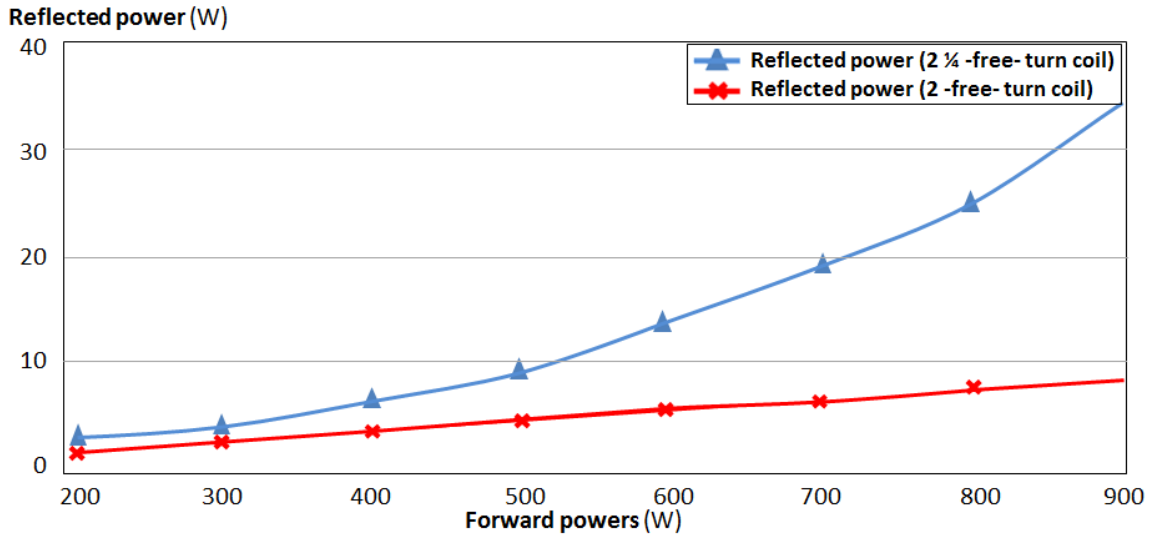


Figure 5-10 Forwarded power versus reflective power for 2¼-free-turn coil and 2-free-turn coil

5.1.2.3 Effects of corrosion on the coil

At atmospheric pressure, the coil is strongly subject to oxidation. Thus corrosion takes place. The effect of surface oxidation leads efficiency drop. Indeed, the EM field intensity is weaker. Consequently, the RF signal is poorly transferred to the plasma. Oxidised copper coil occurred undue stress on the rest of the electrical components. Oxidised coil contribute to premature failure of the PDS.

The efficiency of different materials in conducting RF energy plays an important role in the overall plasma efficiency. Metal oxides do not conduct RF signals as well as pure metal. In particular, copper sulphate is a very poor conductor. Silver oxide has a much smaller effect on efficiency.

If heat is the biggest problem then the best way to deal with this is to use a coil that is plated with a highly conductive material such as silver. However, silver plating does produce a tarnished appearance after a period of use. To obtain the best life out of a coil in this situation, the coil should be cleaned frequently with a tarnish remover. This action does eventually lead to the removal of the silver plating. However, if the tarnish is not removed, excessive heat can build up due to higher absorption and lead to the plating flaking away from the copper tubing. This exposes bare copper areas that will deteriorate at a faster

rate. Copper will oxidise much quicker, thereby leading to possible arcing between coils and lower energy transfer to the plasma [139].

5.1.3 Summary

The four variables of the L type RF network were investigated. Recommended values are given in Table 5-1 based on the low ignition power, test repeatability and low reflected power.

Table 5-1 Optimum values for the RF network

Influencing factors	Recommended value
Tune capacitance	198.94 pF
Load capacitance	28.00 pF
Length of coil	23.5 mm
Number of free turns	2.0 turns

The research on the capacitors provides an optimum setting of both Tune and Load capacitors. The practical method to determine the optimal parameters is threefold: start adjustment procedure using 200 W and make sure that reflective power is less than 10 W, increase the forwarded power incrementally, and force the RF generator to retune after each 100 W increases. When correctly tuned the amount of power required for plasma ignition should be consistent and less than 350 W. Also, the reflected power values observed should be less than 10 W for all forwarded power values.

The research on the coils highlights the effect of the length of the coil on both frequency and ignition power. The sensitivity of coil's length is 0.065, which is more than twice of load capacitance (0.025) but still much lower than tune capacitance (2.5). The optimum setting of the coil's length is 23.5 mm. The most important result of the investigation of the coil highlights the effect of the number of free turns on both frequency and ignition power. Although the sensitivity to the frequency is as small as the load capacitor (0.0255), the effect

on the RP is tremendous. For the priority of PDS operation, the free turns' number of the coil will be kept at 2.

5.2 Result - numerical analysis of De-Laval nozzle designs

The CFD model of High Temperature Jet (HTJ) has been initially validated with the benchmark model in 4.2.1.4. In this section, the model is validated from the viewpoint of processing in 5.2.1. Further validation of the model based on key parameter design is performed in 5.2.2. Finally, the emphasis is made in 5.2.3 on the comparison of the aerodynamic properties between the original and one of the enhanced nozzles.

5.2.1 Aerodynamic behaviour of the De-Laval nozzle

This section presents two investigations for a HTJ (5000 Kelvin) that is used in the context of the Plasma Figuring process. Firstly, an investigation focuses on the aerodynamic properties of this jet that streamed through the plasma torch De-Laval nozzle and impinged on optical surfaces. Secondly, the work highlights quantitatively the effects of changing the distance between the processed surface and nozzle outlet. In both investigations, results of numerical models and experiments were correlated. The areas of interests in the model domain are the nozzle convergent-divergent region and the impinged substrate regions. Strong correlations are highlighted between the gas flow velocity near the surface and material removal footprint profiles.

5.2.1.1 Calculated results of the HTJ in the De-Laval nozzle

The calculated distributions for Mach number, the temperature in the domain are illustrated in Figure 5-11. The Mach number reaches the value of 0.56 in the bottle neck of the nozzle. This velocity is still subsonic as expected.

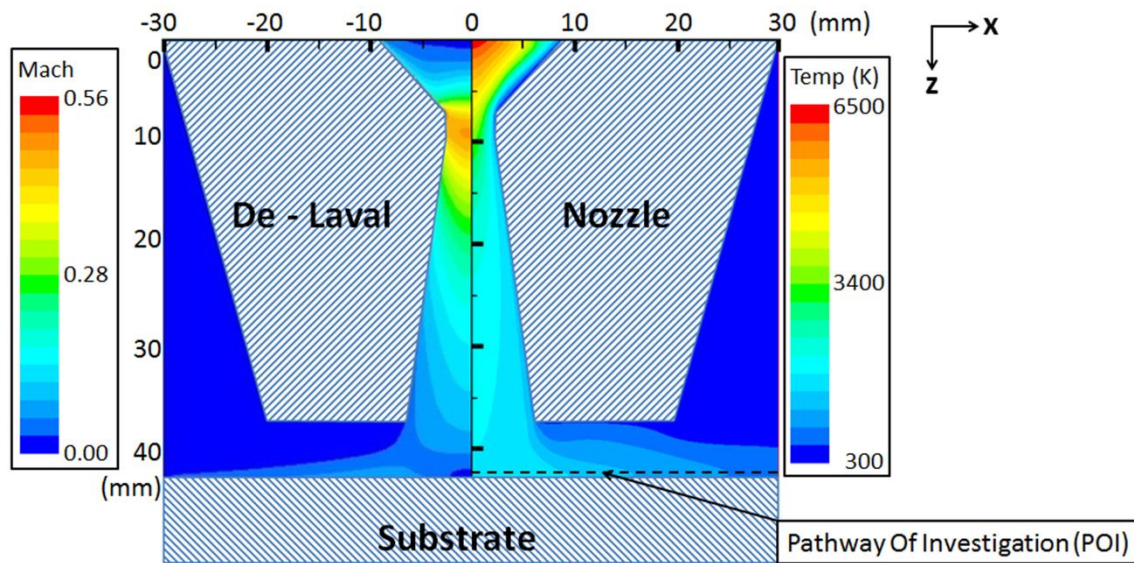
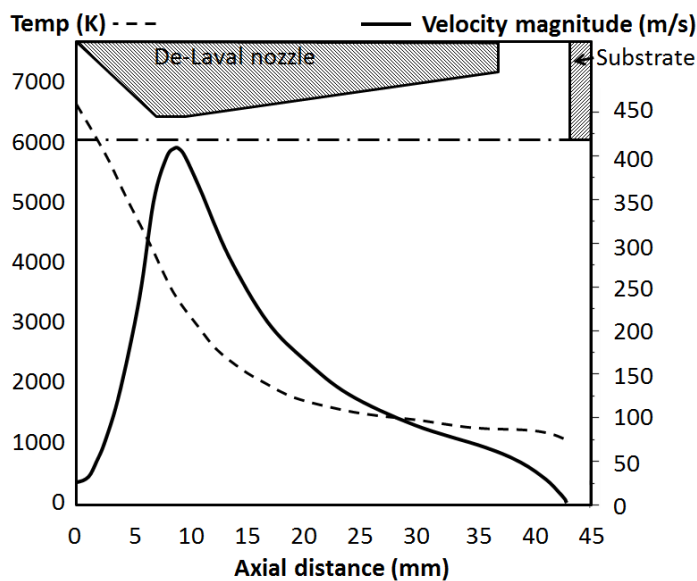


Figure 5-11 Calculated distribution of the Mach number (left), the temperature of HTJ (right) (x-axis is radial distance from the symmetric line, and z-axis is axial distance along the symmetric line)

From the results plotted above it is clear that the symmetric axis of the nozzle is a critical path that is further scrutinized. The variation of temperatures and velocities along the axis are displayed in Figure 5-12 (top). The static pressure is displayed in Figure 5-12 (bottom). The pressure in the nozzle drops significantly by axial distance 5mm. This low pressure is formed in the bottle neck, where the flow velocity reaches 440 m s^{-1} . And as expected the pressure value recovers in the divergent area of the nozzle.



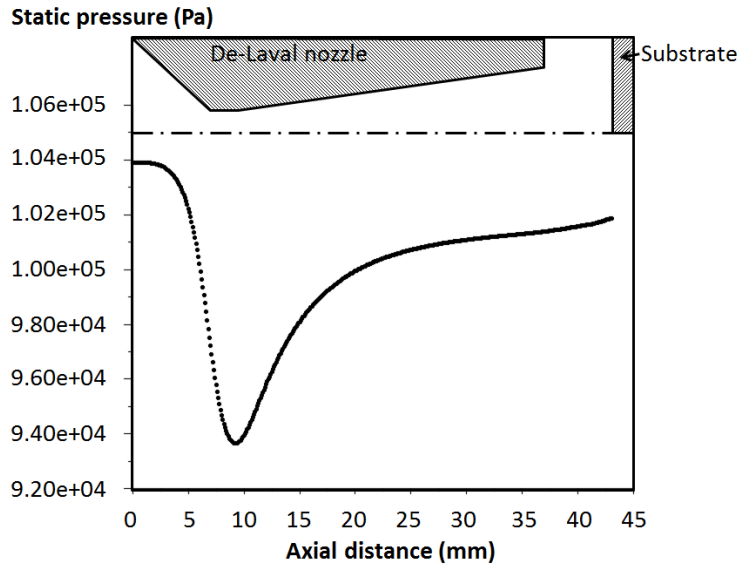


Figure 5-12 Axial profiles of temperature, blue dotted line and velocity, black solid line (top), Static pressure along the symmetric axis of the De-Laval nozzle (bottom)

The other area of interest is the near surface substrate region where the chemical reaction takes place. In order to ease the investigation, a line of study is defined at 10 μm from the substrate surface (Figure 5-11, horizontal dash line located above the substrate area). This line is called “Pathway Of Investigation” (POI). Along the POI, the chemical reaction related data – temperature, density, axial and radial velocity - are extracted and displayed in Figure 5-13. In the region close to the symmetric axis, both variables are higher than that of the ambience. Then it can be deduced that the chemical reaction in the centrally exposed region takes place more effectively. Also in the region far from the symmetric axis - radial distance: 15mm to 30mm - fewer silicon atoms are etched. This statement is supported by the evidence - footprint profile - shown in Figure 4-12.

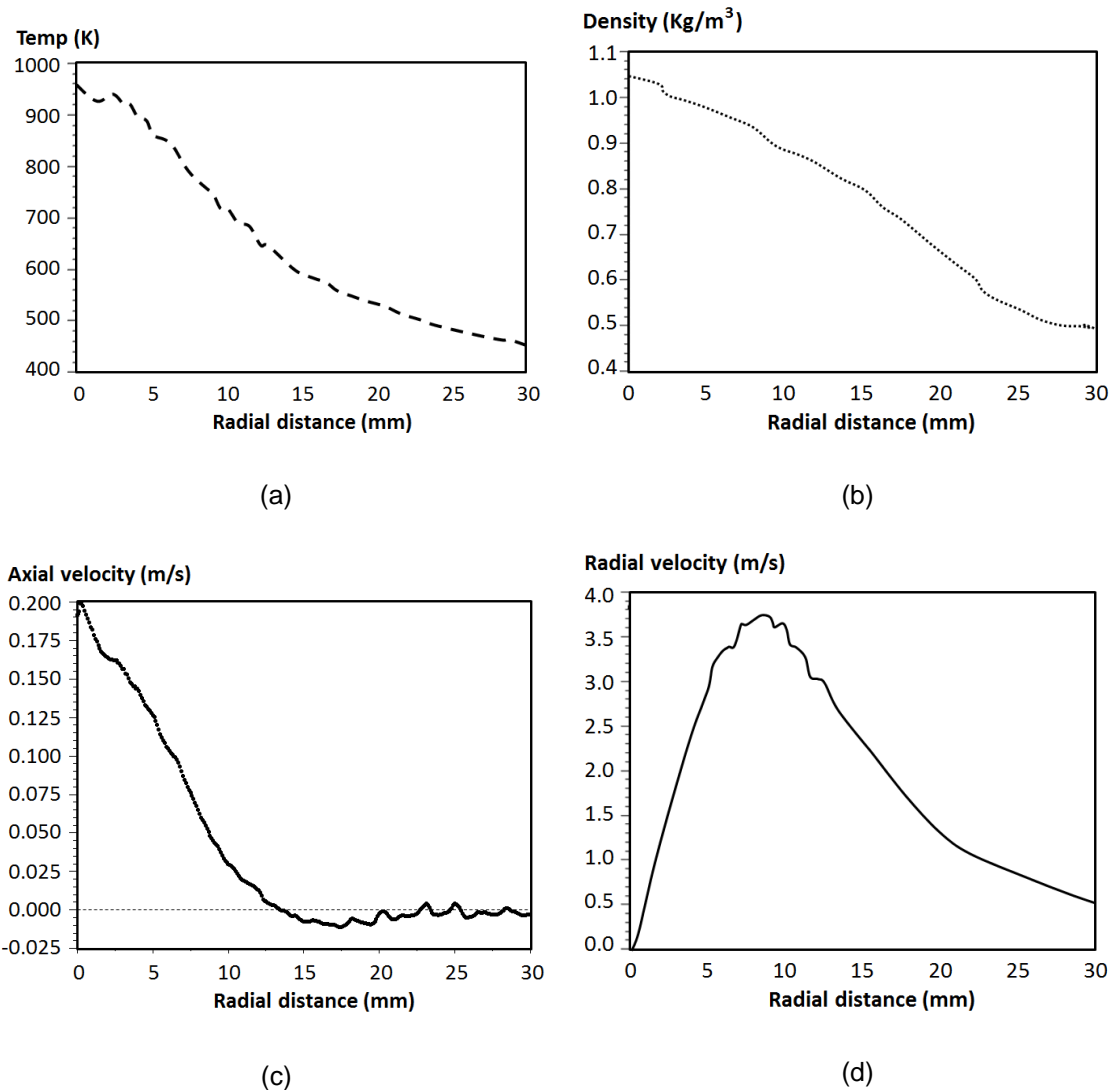


Figure 5-13 Radial profiles of (a) temperature, (b) density, (c) axial velocity, and (d) radial velocity along the "POI"

5.2.1.2 Exposed area definition

From a processing viewpoint, the plasma etching rate is influenced by parameters such as standoff distance of the torch nozzle, the travel speed of the torch - exposure time -, the power delivered by the RF generator, and reactive gas concentration. When those aforementioned parameters are coupled together then a specific near Gaussian shape footprint is created. However, from the microscopic view point, the plasma etching is considered to take place only in the region exposed to fluorine ions.

In Figure 5-14 (left, black solid line), HTJ axial velocity along the POI is displayed. As shown, the HTJ flow can go either downwards or upwards. The area that experiences downwards HTJ flow is shown with positive values of velocity. On the other hand, regions along the POI that experiences an upwards HTJ flow component are shown having negative values of velocity (see Figure 5-14, right). The area experiencing downwards flow is named “Exposed area”. In the next section, the Exposed area is characterised by its diameter value. That enables to compare the two profiles of interest: axial velocity and removal footprint.

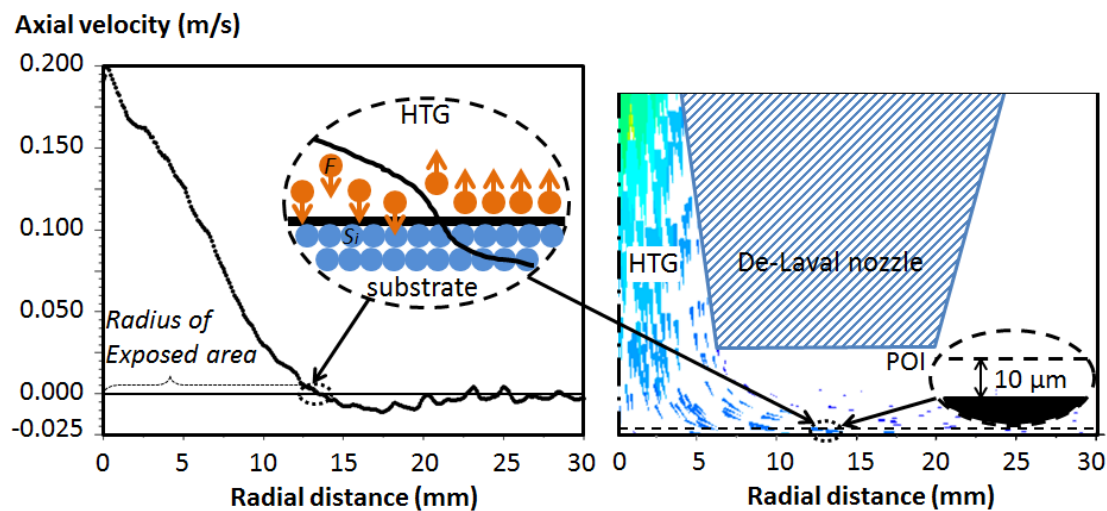


Figure 5-14 Radial profile of the axial velocity along POI (left) and sketch of the HTJ that flows onto the “Exposed area” (right)

5.2.1.3 Validation of the CFD simulation with experimental results

Figure 5-15 shows both the CFD simulation data (5.2.1.2) and experimental data -footprint cross section- (4.2.2.2). This plot highlights the comparison between the material removal footprint and the regions along the POI that experiences a downwards vertical flow. The Exposed area diameter is 26.8mm, which is close to the 6 Sigma value of the footprint’s aperture 31.1 mm. On the other hand, the two profiles are very similar.

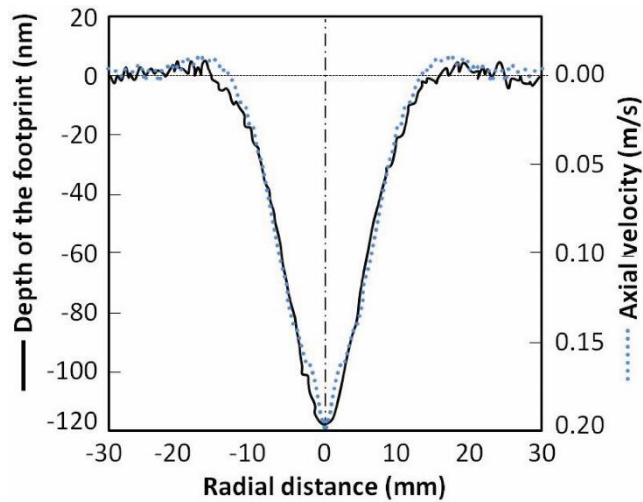


Figure 5-15 Curves of the footprint (black solid line) and axial velocity of HTJ along the POI (blue dotted line)

In addition to previous results, the correlation between exposed area diameter and 6 Sigma values is displayed in Figure 5-16 for standoff distances set to 6mm, 7mm, 8mm and 9mm. Good correlation takes place when the standoff distance is smaller than 7mm, and the discrepancy increases as the standoff distance is over 8mm. The etching rate is dependent on reactive species flux, the velocity of flow and irradiation intensity. When the substrate is far from the nozzle, both reactive species concentration and irradiation intensity will be weaker.

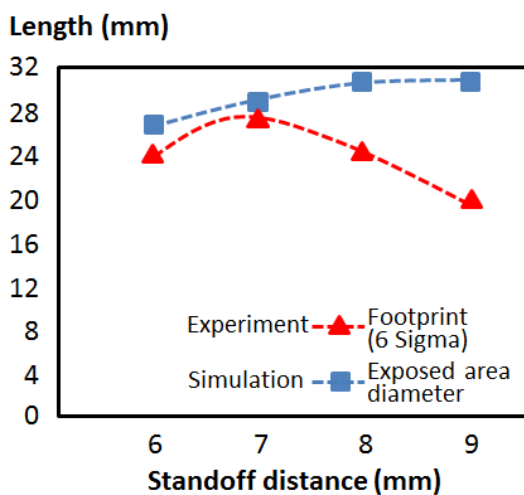


Figure 5-16 Correlation between footprint 6 sigma values and exposed area diameters

5.2.2 De-Laval nozzle evaluation using CFD model

Investigation of the nozzle's key design parameters based on the aforementioned 2D axis-symmetric numerical model has been made. Evaluation is based on the changing radius along the Pathway of Investigation that is exposed to free radicals. The hydrodynamic characteristics of the De-Laval nozzle depend on seven parameters (shown in Table 5-2). The distinguishing physical characteristic of this type of nozzle is the area ratio, meaning the ratio of the divergent area to the throat area. Also, from experimental view of point, D_1 will be kept the same, as it matches the size of existing torch tube design.

Three of them have been changed to investigate their effect on gas flow. The three design parameters varied were: the diameter of the throat D_2 , the diameter of divergent end D_3 , and the depth of the divergent path h_3 . The following paragraphs detail the findings and results obtained through the CFD model focussing on the radius exposed to free radicals and the maximum velocity in the throat.

Table 5-2 Parameters of the nozzle in the characteristic analysis

No	Parameters	Symbol	Schematic plot
1	Diameter of convergent end	D_1	
2	Diameter of throat	D_2	
3	Diameter of divergent end	D_3	
4	Depth of convergent path	h_1	
5	Depth of throat	h_2	
6	Depth of divergent path	h_3	
7	Stand-off distance	h_4	

5.2.2.1 Effect of the Throat Diameter

The throat -parameter D_2 - in the De-Laval nozzle is crucial, because the speed of flow increases strongly when the gas goes through this narrow section. A five-step increase of the throat diameter (4.0mm, 4.3mm, 4.7mm, 5.0mm and 5.3mm) is chosen for the investigation of the flow velocity change. The correlation between the diameter of the throat and the radius exposed to free radicals is highlighted in Figure 5-17. When D_2 decreases by 24%, the radius exposed to free radicals decreases by 19%. The sensitivity of D_2 is 0.79. Also, it can be observed that the flow velocity increases when the throat dimension gets smaller.

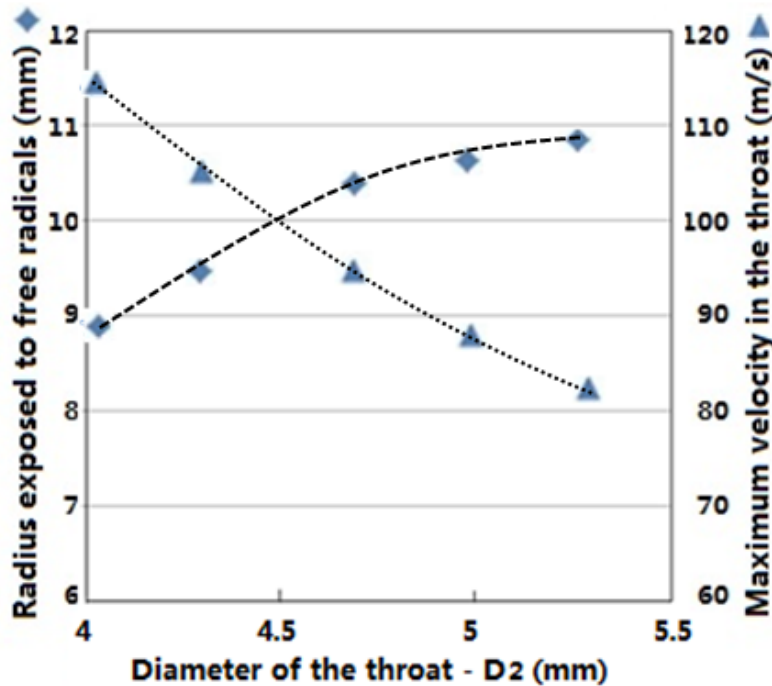


Figure 5-17 The throat diameter (D_2) versus the radius exposed to free radicals (◆ left), and D_2 versus the maximum velocity in the throat (▲ right)

5.2.2.2 Effect of the Divergent End Dimension

A similar comparison is made among nozzles with different dimensions of divergent end diameter -parameter D_3 -. The chosen diameters are 10.8mm, 11.4mm, 12.0mm, 12.6mm, 13.2mm and 16.7mm. The correlation between the diameter of the divergent end and the radius exposed to free radicals can be seen in Figure 5-18. As expected, the results show that a wider divergent end

generates a larger etched area. The dimension of the etched area decreases 8% as D_3 shrinks 18%. The sensitivity of D_3 is 0.44. The maximum flow velocity through the throat is little affected by this nozzle parameter.

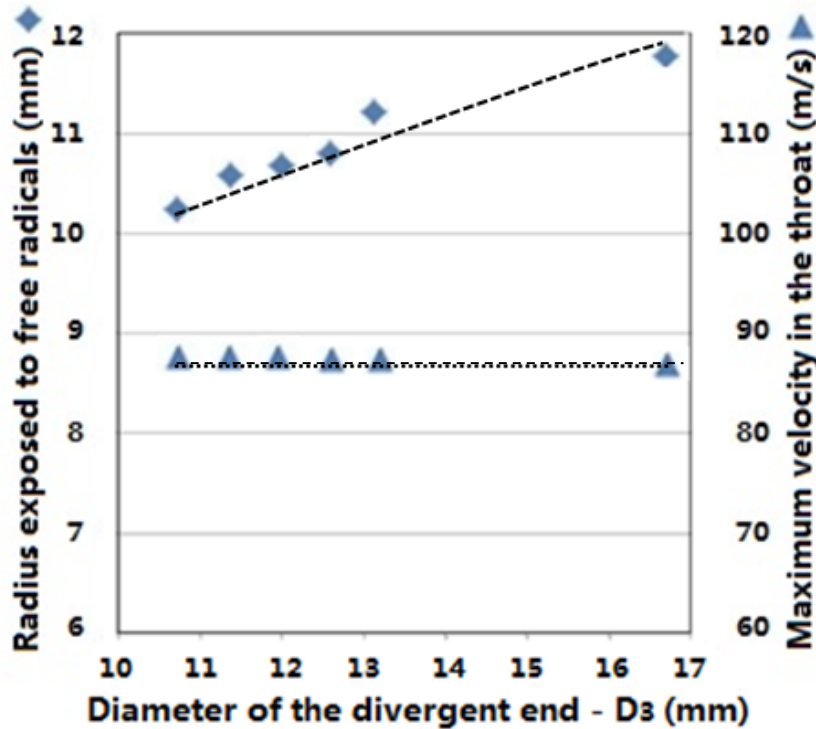


Figure 5-18 The divergent end dimensions (D_3) versus the radius exposed to free radicals (♦ left), and D_3 versus the maximum velocity in the throat (▲ right)

5.2.2.3 Effect of the Divergent Path Dimension

Through this third investigation, the influence of the dimension of the divergent path - parameter h_3 - is analysed. Here two scenarios are investigated.

First scenario: the diameter of the divergent end is kept constant at 11.4mm. Thus the change of divergence path dimension affects the divergent angle which consequently increases. Unlike the last two comparisons, the obvious change of the divergent depth doesn't change the radius exposed to free radicals (Figure 5-19).

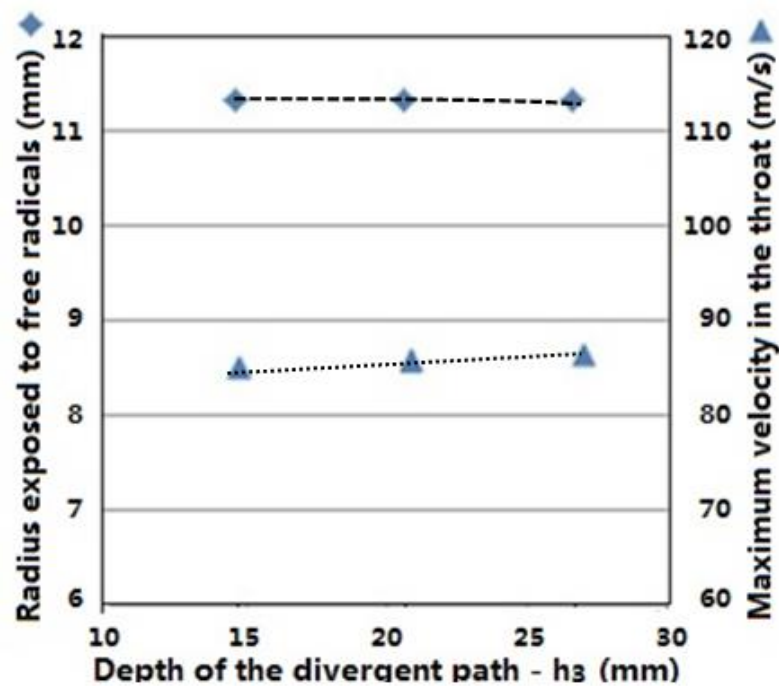


Figure 5-19 The depth of the divergent path (h_3) versus the radius exposed to free radicals (♦ left), and h_3 versus the maximum velocity in the throat (▲ right). (Divergent angle changes with h_3)

Second scenario: the angle of divergence is kept constant and therefore the divergent path dimension is altered. It can be seen in Figure 5-20 that the short nozzle reduces the radius exposed to free radicals. However, the response from h_3 is not obvious comparing to that of D_2 and D_3 .

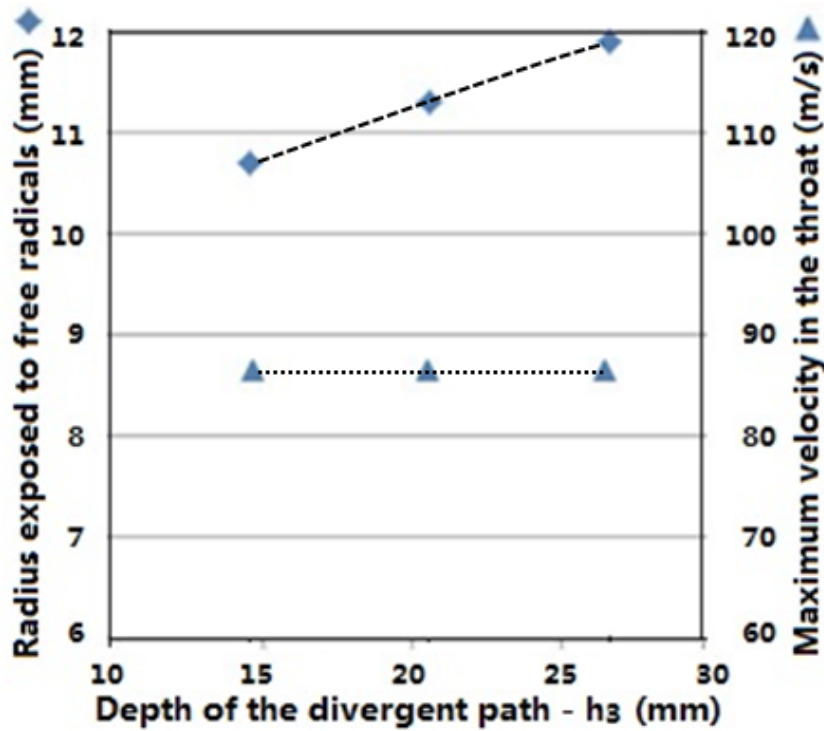


Figure 5-20 The depth of the divergent path (h_3) versus the radius exposed to free radicals (♦ left), and h_3 versus the maximum velocity in the throat (▲ right). (Divergent angle is kept constant)

These last two sets of results are complementary and they enable to correlate the radius exposed to free radicals and the diameter of the divergent end. Moreover, from the series of results obtained through this initial modelling work, there are three general design rules of the De-Laval nozzle:

1. Radius exposed to free radicals decreases significantly as the throat (D_2) shrinks;
2. Radius exposed to free radicals decreases when the divergent end (D_3) shrinks.
3. Smaller energy beam footprints should be achieved with adjustment of D_2 as it is more efficient than tuning D_3 .

5.2.3 CFD optimized nozzle versus original nozzle

In this section, CFD modelling was utilized to investigate the aerodynamic properties of a plasma jet streamed through two De-Laval nozzles. These

nozzles were the original and one of the enhanced nozzles (evaluated in 5.2.2). The temperature distributions in the domains are displayed in Figure 5-21.

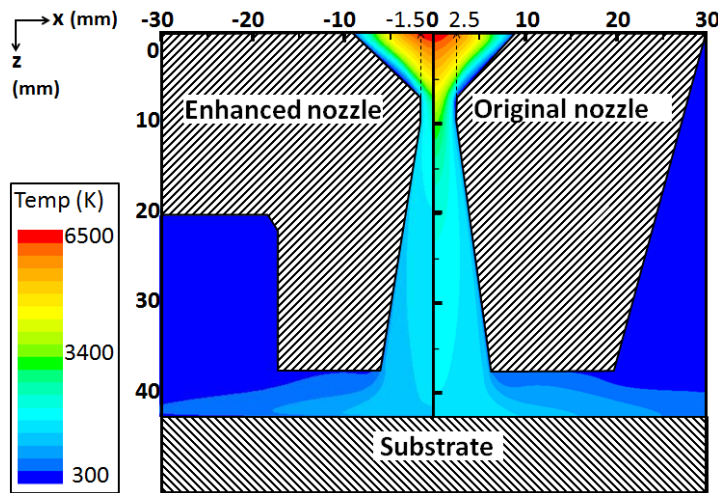


Figure 5-21 Temperature map of gas mixture: enhanced nozzle (left), original nozzle (right)

Temperature and velocity data were logged along the symmetric axis (Figure 5-22) and along the impinged surface (Figure 5-23).

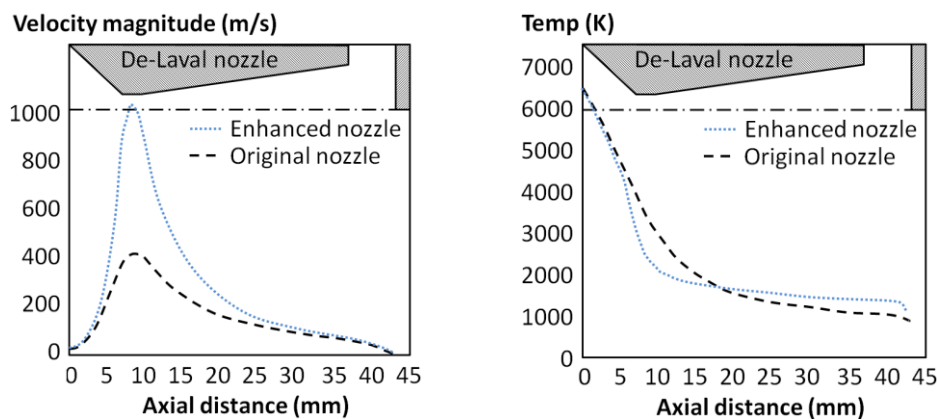


Figure 5-22 Axial profiles of velocity (left) and temperature (right) along the symmetric axis

Along the axis of symmetry, gas velocity magnitude of the enhanced nozzle is faster. In the throat section -10 mm axial distance-, this velocity is 2.5 times higher (Figure 5-22, left). On the other hand, the temperature of the jet is 500 K higher (Figure 5-22, right) at an axial distance where gas impinged the processed surface -44 mm axial distance-.

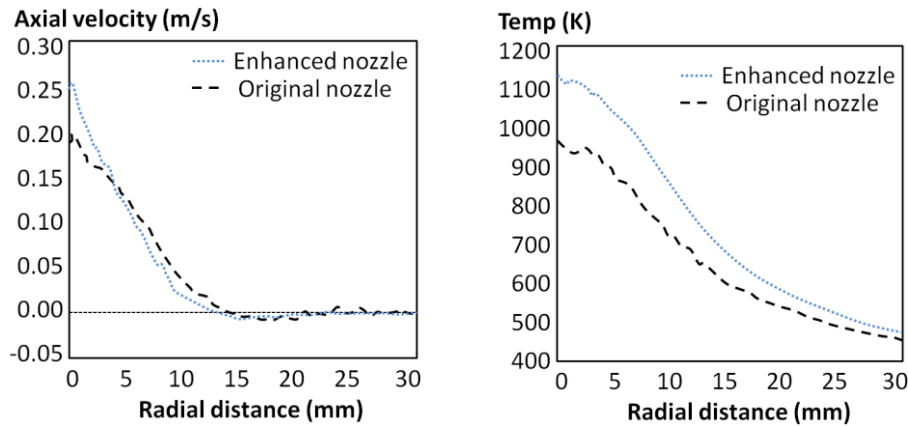


Figure 5-23 Radial profiles of axial velocity (left) and temperature (right) along the impinging surface

Onto the impinged surface, results show that the radius profile of the axial velocity is marginally smaller (Figure 5-23, left) and the maximum gas temperature is increased by 150 K (Figure 5-23, right).

5.2.4 Summary

A CFD model based on the High Temperature Jet (HTJ) was developed for a De-Laval nozzle. This model was tested against the plasma torch model developed by Morsli and Proulx [1] with an acceptable degree of agreement. Compared to plasma models, this model proved that the use of HTJ is sufficient for the actual De-Laval nozzle design characterization. In fact, the numerical results of this model highlighted that appropriate profiles of temperature and velocity applied on the nozzle inlet with reduced computational time. This model enabled the investigation of the entire aerodynamic behaviour of HTJ from the nozzle inlet up to the processed surface.

Some initial design rules and nozzle parameter sensitivity analysis has been obtained. This information can be used to create a number of new nozzle designs for experiments (in Section 5.4).

In the last part of this section, it highlights the increased performance of an improved nozzle design. This nozzle is expected to enhance the processing capability of plasma figuring by reducing the MSF errors. This enhanced nozzle is predicted to deliver a 12.5% smaller footprint and 15.5% higher temperature.

5.3 Result - power dissipation analysis of ICP torch

This section focuses on the power dissipation mechanisms of the bespoke ICP torch and its efficiency. Experiments were carried out to assess the power dissipation in two key components of this plasma torch. The increases in temperatures of the coolant in both coil and De-Laval nozzle were recorded and analysed. Energy dissipation rates were derived from these two sets of results. This method presents an alternative way to estimate the power dissipation of a plasma torch. This will enable us to test nozzle designs from the viewpoint of power dissipation in the next step (Section 5.4).

5.3.1 Results of measurement of coolant (flow rate and temperature)

5.3.1.1 Flow rate of coolant

Figure 5-24 (left) displays the reading from flowmeter that was used to measure the flow rate of coolants through the coil (Figure 5-24, right). The read flow rate valve was correlated with standardised values through conversion chart (Figure 5-24, left). The measured flow rate is $388 \text{ cm}^3 \text{ min}^{-1}$ (0.388 L min^{-1}). So the actual coolant flow rate through the coil is $369 \text{ cm}^3 \text{ min}^{-1}$ (0.369 L min^{-1}).

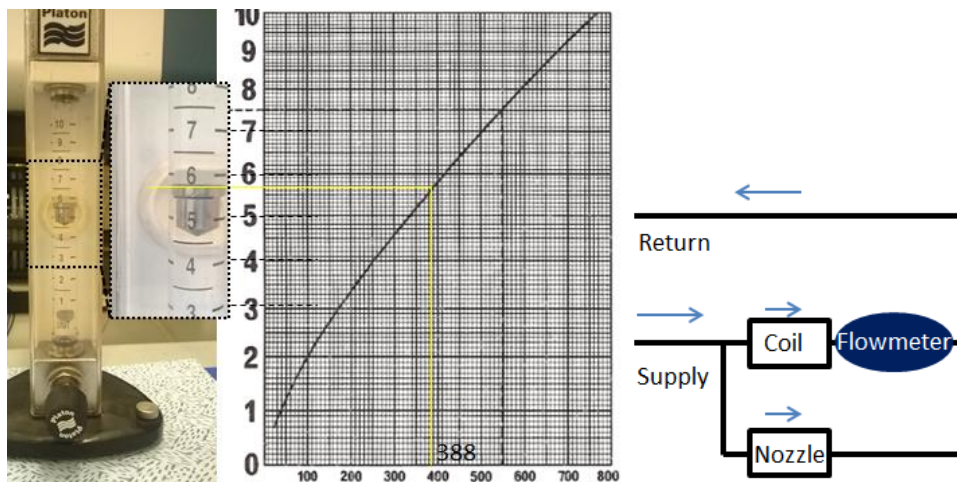


Figure 5-24 Photo of the reading (left) and the measurement position on the pipe through coil (right)

The aforementioned method was used to measure the coolants flow rate through the nozzle (Figure 5-25) and the total return pipe (Figure 5-26). The flow rate through nozzle was $1188 \text{ cm}^3 \text{ min}^{-1}$ (1.188 L min^{-1}), and through the Return total pipe was $1558 \text{ cm}^3 \text{ min}^{-1}$ (1.558 L min^{-1}).

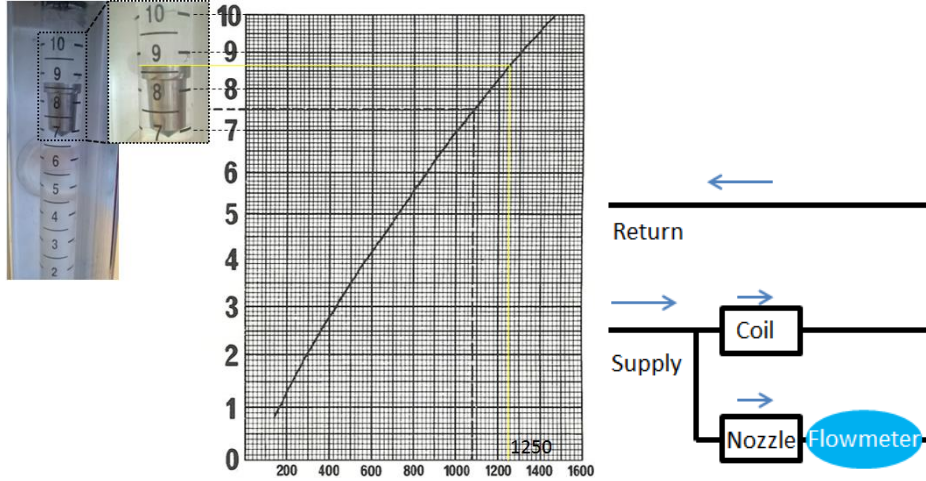


Figure 5-25 Photo of the reading (left) and the measurement position on the pipe through nozzle (right)

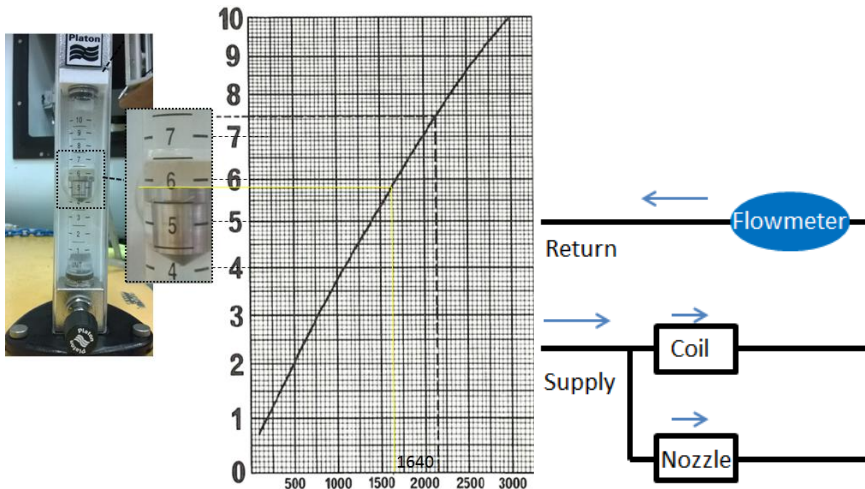


Figure 5-26 Photo of the reading (left) and the measurement position on the total return pipe (right)

5.3.1.2 Temperature logs of coolant in E-mode plasma

Following the same procedure of that in 4.3.2.5, a further six identical trials (RF signal switched on, plasma ignition, and RF power ramped up from 300 up to

800W) were carried out. The experiments were carried out at atmospheric pressure in capacitance dominated plasma mode (i.e. E-mode).

The temperature logs of coolant in this mode are shown in Figure 5-27. From the 1st to the 4th trial, the RF power was increased from 0 to 800 W through the incremental increase of 100 W every 60 seconds. In the 5th trial, the RF power was systemically increased by 50 W every 30 seconds. In the last trial, each RF power was systemically increased by 100 W every 120 seconds.

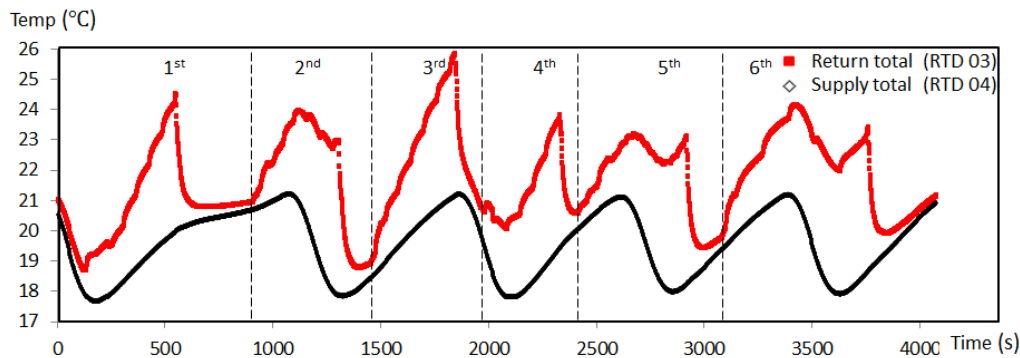


Figure 5-27 Temperature measurement logs of the coolants using RTD

5.3.1.3 Temperature Difference (TD) of the coolant in E-mode plasma

The previous results (in 4.3.2.2 and Figure 4-22) highlighted the influence of the main chiller thermal cycle then it was decided to present the next set of results based on the difference of temperature. Also, the logs displayed in Figure 5-27 enable to determine the absolute response of the Plasma Delivery System.

The TD between the inlet and outlet coolant of the torch assembly was calculated by subtracting (Supply total - Return total). The inlet temperature of coolant was measured by the RTD 04 (Supply total in Figure 5-27) and the outlet temperature was measured by the RTD 03 (Return total in Figure 5-27). The TDs are displayed in Figure 5-28. This set of results highlighted that the TD values is not constant even after 2 minutes, therefore, a 7th trial was carried out with a longer duration.

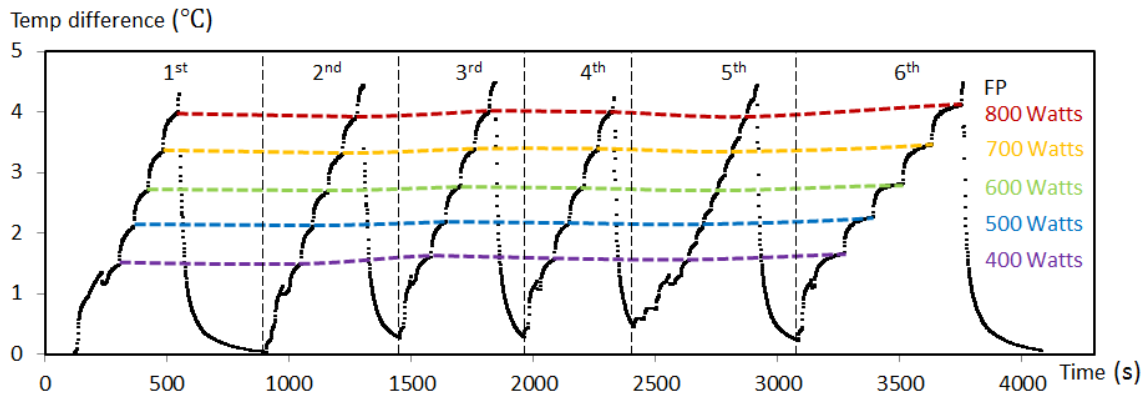


Figure 5-28 Temperature differences of the coolants through ICP torch (1st to 6th trial)

The TD result of the 7th run is displayed in Figure 5-29. RF power at 800 W lasted for 5 minutes and the value tends to be stable (4.5 °C) after its 3 minutes. This value will be used to calculate the energy dissipation in the next trial.

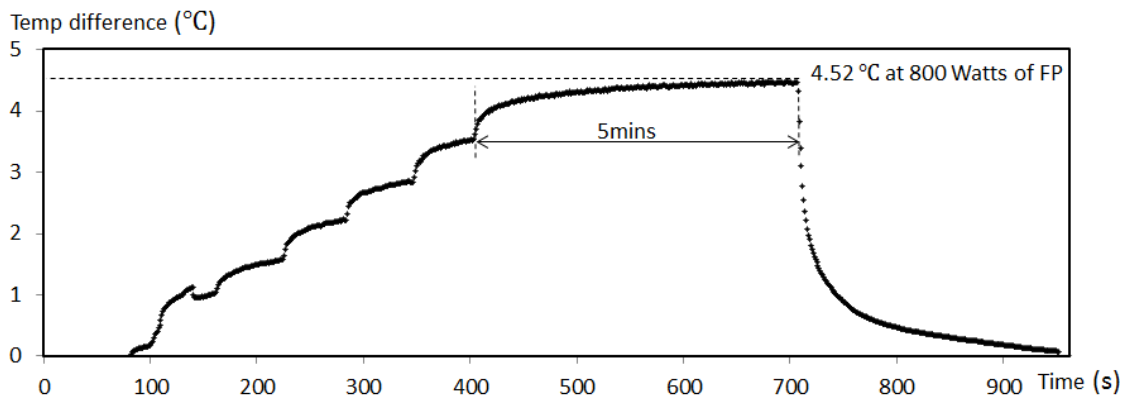


Figure 5-29 Temperature differences of the coolants through ICP torch (7th trial)

During the 8th run, the RF power was systemically increased with 100 W every 3 minutes. The TD result of each RF power is displayed in Figure 5-30. This result enabled to correlate RF P power value and TD.

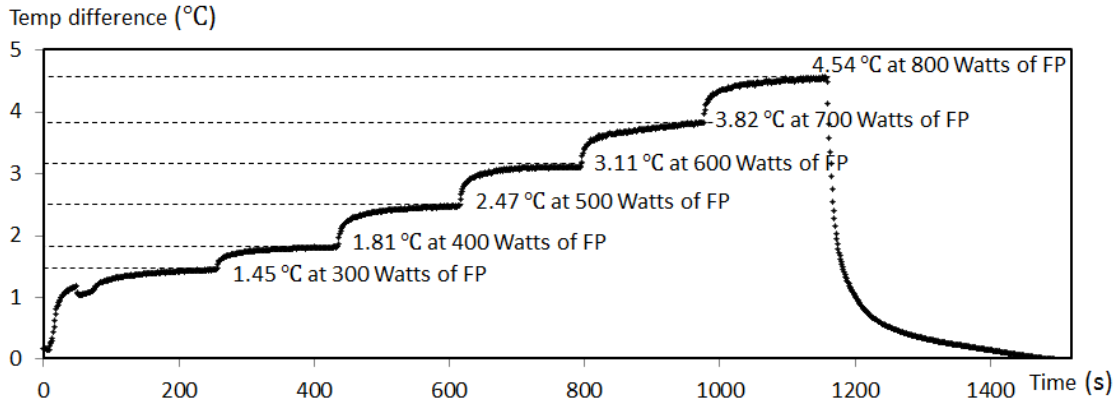


Figure 5-30 Temperature differences of the coolants through ICP torch (8th trial)

During the next sets of experiments under the condition of E-mode plasma, the RF power was also increased from 300 W up to 800 W. Four RTD sensors (01-04) were recorded. The TD of the coolant between the inlet and coil or nozzle was calculated by subtraction of recorded values obtained. The TD results for each RF power step are displayed Figure 5-31. The RF power was stepped up by increments of 100 W that lasted 3 minutes. This test duration for each increment enabled the torch components to reach thermal stability and provide robust temperature records.

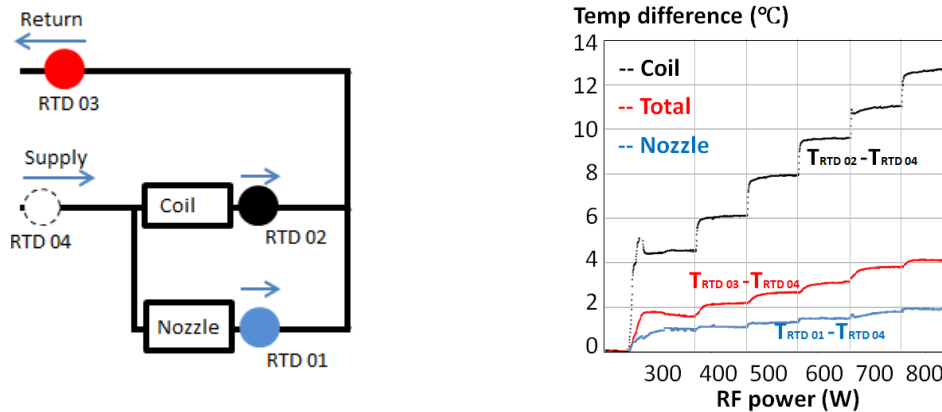


Figure 5-31 Left: schematic of the coolant circuit. RTDs were positioned at four key points of the coolant circuit; Right: temperature difference of coolant channels: coil, nozzle and total

After a set of repetitive testing, the range of TD at each RF power is drawn in Figure 5-32. These results enable to correlate RF power and TD values for coolant channels at each key location where RTDs were set.

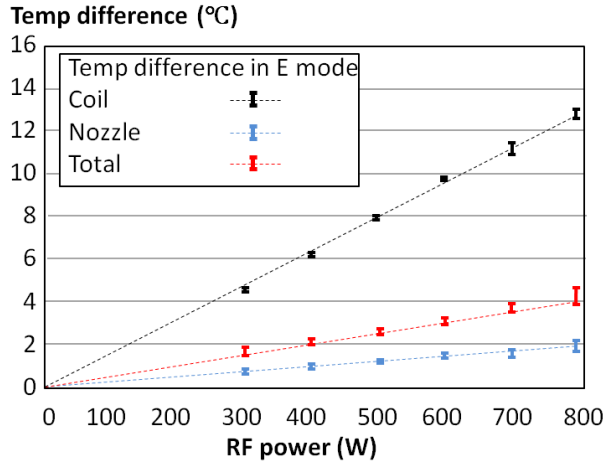


Figure 5-32 RF power versus temperature difference

5.3.2 Power absorbed by coolants in E mode

These results were used to determine the power absorbed by the coolant in E mode. Therefore, each RF power value -steady state - the energy dissipated by coolants was calculated using (5-1).

$$\Delta E_{\text{coolant}} = C_{pc} v_c \Delta T \quad (5-1)$$

where C_{pc} is the specific heat capacity of coolant ($= 3.14 \text{ kJ kg}^{-1} \text{ K}^{-1}$);
 v_c is the flow rate ($= 1055.7 \text{ kg m}^{-3} \times 1.57 \text{ l min}^{-1} = 1.645 \text{ kg min}^{-1}$);
 ΔT is the TD value of coolants for each RF power value set.

Substituting these experimental values into (5-1), the power dissipated by the coolants in E mode was calculated (Figure 5-33).

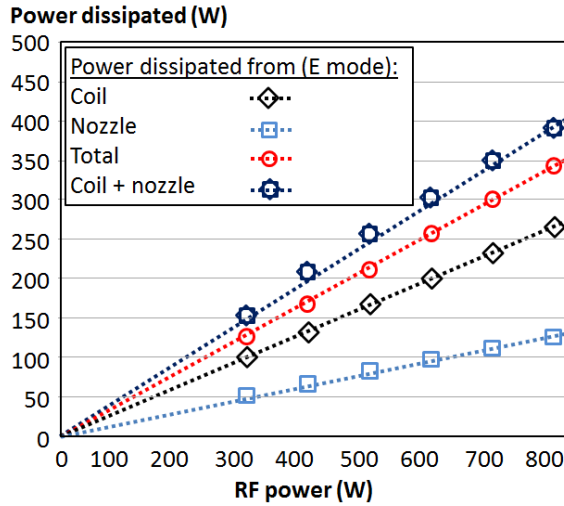


Figure 5-33 RF power versus power dissipated for each coolant channel in E mode

Figure 5-32 and Figure 5-33 enable to observe that a near linear correlation exists between RF power values and both TD and power dissipated values in E mode for the range 300 W up to 800 W.

The value of the total power dissipated by the coolants is calculated for an 800 W power supply. This value was 355 W. The throughout investigation highlighted that the power dissipated in the nozzle coolant was 124 W whereas the coil coolant dissipated 266 W. The sum total of power dissipated by the coil and nozzle coolant was 390 W, which is 8.97 % higher than the measured total power dissipated value. It was considered that the difference is due to the heat loss from the hose between RTD 01/02 and RTD 03 (see Figure 4-20).

5.3.3 Uncertainty analysis

The uncertainty analysis was carried out for power loss, temperature and mass flow rate measurements. The uncertainty was estimated according to the method described by Dietrich [140] and Bell [141]. The uncertainty budget is given in Table 5-3.

The uncertainty in the dissipated power at 800 W RF power is estimated. The result of coolant's power dissipation is 355 W and the uncertainty is 9 W. The

overall uncertainty calculation uses the coverage factor (k) equal to two. This investigation provides a confidence level of 95%.

The mean TD at 800 W RF power was 12.9 °C, and the standard deviation is 0.2 °C. Standard uncertainty of mean of 10 repeated readings is 0.0633 °C (divided by $\sqrt{10}$). The RTD sensors calibration uncertainty was 0.385%. Thus the standard uncertainty u (for $k=2$) was 0.0248 °C. The resolution of reading was 10^{-6} °C.

The mean mass flow rate of total coolant was 1.645 kg min⁻¹ with 3 repeated readings. The estimated standard deviation was 20 g min⁻¹. The accuracy was $\pm 1.25\%$ of reading. Thus the correction uncertainty was 20.56 g min⁻¹.

Table 5-3 Uncertainty budget of the power dissipation of coolant

Source of uncertainty	Value (\pm)	Probability distribution	Divisor	Standard uncertainty
Coolant temperature	10^{-3} °C			10^{-3} °C
TC calibration uncertainty	49.6	Normal	2	24.8
Resolution	10^{-3}	Normal	2	5×10^{-4}
Standard uncertainty	63.3	Normal	1	63.3
Combined standard uncertainty		Normal		67.98
Expanded uncertainty		Normal ($k=2$)		136.
Flow rate	g · min ⁻¹			g · min ⁻¹
Correction uncertainty	20.56	Normal	2	10.28
Standard uncertainty	1.20	Normal	1	1.20
Combined standard uncertainty		Normal		10.35
Expanded uncertainty		Normal ($k=2$)		20.7

5.3.4 Power absorbed by coolants in H mode

The phenomenon of the transition from E to H mode has been presented in 2.3.1.2. Figure 5-34 shows the ICP torch in different modes. The transition of this bespoke ICP torch occurs around 800 W. It can be noticed the amount of light radiating from the ICP torch in E mode is significantly different from that of H mode. Once the plasma transfers to H mode, it can be maintained when the RF power is reduced to 300 W. This section looks at the H-mode plasma from a quantitative viewpoint through temperature measurement of the coolant.

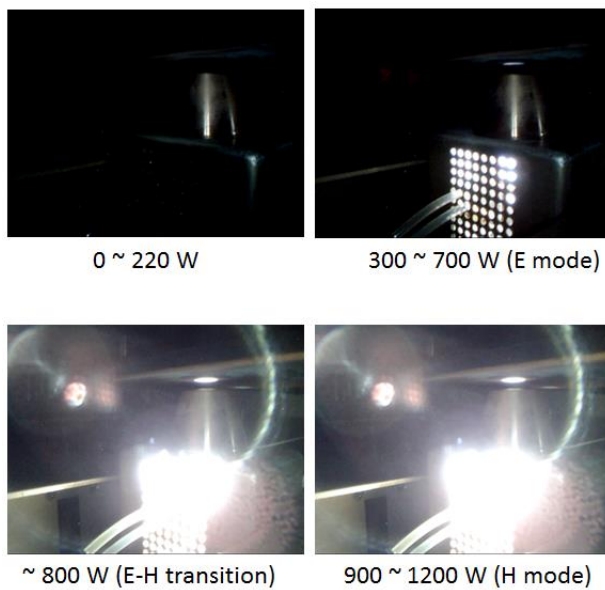


Figure 5-34 Image of the bespoke ICP torch obtained by spectrum camera

Figure 5-35 illustrates how the temperature of nozzle appears at a specific RF power in E and H modes. These images were taken under the set-up procedure introduced in 4.3.1.4. These images provide an intuitive judgment that the temperature of the nozzle increases dramatically in H mode. However, the value acquired from this thermal camera cannot be used in the calculation with data acquired from RTDs.

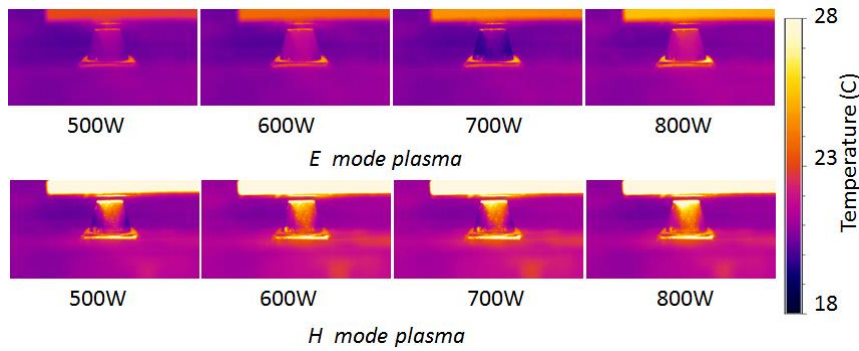


Figure 5-35 Image of the original ICP torch nozzle obtained by thermal camera

The temperature logs of coolant in both supply total and return total are shown in Figure 5-36. In this trial, the transition occurred at the RF power between 800 W to 850 W. The temperature of total return coolant drops by 1 °C. The TD values at each RF power are recorded in Figure 5-37. After the transition, the TDs still keep a good linear correlation with RF powers. This makes the calculation of power loss possible in a higher RF power (around 1200 W) through prediction of the tendency. The TD is predicted to be 4.6 °C at the RF power of 1200W. The power dissipated from the coolant in H-mode is calculated and predicated as 400W, as shown in Figure 5-38.

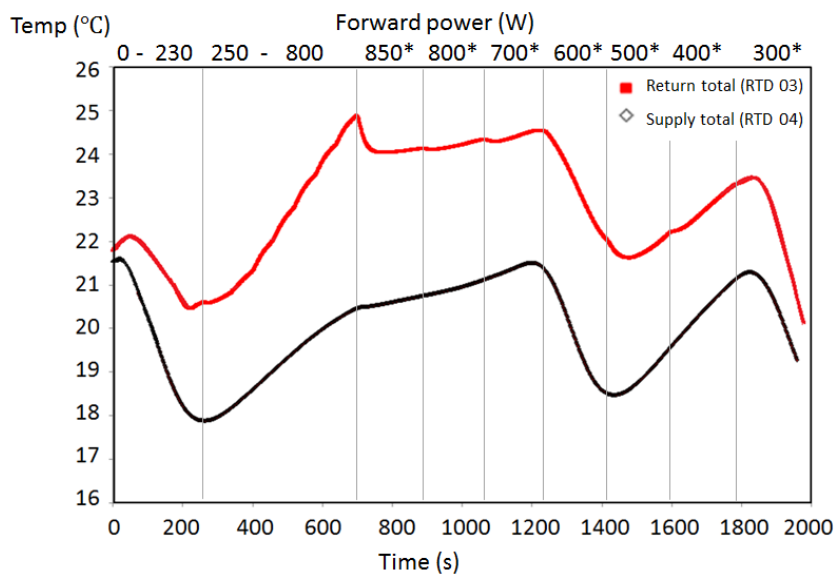


Figure 5-36 Temperature measurement logs of the coolants using RTD (Note: * marks the RF power given in H mode)

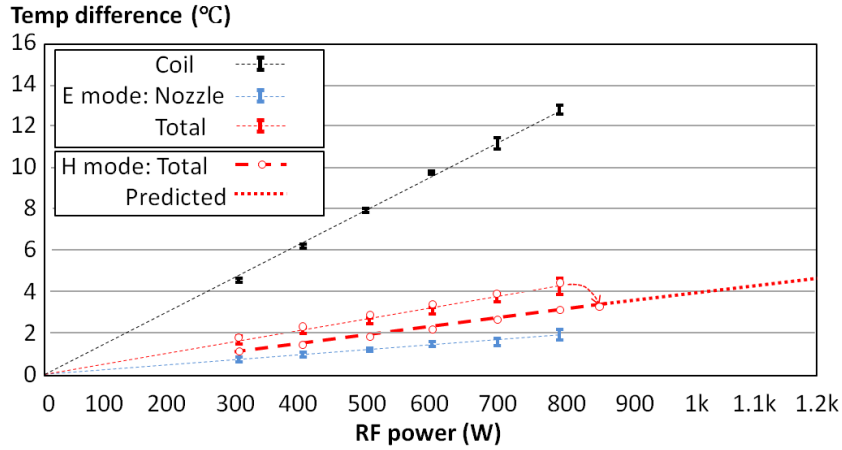


Figure 5-37 RF power versus temperature difference in E and H mode plasma

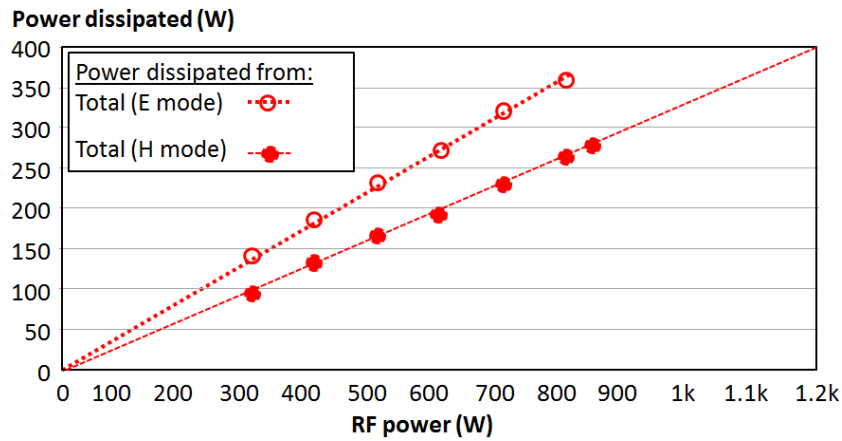


Figure 5-38 RF power versus power dissipated from the total coolant in both E and H mode

5.3.5 Power dissipated by argon gas in H mode

5.3.5.1 Temperature distribution in De-Laval nozzle

The average temperature of the HTJ in this domain is 912.25 K (Calculates the volume-weighted average on a 3D equivalent location). This result comes from the CFD simulation in 5.2.1.1.

5.3.5.2 Derivation of plasma average temperature value

Based on the linear correlation between the RF power and TD values, TD value was extrapolated for the nominal processing RF power value. Thus the deduced energy loss rate by the coolant for a 1200 W RF power is estimated to 664 W. Also, the energy absorbed by the argon gas can be calculated through (5-2):

$$E_{\text{argon}} = \int_{T_{\text{room}}}^T (C_a v_a) dT \quad (5-2)$$

where C_a is the specific heat capacity of argon given as plasma temperature dependent [142], shown as (5-3);

v_a is the gas flow rate ($=22 \text{ litre min}^{-1} = 0.0156 \text{ mol s}^{-1}$);

$$C_a = 20.79 - 3.2 \times 10^{-5}T + 5.16 \times 10^{-8}T^2 \quad (5-3)$$

The dissipated energy rate from the argon heating can be integrated using (5-4):

$$\Delta E_{\text{argon}} = v_a [20.79 T - 1.6 \times 10^{-5}T^2 + 1.72 \times 10^{-8}T^3]_{T_{\text{room}}}^T \quad (5-4)$$

$$= v_a (6090.5 + 20.79T - 1.6 \times 10^{-5}T^2 + 1.72 \times 10^{-8}T^3)$$

The fraction of the radiation losses in the total energy balance of ICP torch varied in a wide range: from 8% to 32% [143]. According to (5-2), the E_{argon} can be derived. This result is 13% to 37% of the RF power. Then the average temperature of plasma was estimated through (5-4). Values range from 481.8K to 1370K.

5.3.5.3 Estimation of power dissipated from argon gas

The rate of energy dissipated by argon gas is 394.2 W when the average temperature of argon is 912.25K (CFD result).

5.3.6 Power dissipated by radiation in H mode

The average temperature of the argon gas was calculated as 912.25K through the CFD model. This result is within the range of predicted gas temperatures mentioned in section 4.5.2 (481.8K to 1370K). That previous result was based on the energy dissipation experiment. However, the radiation losses value in [143] is not accurate enough for the overall energy dissipation estimation. The radiative energy dissipated in the present research consists of two parts: excitation region and transportation region (Figure 5-39).

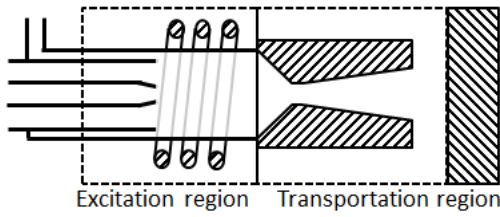


Figure 5-39 Radiation regions of the ICP torch

5.3.6.1 Radiation in excitation region

For the radiation in the excitation region, both Wilbers [144] and Benoy [145] calculated the radiative loss under atmospheric plasma condition as a function of temperature (3000K to 12000K). In the present study, the plasma temperature in the ICP torch is estimated to 10000K [95]. Therefore, the estimated radiative energy dissipated rate in the torch tube ranges from 70 W to 200 W, depending on the radius distance from the torch axis.

5.3.6.2 Radiation in transportation region

The radiative energy dissipated rate in the transportation region can be estimated based on Stefan-Boltzmann law. The radiation energy loss rate can be calculated as 203 W by (5-5),

$$E_{\text{radiation}} = e \sigma A (T^4 - T_c^4) \quad (5-5)$$

where e is emissivity of the gas (=0.8) [143];

σ is Stefan's constant ($=5.6703 \times 10^{-8} \text{ W m}^{-2} \text{ K}^{-4}$);

A is radiating area for the axis-symmetric torch ($= 6.72 \times 10^{-3} \text{ m}^2$);

T is average temperature of plasma in the nozzle ($=912.25 \text{ K}$);

T_c is the temperature of nozzle ($=350 \text{ K}$).

5.3.6.3 Estimation of radiation energy in total

The estimation of the total radiative energy rate results from the addition of the radiative energy rate due to the excitation region (70 – 200 W) and the radiative energy rate due to the transportation region (203 W).

It follows then that total radiative energy rate dissipated ranges from 273 W to 403 W, which is 22.8% to 33.6% of RF power. This calculation is also within the range of reference [143].

5.3.7 Summary

In this section, the results of measurement are analysed and the power dissipated from the coolants in E mode are calculated. This investigation provides a confidence level of 95%, after an uncertainty analysis. In H mode, the measurement of coolant temperature was carried out at the RF power of 850 W to 300 W. There is a near linear correlation between TD value and RF power in accordance with Figure 5-32. The power dissipation is also predicated as 400 W at operating RF power of 1200 W.

The power dissipated by heating the argon gas estimated through the CFD model is 394 W. This estimation does not take into account the ionisation energy of the gas.

The radiation from plasma –excitation and transportation regions– is absorbed by the surrounding parts: surrounding air aluminium tube, outer quartz tube, copper nozzle and coil. The amount of energy absorbed by those latter two parts (nozzle and coil) is already counted by the power dissipated through coolants (5.3.4). The energy absorbed by the remaining parts still needs to be defined. Table 5-4 illustrates the power dissipated by each component of the torch.

Table 5-4 Power balance of the ICP system

Input: RF power	Power dissipated	
1200W provided by RF generator	Coil coolant	272.4 W (22.7%)
	Nozzle coolant	127.2 W (10.6%)
	Gas heating	394.2 W (32.8%)
	Radiation	273~403 W (22.75 ~ 33.58%)
	Total	(88.85 ~ 99.68 %)

From this table, we can have a rough idea that in the original torch nozzle, 1/3 of the power is dissipated from the coolant, 1/3 of the power is dissipated from the gas heating, and the rest 1/3 of the power is dissipated from the radiation.

Methods to measure and calculate the power dissipation are different in each publication from another. Also, it is difficult to compare the torch efficiencies of different types of plasma torches. The method presented in this section enables to compare the different nozzle designs rapidly.

5.4 Result of power dissipation analysis of enhanced nozzle series

In this section, the design of enhanced nozzles and their performance in terms of power dissipation are presented. 5.4.1 emphasises on the mechanical design of the nozzle. With these nozzles' manufactured comparisons of nozzle performances were carried out using the power dissipation method. The results of this comparison were discussed in 5.4.2.

5.4.1 Design and manufacturing of enhanced nozzles

This section presents the design of a combined nozzle for an ICP torch used in optical fabrication. The research is aimed to investigate the effect of nozzle design parameters on the material removal footprint. New nozzles are expected to be used in experiments of power dissipation and material removal footprint, which enables validation of the 2D axis-symmetry numerical model created for the CFD simulation.

The design is based on the existing nozzle to a large extent. One of the big improvements is that the detachable structure enables the dimension of the inner wall of the nozzle to be changed. Therefore, the convergent-divergent size can be changed during the validation trials.

5.4.1.1 Existing nozzle

The existing nozzle designed and made by RAPT Industries is shown in Figure 5-40. It is composed of three parts: aluminium ring, copper nozzle, and outer shell. The quartz tube of the ICP torch is mounted into the aluminium ring. Aluminium is considered to have a better glass-to metal seal than copper. Copper with a good thermal conductivity and high melting point (1085°C), is chosen for the De-Laval nozzle, to work in the plasma of thousands of degrees and surrounded by a chilling groove. The spiral cooling pipe is a helix tube between the copper nozzle and outer shell, and it is connected to the flange of the ICP torch.

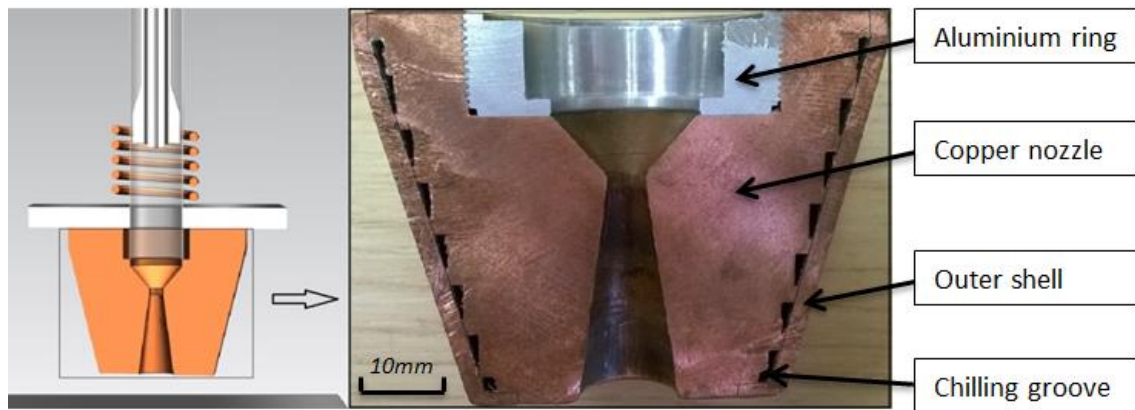


Figure 5-40 Cross section of existing nozzle

5.4.1.2 New nozzle design

The newly designed nozzle will be used to match up with the existing ICP torch flange, so the parameters of the junction are limited, including the inner diameter of the aluminium ring, the diameter of the convergent part D_1 , the position of the chilling pipe, as well as the screwed holes. In Figure 5-41, the aforementioned parameters are shown in the existing ICP torch and its flange.

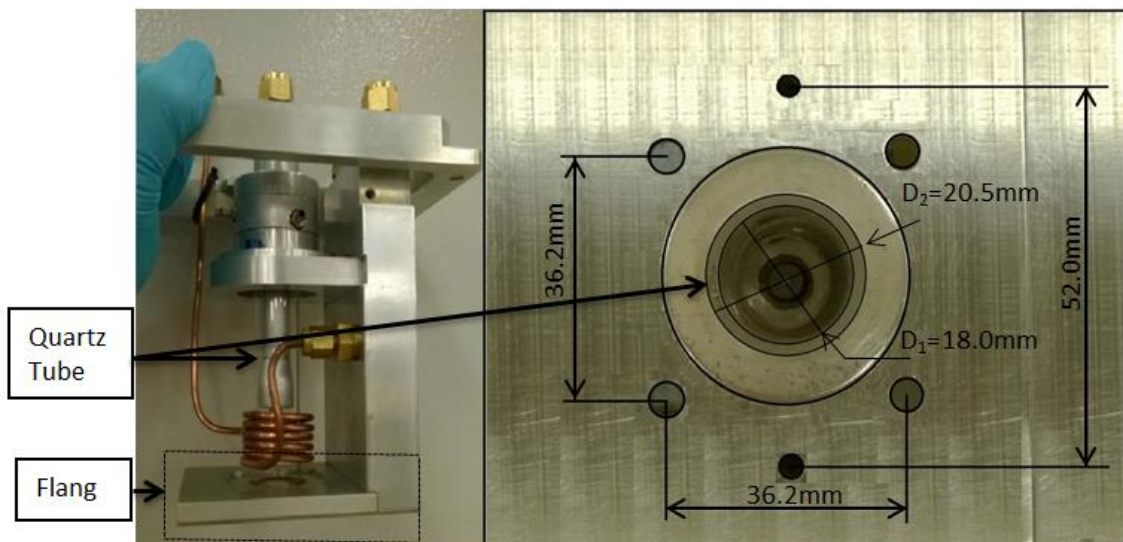


Figure 5-41 Left: ICP torch; Right: the dedicated flange (top view)

In order to investigate the effect of inner parameters on the footprint, the nozzle is designed as detachable. It will lead to a flexible adjustment of nozzle parameters in the following experiments, enabling convenient comparison with different nozzle sizes. So the copper nozzle is divided into two parts with

different missions: De-Laval ring for transporting plasma and mid ring for the cooling system, as shown in Figure 5-42. With a screw joint, the De-Laval ring can be twisted off and replaced by another one.

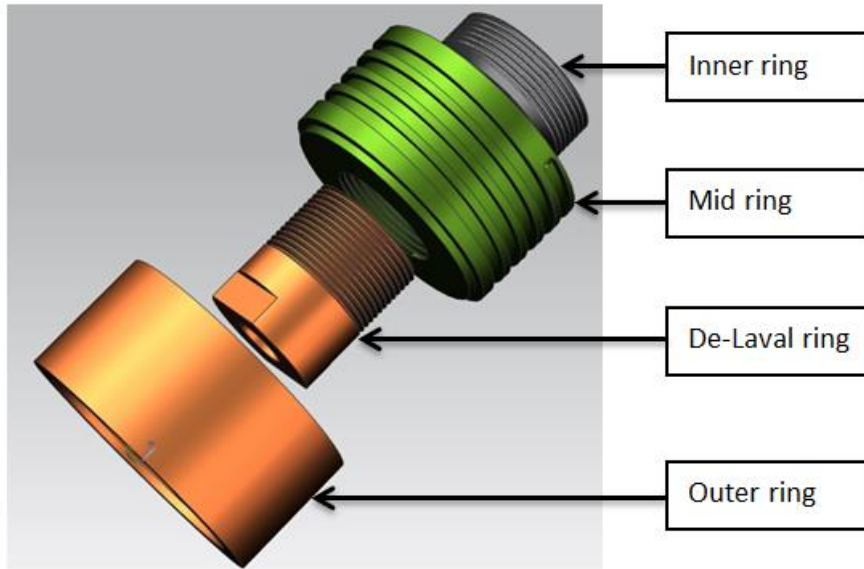


Figure 5-42 Four parts of the new nozzle

Figure 5-43 shows the assembly of the new nozzle, and the engineering drawing can be found in the appendix. Figure 5-44 illustrates the assembly diagram of the new nozzle and existing flange. We can see that there is a bolted connection between the flange and mid ring of the nozzle. It is a shrink fit that combines the mid ring and out shell together, which makes sure the chilling groove is sealed well.

Aluminium alloy 6082 with t6 temper has very good corrosion resistance and higher strength than other aluminium alloys. It is adopted to make the inner ring. The other three parts are made of copper. Copper is also resistant to corrosion well in atmospheres and is considered one of the best conductors. Copper alloy CW024A is used to make those parts. Table 5-5 displays the properties of a related material selected for those parts.

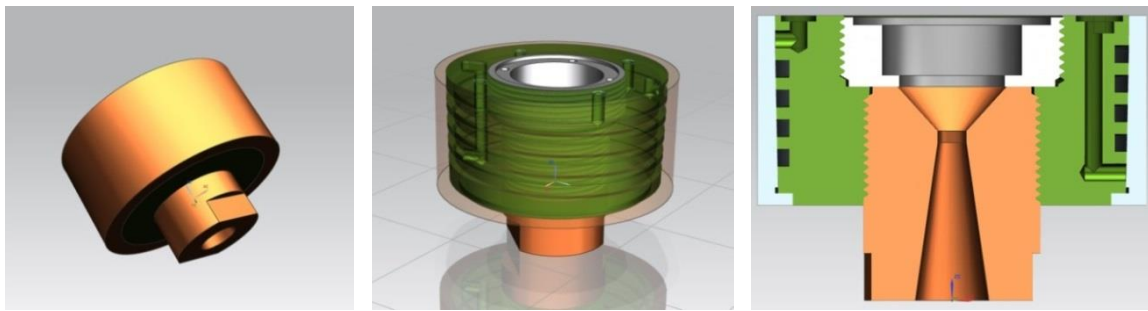


Figure 5-43 Assembly of the new nozzle. Left: external view; Middle: perspective drawing; Right: cross section with flange

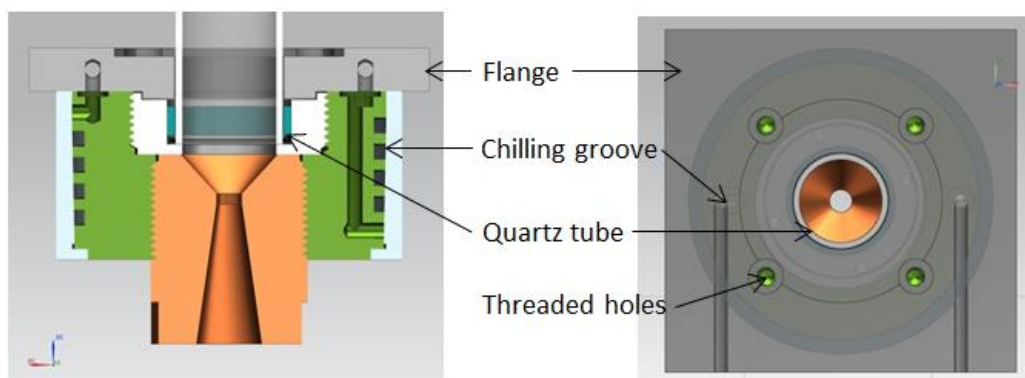


Figure 5-44 Assembly diagrams of the new nozzle and existing flange. Left: section view; Right: top view

Table 5-5 Parameters of related material

Material	Aluminium (6082-T6)	Copper (CW024)	Note
Tensile strength [MPa]	340	200 - 400	
Hardness [HV]	100	120	
Machinability rating	Good	20	Alloy 360 FC Brass is 100
Melting point [°C]	555	1083	
Thermal conductivity [$\text{W m}^{-1} \text{K}^{-1}$]	180	391.2	
Thermal expansion [K^{-1}]	24×10^{-6}	16.9×10^{-6}	

Figure 5-45 gives the comparison of 3D drawings between the existing and new torches.

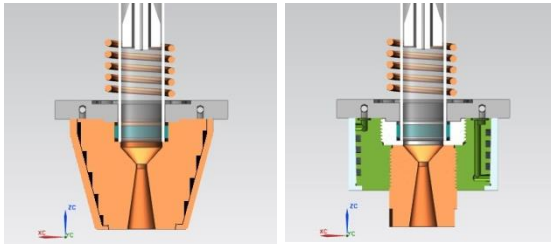


Figure 5-45 3D drawings of existing and new nozzle

Table 5-6 illustrates the dimensions of all the nozzles designed and manufactured. The critical parameters (D_{1-3} and h_{1-3}) were introduced in Table 5-6, and λ is the angle of divergence. According to the one-factor-at-a-time (OFAT) method, D_3 varies among nozzle No.1-3, D_2 varies among nozzle No. 3-5, h_3 varies among nozzle No. 3, 6, 7, while D_3 is kept constant at 11.4mm, and h_3 varies among nozzle No. 7-9, while λ is kept constant at 24.7° .

Table 5-6 Dimensions of the original and enhanced nozzles

No.	Ori	1	2	3	4	5	6	7	8	9	10
D_1	18	18	18	18	18	18	18	18	18	18	18
D_2	5	5	5	5	4.7	4.3	5	5	5	5	3
D_3	12.6	12.6	12	11.4	11.4	11.4	11.4	11.4	N	16.7	11.4
h_1	7.5	7.5	7.5	7.5	7.5	7.5	7.5	7.5	7.5	7.5	7.5
h_2	2	2	2	2	2	2	2	2	2	2	2
h_3	26.6	26.6	26.6	26.6	26.6	26.6	20.6	14.6	20.6	26.6	26.6
λ	N	N	N	N	N	N	N	24.7	24.7	24.7	N

5.4.2 Power dissipation comparisons

The enhanced nozzles were tested using the power dissipation method (documented in Section 5.3). In order to compare these nozzles, two groups of experiments were carried out. In the first group of experiments, there was a 6 mm standoff distance between each nozzle and the substrate. Nozzles of No.6, No.7 and No.8 were not tested in this group, as the lengths of these three nozzles are much shorter than the rest. In the second group of experiments, all the nozzles were tested without the substrate. Measurements of each nozzle were undertaken 3 times, and average results of power dissipated were determined. Figure 5-46 illustrates the predicted power dissipated from coolant at 1200 W RF power.

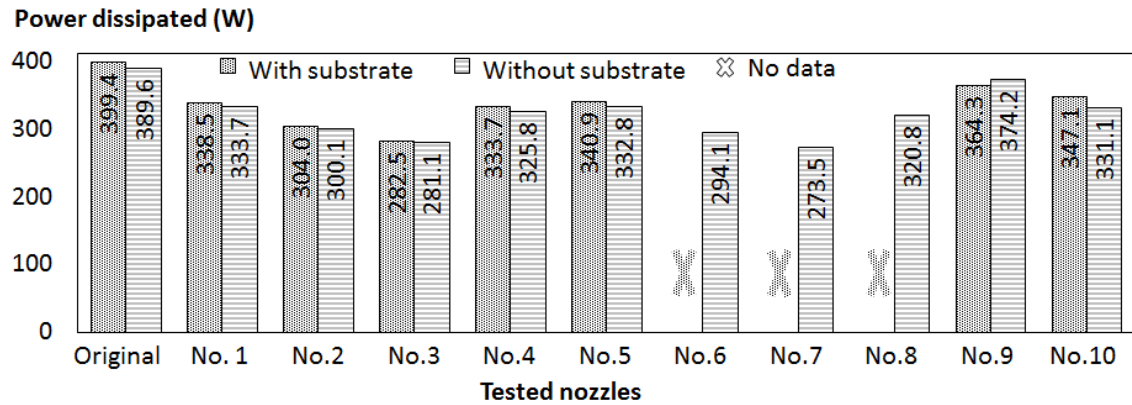


Figure 5-46 Predicted power dissipated of enhanced nozzles when RF power is 1200 W

Among those two sets of comparison, two clear differences can be noticed. First, the powers dissipated from all the enhanced torch nozzles were lower than that of the original torch nozzle. There was about 15% less power dissipated from the coolant in the ICP torch associated with the nozzle No.1, which has the same internal dimension with the original De-Laval nozzle. This phenomenon can be attributed to the significantly different design of the new nozzle assembly from the original one. Second, the power loss of a torch underneath of substrate is slightly higher than that without a substrate. This is considered because of the energy reflection from the substrate. However, there is only one exception in the

measurement of nozzle No.9. More convictive explanation will be given after further investigation on this typical nozzle dimension.

From the comparison of magnitudes, nozzle No.3 has the smallest power dissipation when there is a substrate, and second smallest value without a substrate. Nozzle No.7, with the shortest depth, has the smallest power loss when there is no substrate.

5.4.3 Summary

In this section, a unique design of nozzle is introduced. To fulfil the need of nozzle quick-change, the nozzle is separated to two main parts: main body (as the interface to the existing torch) and a series of De-Laval rings (with different dimensions of inner walls). One of the big improvements is that the detachable structure enables different De-Laval rings to be changed rapidly. This design was proven beneficial to the experiments recorded in 5.4.2.

In order to select the nozzles with higher efficiency regarding heat transfer, all the enhanced nozzles were tested based on the method of power dissipation calculation. Result, which is shown in Figure 5-46, proves that the power dissipated from the enhanced nozzle is less than that of original nozzle. Among the ten nozzles, nozzle No.3 (with the smallest diameter of the divergent end) was selected as with the smallest amount of power loss when there is a substrate upon the torch nozzle. Nozzle No.7 has the smallest amount of power loss when there is no substrate, due to its shortest depth.

6 Discussion

6.1 Numerical approach and its result

The understanding of the fluid dynamic behaviour of plasma flow settled between the inner part of the De-Laval nozzle and nearby surface requires a deep knowledge of physics and a fine analysis of the processing conditions. Then some aspects of the model and experimental results are discussed hereafter. Three aspects are detailed: validation approach, model results, and nozzle design rules.

The validation approach of the CFD model was carried out by comparing axial pressure and temperature profiles with the benchmark model found in [1]. As presented in 4.2.1.4, a discrepancy error of 5% was obtained. This error was attributed to the dependency on the pressure and the chemical composition of the plasma. However, the main point of this work is the creation of a model that supported and increased the understanding of the plasma jet under real and specific processing conditions. Like other researchers' (Wang et al [137]), the plasma figuring activity experienced strong changes of plasma temperatures, velocity and density when a substrate is added to the experimental configuration. Unlike others experimental setups [120,147–149] -used in plasma spraying process- where an 80mm standoff distance enabled measurements, the present configuration -6mm standoff- limited direct experimental validation. This confined space would affect an OES investigation, where unwanted reflections of the light by the substrate and nozzle will degrade the collected spectrum quality. The harsh environment and the short standoff distance made measurements extremely challenging. Thus it was considered that an alternative method was required to correlate results of the CFD model with quantitative outputs.

Based validation stage outcome, the CFD model provided a sound ground for the scientific understanding of the flow dynamics in the nozzle, when the flow was impinging a flat surface at a short distance. The two assumptions were made -HTJ instead of plasma and parabolic profiles of temperature and velocity

- enable to reduce the complexity of the model. Consequently, the computational time was reduced without degrading the quality of the results.

The design of nozzles that are used for conveying subsonic plasma flow can be assisted by the present approach. In fact, the effects of different parameters of the nozzle can be investigated and adjusted for obtaining a specific velocity footprint of the gas flow. However, the present work benefited of an enhanced model is a model more capable of estimating the optimum design parameters for a given material processing flow velocity and material removal footprint.

6.2 Power dissipation analysis

An alternative method for the calculation of the power dissipation inside a plasma torch is given in Section 5.3. This project emphasises on the temperature measurements of coolant in the plasma system and its performance. All the experiments were conducted in the E-mode plasma discharge when the input power was set below 800 W. Several aspects which might affect the measurement quality have been taken into account and presented.

This method provides an in-direct measuring approach to deduce the power dissipated by the coolant. The RTDs provide an immediate record and reliable read of the coolant temperature at specific positions. Thus, it overcomes the difficulty of the direct measurement for the impinging jets. However, the introduction of some RTDs, which are closed to the induction coil, leads to the interference between RTDs and the EM fields.

Three results are analysed: the thermal cycle of the chiller, nominal gas flow, and the power dissipated. Firstly, a 3.5 °C variation amplitude of the thermal cycle of coolant unit was highlighted. It was not observed directly either the effect of this variation or its effect on the torch behaviour. However, it was recognised that temperature around 15°C favour condensation on the coil. That phenomenon is known to lead to torch damage through an electrical breakdown. Thus, it is recommended a particular attention on the quality of the chiller and humidity of the surrounding air. Secondly, a 3.5% deviation from the

nominal gas flow value was correlated with the intensity of EM field. Researcher is not in the capacity to provide a firm explanation for this observation. Lastly, it was calculated that the value of the total power dissipated by the coolants for a 1200 W power supply. This value was 399.6 W. The throughout investigation highlighted that the power dissipated in the nozzle coolant was 127.2 W whereas the coil coolant dissipated 272.4 W. An uncertainty value of 9 W was calculated based on a standard uncertainty principle. This analysis provides a level of confidence of 95 %.

In E mode plasma, the torch efficiency η is the ratio of the plasma jet power P_{plasma} to the total input RF power P_{input} ($\eta = P_{\text{plasma}} / P_{\text{input}}$) [143]. The torch efficiency value of the bespoke torch operated under E-mode was 48.8%. This value is higher than the one measured by Reed [73], Miller [119], and Gutsol [143]. The aforementioned researchers claimed 45%, 34% and 48% efficiency respectively. However, the bespoke torch did not reach the efficiency of the torch reported by Merkhouf [146] and Chen [127]. Merkhouf and Chen reported 55% and 66% efficiency for two different regular ICP torches. It was considered that the copper nozzle in the bespoke torch coupled a great amount of power comparing to Merkhouf's and Chen's.

Methods to measure and calculate the power dissipation are different in each publication from another. Also, it is difficult to compare the torch efficiencies of different types of plasma torches. The reason is that aluminium permeability constant induces strong coupling with the EM fields. The use of ceramic or dielectric materials would be beneficial. However, the integrity of these materials may degrade due to the short distance to the plasma core. Also, these materials are prone to thermal shock due to their low thermal diffusivity. Finally, it is suggested that the design of a nozzle made of non-conductive material (e.g. Alumina or ULE) will be beneficial for the torch efficiency.

7 Conclusion

Objective 1: Improvement of the PDS performance – assessment of the influencing factors and determination of the optimum tuning parameters.

The study of the fixed matching RF network PDS adjustment enabled to determine the optimum tuning of both Tune and Load capacitors. The reflected power values observed was less than 10 W for forwarded power values that ranged from 200 W up to 1 KW. However, it should be mentioned that the original torch was performing in E mode only. The research on the coil highlighted the effect of the coil length on both frequency and ignition power. The sensitivity of coil length is 0.065, which is more than twice of load capacitance sensitivity value (0.025) but still much lower than tune capacitance sensitivity value (2.5). The optimum coil length was 23.5 mm. An optimum tuning of three system parameters was recommended.

Objective 2: Numerical analysis of De-Laval nozzle – Investigation of the aerodynamic property through computational fluid dynamics (CFD) simulation and analysis of the De-Laval nozzle design using the CFD model.

A CFD model based on the High Temperature Jet (HTJ) was developed for a De-Laval nozzle. This model was initially validated against the plasma torch model developed by Morsli and Proulx [17] with an acceptable degree of agreement. Compared to plasma models, this simplified model proved that the use of HTJ is sufficient for the actual De-Laval nozzle design characterization. In fact, the numerical results of this model highlighted that appropriate profiles of temperature and velocity applied on the nozzle inlet with reduced computational time. Furthermore, the model enabled the investigation of the entire aerodynamic behaviour of HTJ from the nozzle inlet up to the processed surface.

Based on this CFD model, some initial design rules and nozzle parameter sensitivity analysis has been obtained. It highlights the increased performance of an improved nozzle design. This nozzle is expected to enhance the processing capability of plasma figuring by reducing the MSF errors. This

enhanced nozzle is predicted to deliver a 12.5% smaller footprint and 15.5% higher temperature.

Objective 3: Power dissipation analysis of ICP torch – Investigation of the power loss mechanism of a plasma delivery system based on ICP torch and evaluation of the torch efficiency of the bespoke ICP torch.

Results of measurement are analysed and the power dissipated from the coolants in E mode are calculated. This investigation provides a confidence level of 95%, after an uncertainty analysis. In H mode, the measurement of coolant temperature was carried out at the RF power of 850 W to 300 W. According to the near linear correlation between TD and RF power, the power dissipation at 1200 W RF power can be predicated as 400 W.

The percentage of power dissipated by heating the argon gas –calculated using information obtained through the CFD model is 394 W. This result is less robust because the ionisation energy was not counted for.

The radiation from plasma –excitation and transportation regions– is absorbed by surrounding parts: coil, aluminium tube, outer quartz tube, copper nozzle, and surrounding air. Some of the total radiative energy (273 ~ 403 W) is clearly dissipated by coil and nozzle. This amount of energy is already counted by the power dissipated through coolants (5.3.4). Then it is suggested that the $E_{\text{radiation}}$ which is transferred to surrounding air and the aluminium tube is still to be defined. Table 5-4 illustrates the power dissipated of each torch part.

Objective 4: Experimental tests of enhanced nozzles – Design and manufacturing a series of De-Laval nozzles based on the CFD analysis. Test these nozzles based on the power dissipation analysis.

In this section, a unique design of nozzle is introduced. By comparing the intensity of the power dissipation values, one nozzle was clearly identified as being more capable to provide highly efficient plasma jet. Result, which is shown in Figure 5-46, proves that the power dissipated from the enhanced nozzle is less than that of original nozzle. Among the ten nozzles, nozzle No.3 (with the smallest diameter of the divergent end) was selected as with the

smallest amount of power loss when there is a substrate upon the torch nozzle. Nozzle No.7 has the smallest amount of power loss when there is no substrate, due to its shortest depth.

8 Recommendations for future work

This PhD project focused on characterization and optimisation of the bespoke plasma torch and its plasma jet. Two research investigations were carried out using both numerical and experimental approaches. The numerical simulation enabled to understand the aerodynamic and thermodynamic properties of the De-Laval nozzle. The experimental work enabled to understand the power dissipation mechanism in the bespoke ICP torches. However, future research is required to improve the scientific investigation, and to improve the optical fabrication using a plasma figuring process.

The new designed nozzle series have been tested through the power dissipation experiment. The priority of the future work is to test the enhanced nozzle series through material removal footprint experiment. The final optimum nozzle is expected to have a footprint in the range 1 to 5 mm FWHM. Then, the nozzle will be equipped to the bespoke ICP torch for the whole surface figuring process.

Numerical simulation is recommended to improve with higher accuracy of prediction. In the future, the CFD model will take the EM field into account, and 3D geometry will be much beneficial to explain the aerodynamic behaviour of plasma. The further developed model is expected to predict the footprint of plasma torch nozzle for figuring process. Finally, more understanding of the heat effects will be carried out using the CFD model together with the temperature measurement experiment.

REFERENCES

1. Morsli M El., Proulx P. A chemical non-equilibrium model of an air supersonic ICP. *Journal of Physics D: Applied Physics*. 2007; 40(2): 380–394. Available at: DOI:10.1088/0022-3727/40/2/015
2. Gilmozzi R., Spyromilio J. The European extremely large telescope (E-ELT) [JOUR]. *The Messenger*. 2007; 127(11): 3.
3. Stepp LM., Strom SE. The Thirty-Meter Telescope project design and development phase [CONF]. *Second Backaskog Workshop on Extremely Large Telescopes*. International Society for Optics and Photonics; 2004. pp. 67–75.
4. ESO. The European Extremely Large Telescope. 2016. Available at: <http://www.eso.org/public/teles-instr/e-elt/> (Accessed: 10 July 2016)
5. ASML. TWINSCAN NXE:3300B. 2016. Available at: https://www.asml.com/products/systems/twinscan-nxe/twinscan-nxe3300b/en/s46772?dfp_product_id=842 (Accessed: 10 July 2016)
6. Lawrence Livermore National Laboratory. National Ignition Facility & Photon Science. 2016. Available at: <https://lasers.llnl.gov/> (Accessed: 10 July 2016)
7. Corning Inc. Ultra-Low Expansion (ULE®) Glass. 2016. Available at: <https://www.corning.com/emea/en/products/advanced-optics/product-materials/semiconductor-laser-optic-components/ultra-low-expansion-glass.html> (Accessed: 12 July 2016)
8. Hartmann P. ZERODUR ®: deterministic approach for strength design. 2012; Available at: DOI:10.1117/1.OE.51.12.124002
9. SCHOTT AG. ZERODUR® Extremely Low Expansion Glass Ceramic. 2016. Available at: http://www.schott.com/advanced_optics/english/syn/advanced_optics/products/optical-materials/zerodur-extremely-low-expansion-glass-

ceramic/zerodur/index.html (Accessed: 12 July 2016)

10. Egerman R., Matthews G., Wynn J., Kirk C., Havey K. The Current and Future State-of-the-art Glass Optics for Space-based Astronomical Observatories.
11. SCHOTT AG. SCHOTT Lithosil®. 2016. Available at: <http://www.schott.com/magazine/english/solutions/lithosil.html> (Accessed: 18 July 2016)
12. De Jong B., Beerkins RGC., Van Nijnatten PA., Bourhis EL. Glass. Ullmann's Encyclopedia of Industrial Chemistry [GEN]. New York: VCH; 1989.
13. Shore P., Cunningham C., Debra D., Evans C., Hough J., Gilmozzi R., et al. Precision engineering for astronomy and gravity science. CIRP Annals - Manufacturing Technology. 2010; 59(2): 694–716. Available at: DOI:10.1016/j.cirp.2010.05.003
14. Kordonski WI., Shorey AB., Tricard M. Magnetorheological Jet (MR JetTM) Finishing Technology. Journal of Fluids Engineering. American Society of Mechanical Engineers; 2006; 128(1): 20. Available at: DOI:10.1115/1.2140802 (Accessed: 14 August 2016)
15. Arnold T., Boehm G., Schindler A. Ultrahigh-rate plasma jet chemical etching of silicon [JOUR]. Journal of Vacuum Science & Technology A. American Institute of Physics; 2001; 19(5): 2586–2589.
16. Föhnle OW., van Brug H., Frankena HJ. Fluid jet polishing of optical surfaces. Applied Optics. Optical Society of America; 1 October 1998; 37(28): 6771. Available at: DOI:10.1364/AO.37.006771 (Accessed: 14 August 2016)
17. Mori Y., Yamauchi K., Endo K. Elastic emission machining. Precision Engineering. Elsevier; July 1987; 9(3): 123–128. Available at: DOI:10.1016/0141-6359(87)90029-8 (Accessed: 14 August 2016)

18. Francis FC. Introduction to plasma physics. 1974; Available at: https://scholar.google.co.uk/citations?view_op=view_citation&continue=/scholar%3Fhl%3Den%26as_sdt%3D0,5%26scilib%3D1%26scioq%3Dintroduction%2Bto%2Bplasma%2Bphysics%2Bchen&citilm=1&citation_for_view=OMSPWvsAAAAJ:u5HHmVD_uO8C&hl=en&oi=p (Accessed: 18 July 2016)
19. van Roosmalen AJ., Baggerman JAG., Brader SJH. Dry etching for VLSI [BOOK]. Springer Science & Business Media; 2013.
20. Cardinaud C., Peignon M-C., Tessier P-Y. Plasma etching: principles, mechanisms, application to micro- and nano-technologies. Applied Surface Science. 2000; 164(1): 72–83. Available at: DOI:10.1016/S0169-4332(00)00328-7
21. Carr JW. Apparatus and method for atmospheric pressure reactive atom plasma processing for surface modification [GEN]. Google Patents; 2003. Available at: <https://www.google.co.uk/patents/WO2002062111A3?cl=en>
22. Castelli M. Advances in Optical Surface Figuring by Reactive Atom Plasma (RAP)(PhD thesis) [JOUR]. Cranfield University, Cranfield, UK. 2013;
23. Hu H., Dai Y., Peng X. Restraint of tool path ripple based on surface error distribution and process parameters in deterministic finishing. Optics Express. Optical Society of America; 25 October 2010; 18(22): 22973. Available at: DOI:10.1364/OE.18.022973 (Accessed: 20 July 2016)
24. Meister J., Arnold T. New process simulation procedure for high-rate plasma jet machining. Plasma Chemistry and Plasma Processing. 2011; 31(1): 91–107. Available at: DOI:10.1007/s11090-010-9267-y
25. Kelley J., Carr J., Fiske P., Chang A. Apparatus and method for non-contact shaping and smoothing of damage-free glass substrates [GEN]. Google Patents; 2004.
26. Fanara C., Shore P., Nicholls JR., Lyford N., Kelley J., Carr J., et al. A

- new reactive atom plasma technology (RAPT) for precision machining: The etching of ULE surfaces. *Advanced Engineering Materials*. 2006; 8(10): 933–939. Available at: DOI:10.1002/adem.200600028
27. Verma Y., Chang AK., Berrett JW., Futterer K., Gardopée GJ., Kelley J., et al. Rapid damage-free shaping of silicon carbide using Reactive Atom Plasma (RAP) processing. *Proc. of SPIE*. 2006. p. 62730B–62730B–8. Available at: DOI:10.1117/12.671969
 28. Subrahmanyam P., Gardopée G., Verma Y., Li N., Yu T., Kyler T., et al. Rapid fabrication of lightweight SiC aspheres using reactive atom plasma (RAP) processing. *Proceedings of SPIE*. 2007; 6666: 66660A–66660A–4. Available at: DOI:10.1117/12.733123
 29. Subrahmanyam PK., Gardopée G. Reactive atom plasma (RAP) processing of mirrors for astronomy. *Proceedings of SPIE*. 2008; 7018(2008): 701809–701809–701812. Available at: DOI:10.1117/12.786991
 30. Subrahmanyam PK., Pang K., Yu TH., Salij R. Simultaneous figuring and damage mitigation of optical surfaces. *Laser-Induced Damage in Optical Materials*. 2008; 7132: 71321R–71321R–6. Available at: DOI:10.1117/12.804429
 31. Jourdain R., Castelli M., Shore P., Sommer P., Proscia D. Reactive atom plasma (RAP) figuring machine for meter class optical surfaces. *Production Engineering*. 2013; 7(6): 665–673. Available at: DOI:10.1007/s11740-013-0467-1
 32. Castelli M., Jourdain R., Morantz P., Shore P. Rapid optical surface figuring using reactive atom plasma. *Precision Engineering*. Elsevier Inc.; 2012; 36(3): 467–476. Available at: DOI:10.1016/j.precisioneng.2012.02.005
 33. Parkins J. Heat Transfer Properties of Laser Assisted. 2012; (August): 2011–2012.

34. Yu N., Jourdain R., Gourma M., Shore P. Analysis of nozzle design used for the creation of advanced energy beam. Proceedings of 29th ASPE Annual Meeting. 2014; (November): 200–205. Available at: DOI:10.1386/nl.10.1.123
35. Yu N., Jourdain R., Gourma M., Shore P. Analysis of De-Laval nozzle designs employed for plasma figuring of surfaces. The International Journal of Advanced Manufacturing Technology. 2016; Available at: DOI:10.1007/s00170-016-8502-y
36. Bennett, A., Jourdain, R., Kirby, P., MacKay, P., Shore, P. Nicholls, J., Morantz P. Microwave generated plasma figuring for ultra precision engineering of optics. 16th International Conference of the European Society for Precision Engineering and Nanotechnology. Nottingham; 2016.
37. Mori Y., Yamamura K., Yamauchi K., Yoshii K., Kataoka T., Endo K., et al. Plasma CVM (chemical vaporization machining): an ultra precision machining technique using high-pressure reactive plasma. Nanotechnology. 1999; 4(4): 225–229. Available at: DOI:10.1088/0957-4484/4/4/008
38. Takino H., Shibata N., Itoh H., Kobayashi T., Tanaka H., Ebi M., et al. Computer numerically controlled plasma chemical vaporization machining with a pipe electrode for optical fabrication. Appl Opt. 1998; 37(22): 5198–5210. Available at: <http://www.ncbi.nlm.nih.gov/pubmed/18285997>
39. Takino H., Shibata N., Itoh H., Kobayashi T., Yamamura K., Sano Y., et al. Fabrication of optics by use of plasma chemical vaporization machining with a pipe electrode. Applied Optics. 2002; 41(19): 3971–3977. Available at: DOI:10.1364/AO.41.003971
40. Takino H., Shibata N., Itoh H., Kobayashi T., Nemoto K., Fujii T., et al. Fabrication of small complex-shaped optics by plasma chemical vaporization machining with a microelectrode. Applied optics. 2006; 45(23): 5897–5902. Available at: DOI:10.1364/AO.45.005897

41. Takino H., Yamamura K., Sano Y., Mori Y. Shape correction of optical surfaces using plasma chemical vaporization machining with a hemispherical tip electrode. *Applied optics*. 2012; 51(3): 401–407. Available at: DOI:10.1364/AO.51.000401
42. Mori Y., Yamauchi K., Yamamura K., Mimura H., Saito A., Kishimoto H., et al. Development of plasma chemical vaporization machining and elastic emission machining systems for coherent X-ray optics. *Proceedings of SPIE - The International Society for Optical Engineering*. 2001; 4501: 30–42. Available at: DOI:10.1117/12.448496
43. Mori Y., Yamamura K., Endo K., Yamauchi K., Yasutake K., Goto H., et al. Creation of perfect surfaces. *Journal of Crystal Growth*. 2005; 275(1–2): 39–50. Available at: DOI:10.1016/j.jcrysgro.2004.10.097
44. Shibahara M., Yamamura K., Sano Y., Sugiyama T., Endo K., Mori Y. Improvement of the thickness distribution of a quartz crystal wafer by numerically controlled plasma chemical vaporization machining. *Review of Scientific Instruments*. 2005; 76(9): 1–8. Available at: DOI:10.1063/1.2041594
45. Frank W. Depth profiling by means of the combination of glancing incidence X-ray fluorescence spectrometry with low energy ion beam etching technique. *Spectrochimica Acta Part B: Atomic Spectroscopy*. 1995; 50(3): 265–270. Available at: DOI:10.1016/0584-8547(94)00130-N
46. Frost F., Schindler a., Bigl F. Reactive ion beam etching of InSb and InAs with ultrasmooth surfaces. *Semiconductor Science and Technology*. 1999; 13(5): 523–527. Available at: DOI:10.1088/0268-1242/13/5/014
47. Boehm G., Frank W., Schindler A. Radical Jet Etching (RJE) - a new tool for high rate figuring of optical surfaces [CONF]. *Optical Fabrication and Testing*. Québec City : Optical Society of America; 2000. p. OMB2. Available at: DOI:10.1364/OFT.2000.OMB2
48. Schindler A., Haensel T., Flamm D., Frank W., Boehm G., Frost F., et al.

- <title>Ion beam and plasma jet etching for optical component fabrication</title>. 2001; 4440: 217–227. Available at: DOI:10.1117/12.448043
49. Schindler A., Boehm G., Haensel T., Frank W., Nickel A., Rauschenbach B., et al. Precision optical asphere fabrication by plasma jet chemical etching (PJCE) and ion beam figuring. Proceedings of the SPIE - The International Society for Optical Engineering. 2001; 4451 BT-: 242–248. Available at: DOI:10.1117/12.453622
 50. Arnold T., Boehm G., Eichentopf IM., Janietz M., Meister J., Schindler A. Plasma Jet Machining. Vakuum in Forschung und Praxis. 2010; 22(4): 10–16. Available at: DOI:10.1002/vipr.201000423
 51. Arnold T., Boehm G., Fechner R., Meister J., Nickel A., Frost F., et al. Ultra-precision surface finishing by ion beam and plasma jet techniques- status and outlook. Nuclear Instruments and Methods in Physics Research, Section A: Accelerators, Spectrometers, Detectors and Associated Equipment. 2010; 616(2–3): 147–156. Available at: DOI:10.1016/j.nima.2009.11.013
 52. Eichentopf IM., Boehm G., Meister J., Arnold T. Reactive plasma jet high-rate etching of SiC. Plasma Processes and Polymers. 2009; 6(SUPPL. 1): 204–208. Available at: DOI:10.1002/ppap.200930503
 53. Arnold T., Böhm G. Application of atmospheric plasma jet machining (PJM) for effective surface figuring of SiC. Precision Engineering. Elsevier Inc.; 2012; 36(4): 546–553. Available at: DOI:10.1016/j.precisioneng.2012.04.001
 54. Paetzelt H., Arnold T., Böhm G., Pietag F., Schindler A. Surface patterning by local plasma jet sacrificial oxidation of silicon. Plasma Processes and Polymers. 2013; 10(5): 416–421. Available at: DOI:10.1002/ppap.201200099
 55. Arnold T., Böhm G., Paetzelt H. Ultra-Precision Surface Machining with

- Reactive Plasma Jets. Contributions to Plasma Physics. 2014; 54(2): 145–154. Available at: DOI:10.1002/ctpp.201310058
56. Paetzelt H., Böhm G., Arnold T. Etching of silicon surfaces using atmospheric plasma jets. Plasma Sources Science and Technology. 2015; 24(2): 25002. Available at: DOI:10.1088/0963-0252/24/2/025002
 57. Arnold T., Grabovski S., Schindler A., Wagner H-E. Spatially resolved emission spectroscopic investigation of microwave-induced reactive low-power plasma jets. Plasma Sources Science and Technology. 2004; 13(2): 309–314. Available at: DOI:10.1088/0963-0252/13/2/017
 58. Cavaleiro A., Czerwicz T., Helmersson U., van der Kolk G., Moller W., Oehr C., et al. Surface figuring of glass substrates by local deposition of silicon oxide with atmospheric pressure plasma jet. Surface and Coatings Technology. 2011; 205: S351–S354. Available at: DOI:10.1016/j.surfcoat.2011.03.127
 59. Arnold T., Schindler A. Mass spectrometry at a Ar/SF₆/O₂ chemically reactive plasma jet. Physica Status Solidi (a). 2008; 205(4): 957–960. Available at: DOI:10.1002/pssa.200778339
 60. Zhang J., Wang B., Dong S. Application of atmospheric pressure plasma polishing method in machining of silicon ultra-smooth surfaces. Frontiers of Electrical and Electronic Engineering in China. 2008; 3(4): 480–487. Available at: DOI:10.1007/s11460-008-0072-9
 61. Zhang J., Wang B., Dong S. Application of atmospheric pressure plasma polishing method in machining of silicon ultra-smooth surfaces [JOUR]. Frontiers of Electrical and Electronic Engineering in China. Springer; 2008; 3(4): 480–487.
 62. Zhang Y., Wang B., Dong S., Yuan Y. Analysis on the material removal stability for the finishing of the optical surface using atmospheric pressure plasma jet. Proc. of SPIE. 2010; 7655: 76552S–76552S–6. Available at: DOI:10.1117/12.867894

63. Yao YX., Wang B., Wang JH., Jin HL., Zhang YF., Dong S. Chemical machining of Zerodur material with atmospheric pressure plasma jet. *CIRP Annals - Manufacturing Technology*. CIRP; 2010; 59(1): 337–340. Available at: DOI:10.1016/j.cirp.2010.03.118
64. Jin H., Xin Q., Li N., Jin J., Wang B., Yao Y. The morphology and chemistry evolution of fused silica surface after Ar/CF₄ atmospheric pressure plasma processing. *Applied Surface Science*. 2013; 286: 405–411. Available at: DOI:10.1016/j.apsusc.2013.09.100
65. Xin Q., Li N., Wang J., Wang B., Li G., Ding F., et al. Surface roughening of ground fused silica processed by atmospheric inductively coupled plasma. *Applied Surface Science*. 2015; 341: 142–148. Available at: DOI:10.1016/j.apsusc.2015.03.001
66. Shi B., Xie X., Dai Y., Liao C. A high efficiency machining method of SiC: ion-enhanced atmospheric pressure plasma machining. 2014; 9281: 928104. Available at: DOI:10.1117/12.2069012
67. Shi B., Dai Y., Xie X., Li S., Zhou L. Arc-Enhanced Plasma Machining Technology for High Efficiency Machining of Silicon Carbide. *Plasma Chemistry and Plasma Processing*. Springer US; 19 May 2016; 36(3): 891–900. Available at: DOI:10.1007/s11090-016-9695-4 (Accessed: 20 July 2016)
68. Aikens D., DeGroote JE., Youngworth RN. Specification and Control of Mid-Spatial Frequency Wavefront Errors in Optical Systems. *Frontiers in Optics 2008/Laser Science XXIV/Plasmonics and Metamaterials/Optical Fabrication and Testing*. 2008; : OTuA1. Available at: DOI:10.1364/OFT.2008.OTuA1
69. Jousten K. Kalibrierungen und Normen. *Wutz Handbuch Vakuumtechnik*. Wiesbaden: Vieweg+Teubner Verlag; 2004. pp. 554–596. Available at: DOI:10.1007/978-3-322-96971-2_14 (Accessed: 15 August 2016)
70. Valinčius V., Grigaitienė V., Tamošiūnas A. Report on the different

plasma modules for pollution removal MO 0 3 [JOUR]. Plasma for environ protect. 2012;

71. Popov OA. High density plasma sources: design, physics and performance [BOOK]. Elsevier; 1996.
72. Cordos EA., Frentiu T., Rusu A-M., Angel SD., Fodor A., Ponta M. Analytical characterisation of a capacitively coupled plasma torch with a central tube electrode. Talanta. 1999; 48(4): 827–837. Available at: DOI:10.1016/S0039-9140(98)00099-X
73. Reed TB. Induction-Coupled plasma torch. Journal of Applied Physics. 1961; 32(5): 821–824. Available at: DOI:10.1063/1.1736112
74. Reed TB. Heat-Transfer Intensity from Induction Plasma Flames and Oxy-Hydrogen Flames [JOUR]. Journal of Applied Physics. AIP Publishing; 1963; 34(8): 2266–2269.
75. Tong JB., Lu X., Liu CC., Pi ZQ., Zhang RJ., Qu XH. Numerical simulation and prediction of radio frequency inductively coupled plasma spheroidization. Applied Thermal Engineering. 2016; 100: 1198–1206. Available at: DOI:10.1016/j.applthermaleng.2016.02.108
76. Helber B., Turchi A., Scoggins JB., Hubin A., Magin TE. Experimental investigation of ablation and pyrolysis processes of carbon-phenolic ablators in atmospheric entry plasmas. International Journal of Heat and Mass Transfer. 2016; 100: 810–824. Available at: DOI:10.1016/j.ijheatmasstransfer.2016.04.072
77. Liu TY., Li PL., Liu CW., Gau C. Boiling flow characteristics in microchannels with very hydrophobic surface to super-hydrophilic surface. International Journal of Heat and Mass Transfer. 2011; 54(1): 126–134. Available at: DOI:10.1016/j.ijheatmasstransfer.2010.09.060
78. Montaser A., Golightly DW. Inductively coupled plasmas in analytical atomic spectrometry [JOUR]. VCH Publishers, New York, NY; 1987;

79. Hollahan JR., Bell AT. Techniques and applications of plasma chemistry [JOUR]. J Wiley & Sons; 1974;
80. Cunge G., Crowley B., Vender D., Turner MM., J LMA and LA., H KJ., et al. Characterization of the E to H transition in a pulsed inductively coupled plasma discharge with internal coil geometry: bi-stability and hysteresis. Plasma Sources Science and Technology. IOP Publishing; 1 November 1999; 8(4): 576–586. Available at: DOI:10.1088/0963-0252/8/4/309 (Accessed: 19 August 2016)
81. Boulos MI. Flow and Temperature Fields in the Fire-Ball of an Inductively Coupled Plasma. IEEE Transactions on Plasma Science. IEEE; 1976; 4(1): 28–39. Available at: DOI:10.1109/TPS.1976.4316928 (Accessed: 19 August 2016)
82. Razzak MA., Kondo K., Uesugi Y., Takamura S. Transition from electrostatic to electromagnetic mode in atmospheric pressure RF Ar inductively coupled plasma. The 30th International Conference on Plasma Science, 2003. ICOPS 2003. IEEE Conference Record - Abstracts. IEEE; p. 446. Available at: DOI:10.1109/PLASMA.2003.1230027 (Accessed: 4 October 2016)
83. Razzak MA., Takamura S., Uesugi Y. Dynamics of E-H mode transition in high-pressure RF inductively coupled plasmas. IEEE; 2005;
84. Tekna Plasma Systems Inc. Nanopowder Technology. 2016. Available at: <http://tekna.com/equipment-spheroidization-nanosynthesis-deposition/nanopowder-equipment/> (Accessed: 10 July 2016)
85. Boulos MI., Jurewicz J. High performance induction plasma torch with a water-cooled ceramic confinement tube [GEN]. Google Patents; 1993.
86. El Morsli M., Proulx P. Two-temperature chemically non-equilibrium modelling of an air supersonic ICP [JOUR]. Journal of Physics D: Applied Physics. IOP Publishing; 2007; 40(16): 4810.
87. Boselli M., Colombo V., Ghedini E., Gherardi M., Sanibondi P., Jaeggi C.,

- et al. Influence of processing parameters on the properties of silicon nanoparticles synthesized by radio-frequency induction thermal plasma. 2012 Abstracts IEEE International Conference on Plasma Science. IEEE; 2012. p. 7D–2–7D–2. Available at: DOI:10.1109/PLASMA.2012.6384086 (Accessed: 5 October 2016)
88. Boulos MI., Jurewicz J. High performance induction plasma torch with a water-cooled ceramic confinement tube [GEN]. Google Patents; 1992. Available at: <http://www.google.com/patents/CA2085133A1?cl=3Den>
 89. Rahmane M., Soucy G., Boulos MI. Mass transfer in induction plasma reactors. *International Journal of Heat and Mass Transfer*. Pergamon; September 1994; 37(14): 2035–2046. Available at: DOI:10.1016/0017-9310(94)90305-0 (Accessed: 21 July 2016)
 90. Rahmane M., Soucy G., Boulos MI. Analysis of the enthalpy probe technique for thermal plasma diagnostics. *Review of Scientific Instruments*. AIP Publishing; 1995; 66(6): 3424. Available at: DOI:10.1063/1.1145517 (Accessed: 21 July 2016)
 91. Fincke JR., Crawford DM., Snyder SC., Swank WD., Haggard DC., Williamson RL. Entrainment in high-velocity, high-temperature plasma jets. Part I: Experimental results. *International Journal of Heat and Mass Transfer*. 2003; 46(22): 4201–4213. Available at: DOI:10.1016/S0017-9310(03)00272-2
 92. Hopwood J., Guarnieri CR., Whitehair SJ., Cuomo JJ. Langmuir probe measurements of a radio frequency induction plasma. *Journal of Vacuum Science & Technology A: Vacuum, Surfaces, and Films*. AVS: Science & Technology of Materials, Interfaces, and Processing; January 1993; 11(1): 152. Available at: DOI:10.1116/1.578282 (Accessed: 21 July 2016)
 93. Singh SV. Investigation of ICP RF discharges by means of a Langmuir probe. *JOUR. Ruhr-University Bochum*; 2004.
 94. Peterson D., Coumou D., Larson L., Shannon S. Microsecond resolved

- electron density measurements with a hairpin resonator probe in a pulsed ICP discharge. 25 January 2016; Available at: <http://arxiv.org/abs/1601.06811> (Accessed: 21 July 2016)
95. O'Brien WJ. Characterisation and Material Removal Properties of the RAPTM Process. 2011;
 96. Kant MA., Rudolf von Rohr P. Determination of surface heat flux distributions by using surface temperature measurements and applying inverse techniques. *International Journal of Heat and Mass Transfer*. 2016; 99: 1–9. Available at: DOI:10.1016/j.ijheatmasstransfer.2016.03.082
 97. Li HB., Zhen HS., Leung CW., Cheung CS. Effects of plate temperature on heat transfer and emissions of impinging flames. *International Journal of Heat and Mass Transfer*. 2010; 53(19): 4176–4184. Available at: DOI:10.1016/j.ijheatmasstransfer.2010.05.040
 98. Dong L., Cheung C., Leung C. Heat transfer from an impinging premixed butane/air slot flame jet. *International Journal of Heat and Mass Transfer*. 2002; 45(5): 979–992. Available at: DOI:10.1016/S0017-9310(01)00215-0
 99. Jourdain R., Castelli M., Yu N., Gourma M., Shore P. Estimation of the power absorbed by the surface of optical components processed by an inductively coupled plasma torch. *Applied Thermal Engineering*. 2016; Available at: DOI:10.1016/j.applthermaleng.2016.08.024
 100. Leader JJ., Leader JJ. Numerical analysis and scientific computation [BOOK]. 2004.
 101. Suzen Y., Huang G., Jacob J., Ashpis D. Numerical Simulations of Plasma Based Flow Control Applications. 35th AIAA Fluid Dynamics Conference and Exhibit. 2005; : 1–11. Available at: DOI:10.2514/6.2005-4633
 102. Eymard R., Gallouët T., Herbin R. Finite volume methods [JOUR]. *Handbook of numerical analysis*. Elsevier; 2000; 7: 713–1018.

103. Reddy JN. An introduction to the finite element method [BOOK]. McGraw-Hill New York; 1993.
104. Iserles A. A first course in the numerical analysis of differential equations [BOOK]. Cambridge university press; 2009.
105. ANSYS Inc. ANSYS Fluent. 2016. Available at: <http://www.ansys.com/Products/Fluids/ANSYS-Fluent> (Accessed: 10 July 2016)
106. COMSOL Inc. A new version of COMSOL Multiphysics® and COMSOL Server™ is available. 2016. Available at: <https://www.comsol.com/> (Accessed: 10 July 2016)
107. ESI Group. CFD-ACE+. 2016. Available at: <https://www.esi-group.com/software-solutions/virtual-environment/cfd-multiphysics/ace-suite/cfd-ace> (Accessed: 10 July 2016)
108. CHAM Limited. CHAM Your Gateway to CFD Success. 2016. Available at: <http://www.cham.co.uk/> (Accessed: 10 July 2016)
109. ANSYS Inc. ANSYS CFX. 2016. Available at: www.ansys.com/Products/Fluids/ANSYS-CFX (Accessed: 10 July 2016)
110. CD-adapco. STAR-CCM+ v11.04. 2016. Available at: <http://www.cd-adapco.com/#> (Accessed: 10 July 2016)
111. Potter DE. Numerical Studies of the Plasma Focus. Physics of Fluids. AIP Publishing; 1971; 14(9): 1911. Available at: DOI:10.1063/1.1693700 (Accessed: 4 October 2016)
112. Maxon S., Eddleman J. Two-dimensional magnetohydrodynamic calculations of the plasma focus. Physics of Fluids. AIP Publishing; 1978; 21(10): 1856. Available at: DOI:10.1063/1.862103 (Accessed: 4 October 2016)
113. Mostaghimi J., Proulx P., Boulos MI. An analysis of the computer modeling of the flow and temperature fields in an inductively coupled

- plasma. Numerical Heat Transfer. 1985; 8: 187–201. Available at: DOI:10.1080/01495728508961849
114. Mostaghimi J., Boulos MI. Two-dimensional electromagnetic field effects in induction plasma modelling. Plasma Chemistry and Plasma Processing. 1989; 9(1): 25–44. Available at: DOI:10.1007/BF01015825
 115. Sember V., Gravelle D V., Boulos MI. Spectroscopic study of a supersonic plasma jet generated by an ICP torch with a convergent-divergent nozzle. Journal of Physics D: Applied Physics. 2002; 35(12): 1350–1361. Available at: DOI:10.1088/0022-3727/35/12/311
 116. Murphy AB., Boulos MI., Colombo V., Fauchais P., Ghedini E., Gleizes A., et al. Advanced Thermal Plasma Modelling. High Temperature Material Processes. 2008; 12(3–4): 255–336.
 117. Selezneva SE., Boulos MI. Supersonic induction plasma jet modeling. Nuclear Instruments and Methods in Physics Research, Section B: Beam Interactions with Materials and Atoms. 2001; 180(1–4): 306–311. Available at: DOI:10.1016/S0168-583X(01)00436-0
 118. Li D., Xia G., Merkle CL. Analysis of real fluid flows in converging diverging nozzles. AIAA Paper 2003-4132. 2003; (June): 1–15.
 119. Miller RC., Ayen RJ. Temperature profiles and energy balances for an inductively coupled plasma torch. Journal of applied physics. 1969; 40(13): 5260–5273. Available at: DOI:10.1063/1.323266
 120. Bolot R., Imbert M., Coddet C. On the use of a low-Reynolds extensions to the Chen-Kim (??-??) model to predict thermal exchanges in the case of an impinging plasma jet. International Journal of Heat and Mass Transfer. 2001; 44(6): 1095–1106. Available at: DOI:10.1016/S0017-9310(00)00185-X
 121. Shigeta M., Sato T., Nishiyama H. Numerical simulation of a potassium-seeded turbulent RF inductively coupled plasma with particles. Thin Solid Films. July 2003; 435(1–2): 5–12. Available at: DOI:10.1016/S0040-

6090(03)00366-3 (Accessed: 15 August 2016)

122. Nishiyama H., Muro Y., Kamiyama S., H N., Mostaghimi J PP and BMI., Bourdin E FP and BMI., et al. The control of gas temperature and velocity fields of a RF induction thermal plasma by injecting secondary gas. *Journal of Physics D: Applied Physics*. IOP Publishing; 14 October 1996; 29(10): 2634–2643. Available at: DOI:10.1088/0022-3727/29/10/014 (Accessed: 15 August 2016)
123. Bernardi D., Colombo V., Ghedini E., Mentrelli A. Three-dimensional modelling of inductively coupled plasma torches. *The European Physical Journal D - Atomic, Molecular and Optical Physics*. EDP Sciences, Springer-Verlag, Società Italiana di Fisica; 1 January 2003; 22(1): 119–125. Available at: DOI:10.1140/epjd/e2002-00233-9 (Accessed: 15 August 2016)
124. Colombo V., Ghedini E., Sanibondi P. A three-dimensional investigation of the effects of excitation frequency and sheath gas mixing in an atmospheric-pressure inductively coupled plasma system. *J. Phys. D: Appl. Phys.* *J. Phys. D: Appl. Phys.* 2010; 43(43): 105202–105202. Available at: DOI:10.1088/0022-3727/43/10/105202 (Accessed: 15 August 2016)
125. Boulos MI. The inductively coupled R.F. (radio frequency) plasma. *Pure and Applied Chemistry*. International Union of Pure and Applied Chemistry; 1 January 1985; 57(9): 1321–1352. Available at: DOI:10.1351/pac198557091321 (Accessed: 15 August 2016)
126. Morsli M El., Proulx P., Gravelle D., I BM., I BM., F G., et al. Chemical non-equilibrium modelling of an argon–oxygen supersonic ICP. *Plasma Sources Science and Technology*. IOP Publishing; 1 February 2011; 20(1): 15016. Available at: DOI:10.1088/0963-0252/20/1/015016 (Accessed: 15 August 2016)
127. Xi C. Heat transfer and flow in a radio frequency plasma torch—a new modelling approach. *International Journal of Heat and Mass Transfer*.

- Pergamon; May 1990; 33(5): 815–826. Available at: DOI:10.1016/0017-9310(90)90065-3 (Accessed: 15 August 2016)
128. DeWitt DP., Nutter GD. Theory and practice of radiation thermometry [BOOK]. Wiley Online Library; 1988.
 129. Jourdain R., Castelli M., Morantz P., Shore P. Plasma surface figuring of large optical components [CONF]. SPIE Photonics Europe. International Society for Optics and Photonics; 2012. p. 843011.
 130. Inc. C. Turbotune Technology: Frequency Tuning for High Performance RF Plasma Systems. 2016. Available at: <http://www.comdel.com/optional-frequency-agile-tuning> (Accessed: 4 October 2016)
 131. Knight DW. Practical continuous functions for the internal impedance of solid cylindrical conductors [JOUR]. G3YNH. info. 2012;
 132. Boss CB., Fredeen KJ. Concepts, instrumentation and techniques in inductively coupled plasma optical emission spectrometry [BOOK]. Perkin Elmer Norwalk; 1999.
 133. Belostotskiy SG., Khandelwal R., Wang Q., Donnelly VM., Economou DJ., Sadeghi N. Measurement of electron temperature and density in an argon microdischarge by laser Thomson scattering. Applied Physics Letters. 2008; 92(22). Available at: DOI:10.1063/1.2939437
 134. Chen WLT., Heberlein J., Pfender E. Critical Analysis of Viscosity Data of Thermal Argon Plasmas at Atmospheric Pressure. Plasma Chemistry and Plasma Processing. 1996; 16(4): 635–650. Available at: DOI:10.1007/BF01447012
 135. Rott N. Note On The History Of The Reynolds Number. Annual Review of Fluid Mechanics. 1990; 22(1): 1–11. Available at: DOI:10.1146/annurev.fluid.22.1.1
 136. Launder BE., Spalding DB. The numerical computation of turbulent flows. Computer Methods in Applied Mechanics and Engineering. 1974; 3(2):

269–289. Available at: DOI:10.1016/0045-7825(74)90029-2

137. Wang HX., Chen X., Pan W. Modeling study on the entrainment of ambient air into subsonic laminar and turbulent argon plasma jets. *Plasma Chemistry and Plasma Processing*. 2007; 27(2): 141–162. Available at: DOI:10.1007/s11090-006-9047-x
138. Rowe DM. *Thermoelectrics handbook: macro to nano*. Thermoelectrics Handbook Macro to Nano. 2005; 80(10): 1014. Available at: DOI:10.1038/ki.2011.318
139. Glass expansion. Care of torch. Available at: http://www.geicp.com/cgi-bin/site/wrapper.pl?c1=Care_gencaretorch (Accessed: 6 October 2016)
140. Dietrich CF. *Uncertainty, calibration and probability: the statistics of scientific and industrial measurement* [BOOK]. CRC Press; 1991.
141. Bell S. *A beginner's guide to uncertainty of measurement* [BOOK]. National Physical Laboratory Teddington, Middlesex; 2001.
142. Reid RC., Prausnitz JM., Poling BE. *The properties of gases and liquids* [JOUR]. McGraw Hill Book Co., New York, NY; 1987;
143. Gutsol AF., Larjo J., Hernberg R. Reverse-flow swirl radio-frequency induction plasmatron [JOUR]. *High Temperature*. Springer; 2001; 39(2): 169–179.
144. Wilbers ATM., Beulens JJ., Schram DC. Radiative energy loss in a two-temperature argon plasma. *Journal of Quantitative Spectroscopy and Radiative Transfer*. 1991; 46(5): 385–392. Available at: DOI:10.1016/0022-4073(91)90040-W
145. Benoy DA., Van der Mullen JAM., Schram DC. Radiative energy loss in a non-equilibrium argon plasma [JOUR]. *Journal of Physics D: Applied Physics*. IOP Publishing; 1993; 26(9): 1408.
146. Merkhouf A., Boulos MI. Experimental validation for an integrated model of the induction plasma generation system [CONF]. *Proc. 14th Int. Symp.*

on Plasma Chemistry. 1999. p. 421.

147. Kang CW., Ng HW., Yu SCM. Comparative study of plasma spray flow fields and particle behavior near to flat inclined substrates [JOUR]. Plasma chemistry and plasma processing. Springer; 2006; 26(2): 149–175.
148. Li H-P., Pfender E. Three dimensional modeling of the plasma spray process [JOUR]. Journal of Thermal Spray Technology. Springer; 2007; 16(2): 245–260.
149. Selvan B., Ramachandran K., Pillai BC., Subhakar D. Numerical modelling of Ar-N₂ plasma jet impinging on a flat substrate. Journal of Thermal Spray Technology. 2011; 20(3): 534–548. Available at: DOI:10.1007/s11666-010-9587-8